

**MAGNETIC IRON OXIDE NANOPARTICLES  
AS POTENTIAL CONTRAST AGENTS FOR  
MAGNETIC RESONANCE IMAGING**

**Dissertation**

zur

Erlangung des Doktorgrades  
der Naturwissenschaften  
(Dr. rer. nat)

dem Fachbereich Pharmazie  
der Philipps-Universität Marburg

vorgelegt von  
Christoph Schweiger  
aus Schwabmünchen / Bayern

Marburg / Lahn 2010

Vom Fachbereich Pharmazie der Philipps-Universität Marburg als Dissertation  
am 17.12.2010 angenommen.

Erstgutachter: Prof. Dr. Thomas Kissel

Zweitgutachter: Prof. Dr. Wolfgang Parak

Tag der mündlichen Prüfung am 20.12.2010

Erscheinungsort und -jahr: Marburg, 2010

Hochschulkennziffer: 1180

Die vorliegende Arbeit entstand auf Anregung und unter Leitung von

*Herrn Prof. Dr. Thomas Kissel*

am Institut für Pharmazeutische Technologie und Biopharmazie  
der Philipps-Universität Marburg.

Gewidmet meinen Eltern  
in Liebe und Dankbarkeit.

# Table of Contents

CHAPTER 1	INTRODUCTION .....	1
	MAGNETIC NANOPARTICLES IN NANOTECHNOLOGY .....	2
	BIODISTRIBUTION AND TARGETING .....	3
	APPLICATIONS IN BIOMEDICINE .....	6
	PHYSICAL PRINCIPLES OF MAGNETISM .....	9
	PRINCIPLES OF MAGNETIC RESONANCE IMAGING (MRI) .....	21
	MRI CONTRAST AGENTS.....	26
	MANUFACTURING TECHNIQUES .....	28
	OBJECTIVE OF THE STUDY .....	31
	REFERENCES .....	34
CHAPTER 2	NOVEL MAGNETIC IRON OXIDE NANOPARTICLES FOR POTENTIAL BIOMEDICAL APPLICATION: SYNTHESIS, STABILITY, CYTOTOXICITY AND MR IMAGING.....	43
	ABSTRACT.....	44
	INTRODUCTION .....	45
	MATERIALS AND METHODS .....	46
	RESULTS AND DISCUSSION.....	51
	CONCLUSIONS.....	63
	ACKNOWLEDGEMENTS.....	64
	REFERENCES .....	65

CHAPTER 3	CELL UPTAKE BEHAVIOR OF OPPOSITELY CHARGED MAGNETIC IRON OXIDE NANOPARTICLES – IMPLICATIONS FOR SUBSEQUENT CELLULAR MR IMAGING .....	72
	ABSTRACT.....	73
	INTRODUCTION .....	73
	MATERIALS AND METHODS .....	75
	RESULTS.....	80
	DISCUSSION .....	87
	CONCLUSIONS.....	90
	ACKNOWLEDGEMENTS.....	90
	REFERENCES .....	91
CHAPTER 4	SUMMARY AND OUTLOOK .....	97
	SUMMARY .....	98
	OUTLOOK.....	100
	ZUSAMMENFASSUNG.....	101
	AUSBLICK .....	103
APPENDICES .....		104
	ABBREVIATIONS .....	105
	LIST OF PUBLICATIONS .....	107
	CURRICULUM VITAE .....	108

**Chapter 1      Introduction**



---

**MAGNETIC NANOPARTICLES IN NANOTECHNOLOGY**

Nanotechnology has revolutionized many branches of science and is generally regarded as one of the most promising future technologies, due to its broad scope of potential applications. One general advantage of nanotechnology is its versatility to modify physical, chemical and biological properties of materials when reaching nanoscale dimensions. Commonly, sizes of approximately 1 – 100 nm in diameter are regarded as relevant. One of the subfields in which nanoparticulate objects have found application is nanomedicine. As various biological processes occur at the nanometer scale, they can be easily accessed or manipulated by nanoparticles [1]. In combination with their unique physicochemical properties, nanoparticles offer interesting features for drug delivery and diagnostic purposes. Advances in materials science further contribute to the development of improved carriers for a more specialized treatment and diagnosis of diseases [2]. The motivation for these structural refinements is to approximate the idealized concept of ‘magic bullets’ proposed by Paul Ehrlich, who envisioned a pharmaceutical agent selectively targeting abnormalities inside the body with no side effects. Apart from the quest for specificity, nano science is attempting to provide nanoparticles with additional functionalities, such as traceability or susceptibility to external triggers.

Magnetic nanoparticles (MNP) represent a class of carriers with inherent functionality. Due to the multitude of physical processes inducible in these carriers, MNP have gained considerable interest among the broad spectrum of nanoscale materials for biomedical use [3]. The effects mediated by intrinsic magnetic properties range from heat generation to magnetic attraction and tissue proton relaxation. This versatility of action renders MNP highly suitable for numerous applications, including hyperthermia, magnetic resonance imaging (MRI) and (image-guided) drug delivery. As regards biomedical applications, MNP are usually administered orally or intravenously in the form of stable ferrofluidic nanosuspensions [4].



---

These nanoparticles are composed of magnetic iron or ferrite cores surrounded by organic or inorganic coatings and, optionally, drug or targeting molecules. In general, the complexity of the modular design of MNP is dependent on the desired application. Several routes have been described for the synthesis of magnetic cores, each with a different impact on size, crystallinity and morphology of the generated nanoparticles [5]. Subsequent or concomitant addition of stabilizers is a crucial step, as these molecules provide size control, stabilization in aqueous environments and the possibility for further functionalization [6]. In the majority of cases, the resultant assembly is comparable to a core-shell structure. This dual design involves MNP being recognized as ‘usual’ nanoparticulate vehicles from the outside while carrying an internal functionality. These considerations are relevant to the prediction of biodistribution processes upon administration of MNP.

### **BIODISTRIBUTION AND TARGETING**

Nanoparticles have to overcome a number of physiological barriers before reaching the site of action. In the case of intravascular administration, nanoparticles are confronted with ample plasma-protein levels, blood cells and high ionic strength of the bloodstream [7]. Apart from aggregation of nanoparticles, extensive attachment of plasma proteins and subsequent removal by phagocytic cells can occur. The latter effect is a function of both particle size and surface texture, and by appropriate manipulation of these parameters, blood circulation times and access to deep compartments can be significantly enhanced [8]. Where MNP are concerned, the impact of size could be demonstrated for ultrasmall superparamagnetic iron oxide nanoparticles (USPIO), which display enhanced plasma half-life, and are thus capable of extravasating to a larger extent from the blood vessels into interstitial spaces [9].

In addition, the biodistribution of nanoparticles is largely dependent on the morphology and accessibility of certain tissues. Targeting effects can contribute to a preferential accumulation of pharmaceutical agents inside cancerous areas of the body. Passive targeting exploits the characteristic features of tumor biology, which allow nanoparticles to concentrate in the tumor by the enhanced permeability and retention (EPR) effect [10]. This effect describes the facilitated entrance and enhanced residence of nanoscaled particles in tumor tissues, due to the defective vasculature and dysfunctional lymphatic drainage of tumors. The degree of drug accumulation generally varies with tumor size, vascular maturation and endothelialization heterogeneity of tumor blood vessels [11].

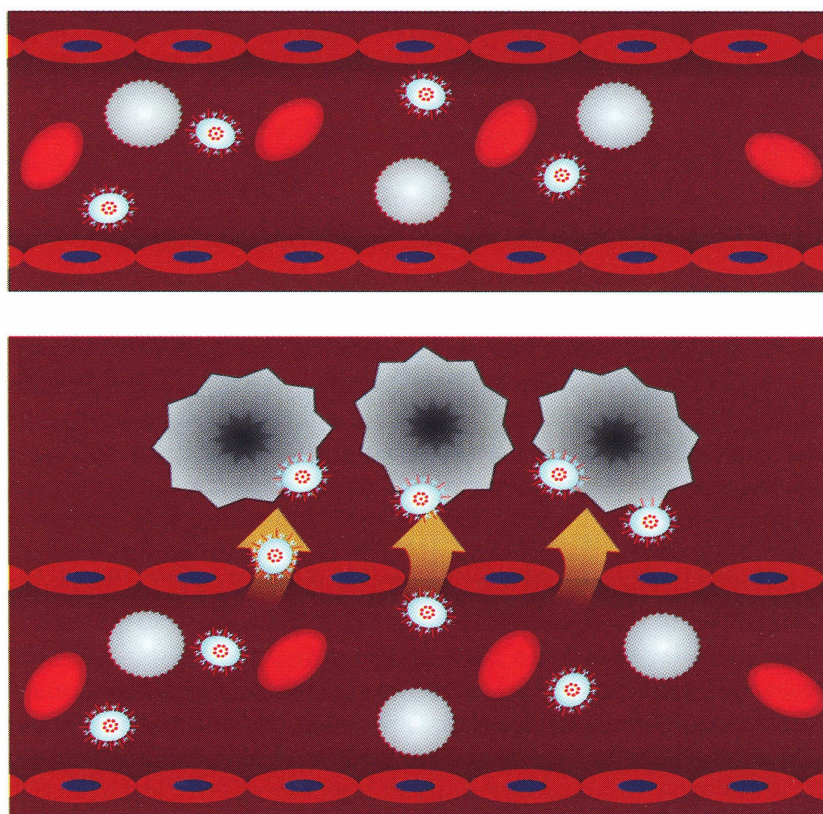


*Figure 1. Passive tumor targeting: Long-time confinement of pharmaceutical nanocarriers inside vessels with intact vasculature (top), and facilitated extravasation of such carriers due to fenestrated tumor vasculature (bottom) [12].*

---

As passive targeting suffers from several limitations, including EPR restriction to specific tumors and random nature of the approach, the need for more selective strategies has emerged. Active targeting involves the attachment of recognition molecules to the surface of nanoparticles, in order to achieve maximum binding to target cell receptors [13]. There are different classes of potential recognition molecules, including antibodies, proteins, small molecules and aptamers [14]. Consequently, tumor binding and internalization are significantly enhanced at the desired site of action.

The principles of active and passive targeting can also be transferred to magnetic nanoparticles. As stated above, MNP for biomedical applications usually carry polymer shells, so that their interaction with cellular components of the body is highly comparable to polymeric drug delivery vehicles. Consequently, the performance of MNP is associated to both external factors, such as size and surface texture, and internal factors like magnetism and crystallinity [15]. Depending on the choice of application for MNP, different aspects of targeting have priority. While passive distribution of the MNP formulation throughout the body is in most cases sufficient for imaging purposes, active targeting strategies are desirable for drug delivery and hyperthermia purposes. In this context, biodistribution experiments are often helpful for the prediction of accumulation and effectiveness of nanocarriers. A convenient method to measure pharmacokinetic distribution profiles of magnetic nanoparticles is radiolabeling [16].

---

## APPLICATIONS IN BIOMEDICINE

### **Magnetic nanoparticles in drug delivery and hyperthermia**

Drug delivery designates the method or process of administering a pharmaceutical compound to achieve a therapeutic effect in humans or animals [17]. The classical efforts of magnetic drug delivery included the targeting of drug-loaded MNP by means of a strong external field. Due to the limited depth effect of permanent magnets, this method is becoming increasingly irrelevant [18]. In this context, the near-surface treatment of physical defects constitutes an exception. For example, studies for the intraarticular retention of magnetic particles in the presence of an external magnet have shown promising results. Implantation of permanent magnets close to the site of action is another possibility of circumventing the depth limitation [19]. Moreover, very strong magnetic field gradients can be used to manipulate MNP in deeper body regions [20]. The more popular approach of image-guided drug delivery will be discussed in a later section.

Magnetic hyperthermia is a treatment modality for cancer, which exploits the high efficiency of superparamagnetic crystal suspensions to absorb energy in an oscillating magnetic field and transform it into heat [21]. Depending on the induced temperature and the duration of heating, the therapy either results in direct death of tumor cells, or makes the cells more susceptible to concomitant radiotherapy or chemotherapy [22]. Healthy tissues can tolerate elevated temperatures for longer periods because of their intact thermoregulation. Further protection of healthy cells can be achieved by the direct local application of MNP into the tumor tissue. The heat dissipation of MNP results from the parallel contributions of thermal and viscous rotation upon oscillation of a magnetic field [23]. The energy release is dependent on both particle size and polydispersity of the excited material, and is given as specific absorption rate (SAR) [24]. Studies with targeted magnetic nanoparticles are still restricted to the *in vitro* stage, due to the insufficient level of accumulation at the site of action [25]. In

contrast, localized administration of magnetic ferrofluids by means of minimally invasive surgery is currently being studied for a number of applications, either as single or synergetic therapy [26]. In 2010, the medicinal products NanoTherm® and NanoActivator® (MagForce Nanotechnologies) have found EU approval for the treatment of glioblastoma multiforme [27].

### **Applications in magnetic resonance imaging**

The application of magnetic nanoparticles as MRI contrast agents aims at the improved depiction of somatic structures. MNP have the potential to accentuate signal intensity differences between adjacent tissues in MRI experiments. The concurrent contrast enhancement is attributable to their unique relaxometric properties. In scientific literature, MNP for imaging purposes are often referred to as superparamagnetic iron oxide nanoparticles (SPION and USPIO) [28]. These nanoparticles accumulate in the cells of the mononuclear phagocytic system upon administration. Depending on their location after uptake, these agents can serve as MRI markers for liver and spleen imaging, lymph node and blood pool imaging [29].

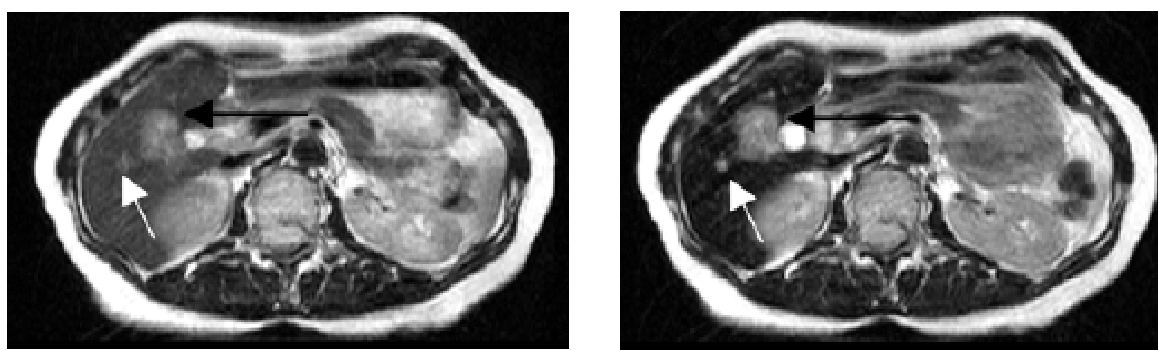


*Figure 2. MRI detection of breast cancer metastasis in a liver segment before (left) and after (right) application of SPION contrast agents. Improved delineation of metastasis (black arrows) and liver lesions (white arrows) is observable after SPION administration [30].*

Classical SPIONs are not suitable for tumor visualization because of insufficient accumulation at the tumor site. The need for contrast agents with pronounced tumor selectivity has led to the development of modern SPIONs combining previous features with active targeting principles (*Table 1*).

Name	Target	Imaging application	Reports
Folic acid	Folate receptor	Breast cancer	[34]
RGD mimetic	$\alpha_v\beta_3$ integrin	Integrin-positive cell imaging	[35]
PBP	P-selectin	Post-stroke neuroinflammation	[36]
RGD peptide	$\alpha_v\beta_3$ integrin	Breast cancer	[37]
EGFRvIII antibody	EGFRvIII	Glioblastoma multiforme	[38]
anti-HER2 affibody	HER2/neu	Breast cancer	[39]

*Table 1. Targeting strategies for magnetic nanoparticles: name of targeting moieties, cellular targets and therapeutic application.*

Depending on their composition, targeted nanocarriers are able to locate a large number of structures. The possibility of tailoring MNP in such a way that they can track down a defined molecular target concurs with the idea of molecular imaging [31]. In addition to structural refinements, the performance of MNP can be upgraded by introducing further functionalities, for example, therapeutic payloads and secondary imaging agents. Drug-loaded MNP are used to monitor drug accumulation at the desired site of action or to trigger drug release, hence the expressions image-guided drug delivery and theragnostics [32]. The bound agents are in most cases chemotherapeutics or radiotherapeutics for cancer therapy. In recent years, stem cell

---

therapy has attracted much attention, due to its healing potential for incurable diseases. The fate of administered stem cells can be tracked after *ex vivo* labeling with MNP. Meanwhile, the concept of cell tracking has been expanded to xenografts, among others [33].

### **Future developments**

Over the past decade, the concept of multimodality *in vivo* imaging has emerged. The term describes the combination of two or more imaging modalities complementing each other, usually within the setting of a single examination. Among the applied modalities are MRI, X-ray computed tomography (CT) and single-photon emission computed tomography (SPECT). Contrast agents suitable for multimodality *in vivo* imaging must be responsive to the chosen modalities and have to meet strict requirements, including sustained detectability of signal, lack of interference and uniformity of signal ratio [40]. The confinement of two functionalities in one nanocarrier enables dual imaging following a single administration. Standard nanosystems for MRI and optical imaging containing iron oxide and Cy5.5 are, for example, used for precise surgical procedure planning [41]. In short, the challenge to generate tailored contrast agents for multimodality *in vivo* imaging is substantial.

### **PHYSICAL PRINCIPLES OF MAGNETISM**

The first studies on the phenomenon of magnetism date back almost three thousand years, but it was not until the nineteenth century that scientists made enormous progress in the understanding of the physical principles which underlie magnetism. Among the most important findings were on the one hand the direct linkage of magnetism and electricity, on the other hand the atomistic rather relativistic explanation for magnetic effects. Magnetism is a cooperative phenomenon which involves the interplay of huge numbers of particles. Thus,

the magnetic behavior of macroscopic systems is not restricted to the individual state of intrinsic isolated magnetic moments, because also their order and mutual interactions contribute to the overall effect [42].

In this section, the most relevant mechanistic principles and forms of magnetism are introduced, as they present the base for the phenomenon of superparamagnetism, which is of major interest in this work.

### **Magnetic moments and magnetization**

The magnetic moment is the fundamental quantity in magnetism. If an electric current  $I$  circulates around an infinitesimal oriented loop of area  $dA$ , then a magnetic field is generated normal to the loop plane with a resultant magnetic moment  $d\mu$  given by

$$d\mu = I dA . \quad (\text{Eq. 1})$$

Due to the fact that a loop of finite size presents nothing else than a giant assembly of equal infinitesimal current loops distributed throughout its plane, the overall magnetic moment  $\mu$  of such loops can be calculated by the integration of the generated minuscule moments  $d\mu$ :

$$\mu = \int d\mu = I \int dA . \quad (\text{Eq. 2})$$

The appearance of magnetic moments in atoms is associated with both the orbital motion of electrons around the nucleus and their tumbling spin rotation around their own axis. Both types of movement influence the angular momentum  $L$  of the electrons and go along with a transport of current, thereby creating a magnetic moment. According to quantum theory, all angular momenta appearing in atoms are quantized, in such a way that their values are either integral or half-integral multiples of the quantity  $h/2\pi$  ( $= \hbar$ ), where  $h$  is Planck's constant. Hence, the magnetic moment of an atom bearing a charge  $q$  is also quantized and can be written as

$$\mu = \frac{q \hbar L}{2m \hbar} . \quad (\text{Eq. 3})$$



For an electron with  $m = m_e$  and  $q = -e$  which revolves around the nucleus of a hydrogen atom, the equation is simplified to

$$\mu = -\frac{e\hbar}{2m_e} = -\mu_B, \quad (\text{Eq. 4})$$

where  $\mu_B$  is the Bohr magneton, defined by

$$\mu_B = \frac{e\hbar}{2m_e} = 9.27 \times 10^{-24} \text{ Am}^2. \quad (\text{Eq. 5})$$

The Bohr magneton is the smallest entity of the magnetic moment, and by convention a convenient unit for describing the overall size of atomic magnetic moments. Inside a magnetic solid, a large number of atoms with magnetic moments is present. The magnetization  $M$  represents the common descriptor for magnetic systems at the macroscopic scale, and is defined as the magnetic moment per unit volume. The magnetization  $M$  can be imagined as a vector field which is continuous throughout homogeneous materials, except for their edges.

### **Magnetic field and magnetic susceptibility**

The physical quantities of the magnetic field  $H$  and the magnetic induction  $B$  are linked under vacuum conditions via the permeability of free space  $\mu_0$ :

$$B = \mu_0 H. \quad (\text{Eq. 6})$$

Inside magnetic materials, the relation between both quantities is complicated by the contribution of the intrinsic magnetization  $M$ , so that the abovementioned equation has to be expanded to

$$B = \mu_0(H + M) = \mu_0(H + \chi H) = \mu_0(1 + \chi)H = \mu_0 \mu_r H, \quad (\text{Eq. 7})$$

where  $\chi$  is the magnetic susceptibility and  $\mu_r = 1 + \chi$  is the relative permeability of the respective material. The parameter  $\chi$  describes the degree of magnetization of a substance in response to an applied field.

---

Depending on the material type, the susceptibility  $\chi$  takes characteristic values which are indicative of a certain class of magnetic behavior:

Diamagnetism	$\chi$ negative, $ \chi  \ll 1$
Paramagnetism	$\chi$ positive, $ \chi  \ll 1$
Ferromagnetism	$\chi$ positive, $ \chi  \gg 1$ .

Diamagnetic and paramagnetic materials exhibit magnetic susceptibilities close to zero, and consequently only weak responses to external fields. In contrast, ferromagnetic effects are rather large, able to produce magnetizations orders of magnitude greater than the applied field [43]. The reason for this striking discrepancy lies in the state of order: while materials from the first two groups can be regarded as assemblies of isolated, non-interacting magnetic moments, ferromagnets display long-range magnetic order, leading to strong cooperative forces (below a certain critical temperature). Further ground states with highly ordered structures include ferrimagnets, which will be discussed later, antiferromagnets and spin glasses.

### **Diamagnetism**

Diamagnetism is an inherent additive effect of all materials, but it only constitutes the predominant role for substances containing atoms or molecules with filled electronic shells. The application of a magnetic field causes the induction of a magnetic polarization, which opposes the original field and therefore weakens the magnetic induction  $B$  inside the material ( $\chi < 0$ ). This is in accordance to Lenz's Law, which claims that the triggered back electromotive force on charge carriers acts antidiagonal to the magnetic field [44]. It is noteworthy that all materials undergo this orbital response. However, in paramagnetic and ferromagnetic substances, this rather weak effect is overwhelmed by the existence of major permanent magnetic moments caused by unpaired electrons. Perfect diamagnets with

magnetic susceptibilities of  $-1$  have found most considerable technical application as superconductors.

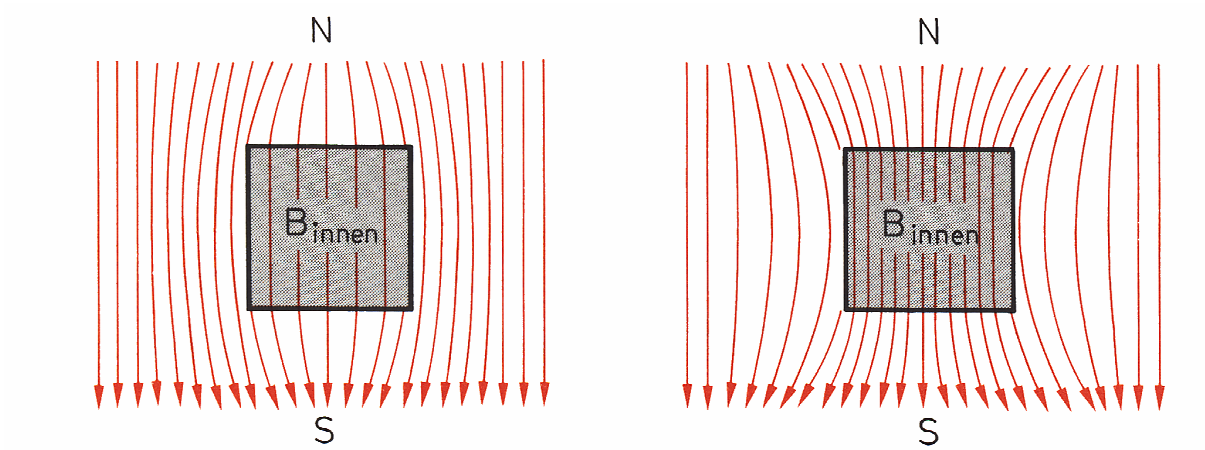


Figure 2. Behavior of diamagnetic (left) and paramagnetic (right) solids in a homogeneous magnetic field. A diamagnetic substance is repelled from the magnetic field, due to induction of a magnetization opposed to the original field [43].

### Paramagnetism

When paramagnetic materials are introduced into an external magnetic field, an enforcing magnetization parallel to the existing field is induced. Atoms of paramagnets contain unpaired electrons, and thus permanent non-zero magnetic moments which tend to either randomize and be statistically distributed at zero field conditions, or line up with an applied field. For the latter case, a net magnetization  $M$  becomes measurable which depends on both the field strength  $B$  and the temperature  $T$ . Thermal agitation counteracts the alignment, whereas high field magnitude favors it. The magnetization of a classical paramagnet is described by the Langevin function,

$$L(x) = \frac{M}{M_s} = \coth x - \frac{1}{x}, \quad x = \frac{\mu B}{k_B T}, \quad (\text{Eq. 8})$$

---

where  $k_B$  is the Boltzmann constant and  $M_S$  is the saturation magnetization, which is the maximum detectable magnetization at complete alignment of all moments.

For small magnetic fields, Curie's Law states the inverse proportionality of magnetic susceptibility and temperature.

### **Ferromagnetism**

The special arrangement of magnetic moments inside ferromagnets explains their unique properties. Ferromagnetic systems are composed of domains which in turn enclose magnetic moments of parallel orientation. The unidirectional alignment of moments is a consequence of the exchange interactions between identical particles, and can be predicted by quantum mechanical calculations [44]. Despite the fact that each domain is thus magnetized until saturation, untreated ferromagnets do not appear to be magnetic at the macroscopic scale, which is due to the transient change in domain orientation and the resultant cancellation of moments.

Upon application of a magnetic field, several processes including domain wall motion, domain rotation and coherent domain rotation all lead to the gradual alignment of magnetic moments with the external field, and give rise to a strong net magnetization. This magnetization  $M$  increases with the field strength  $H$  and experiences saturation ( $M_S$ ) at complete orientation of all magnetic moments with the field (*Figure 3*). When the field is reset to zero, the system maintains a remanent magnetization  $M_R$  and behaves like a permanent magnet. In order to entirely demagnetize the system, a coercive field  $H_C$  of opposite sign needs to be applied. Both parameters determine the course of the associated hysteresis loop, which encloses an area equivalent to the energy loss by heat dissipation during the magnetization cycle.

The quantity  $M_R$  and the hysteresis area are also measures for the reluctance of a material to the reversal of magnetic moments after uniform magnetization. Large hysteresis areas occur

when the mechanism of domain wall rotation is efficiently hindered, due to pronounced anisotropic effects or dislocations in the crystallographic structure. Corresponding materials are called ‘magnetically hard’ and find, among others, application as data storage media due to these unique features. It should also be noted that ferromagnets lose their structured orientation above a critical temperature, the Curie temperature, and then act like paramagnets.

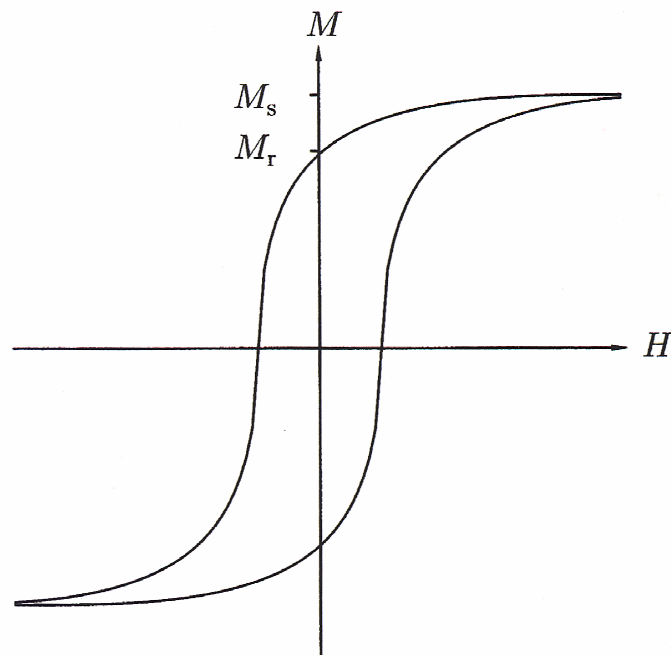


*Figure 3. Hysteresis loop for a ferro- or ferrimagnetic substance. Magnetic saturation ( $M_s$ ) is accomplished at high magnetic field strengths, due to complete alignment of magnetic moments. Field reversal to zero results in a non-zero remanent magnetization  $M_R$  [42].*

### **Ferrimagnetism**

Ferrites, for which this phenomenon was initially described, and garnets belong to the family of ferrimagnets. The domains of these systems can be imagined to be composed of two interpenetrating sublattices bearing magnetic moments of antiparallel alignment. Unlike in

antiferromagnets, the different magnitude of opposed moments or their non-equivalent distribution among the compartments result in the appearance of spontaneous magnetization.

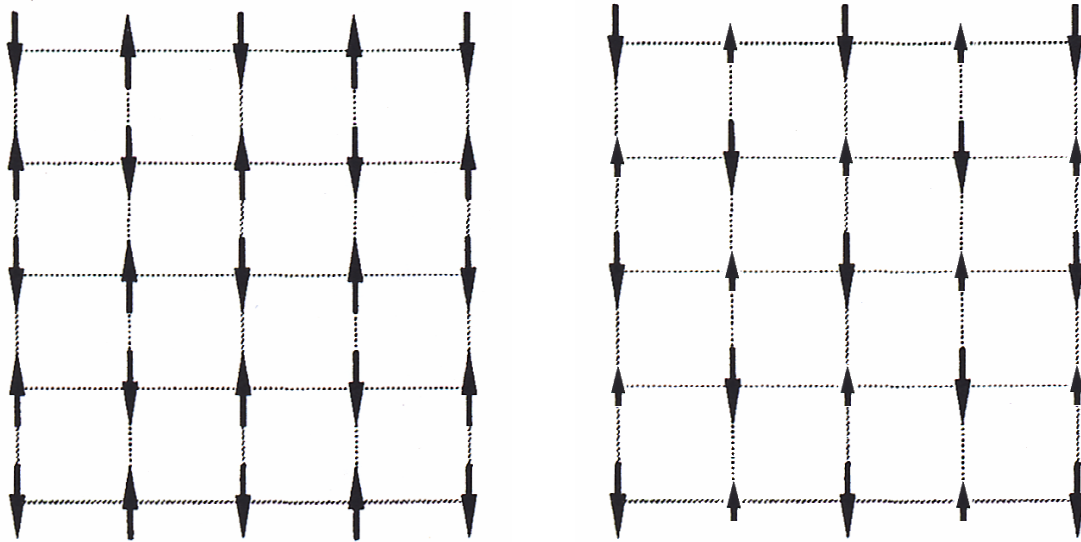


*Figure 4. Schematic composition of antiferromagnetic (left) and ferrimagnetic (right) materials. The system assemblies can be considered as two interpenetrating sublattices with opposite alignment of magnetic moments. In antiferromagnets, the magnetic moments of the sublattices are equal and therefore cancel out [42].*

Considering further the partitioning into domains, it is not surprising that the magnetization dependence on the field very much resembles that of ferromagnets. The same applies for the influence of temperature, with the exception that some ferrimagnetic materials exhibit a compensation temperature at which the two sublattices gain equal moments.

Ferrites are compounds of the basic chemical formula  $MO \cdot Fe_2O_3$  where M is a divalent cation like  $Zn^{2+}$ ,  $Fe^{2+}$ ,  $Mn^{2+}$ ,  $Ni^{2+}$ ,  $Cu^{2+}$  or  $Co^{2+}$ . Magnetite ( $Fe_3O_4$ ) and the related defect crystal maghemite ( $\gamma-Fe_2O_3$ ) are part of this group, and their structures are briefly highlighted due to their relevance for the experimental section. The general spinel structure contains two types of lattice sites, namely tetrahedral (or A) sites and octahedral (or B) sites. Cations of the A

sublattice are surrounded by four oxygen neighbors, while B site cations are coordinated by six oxygen atoms.

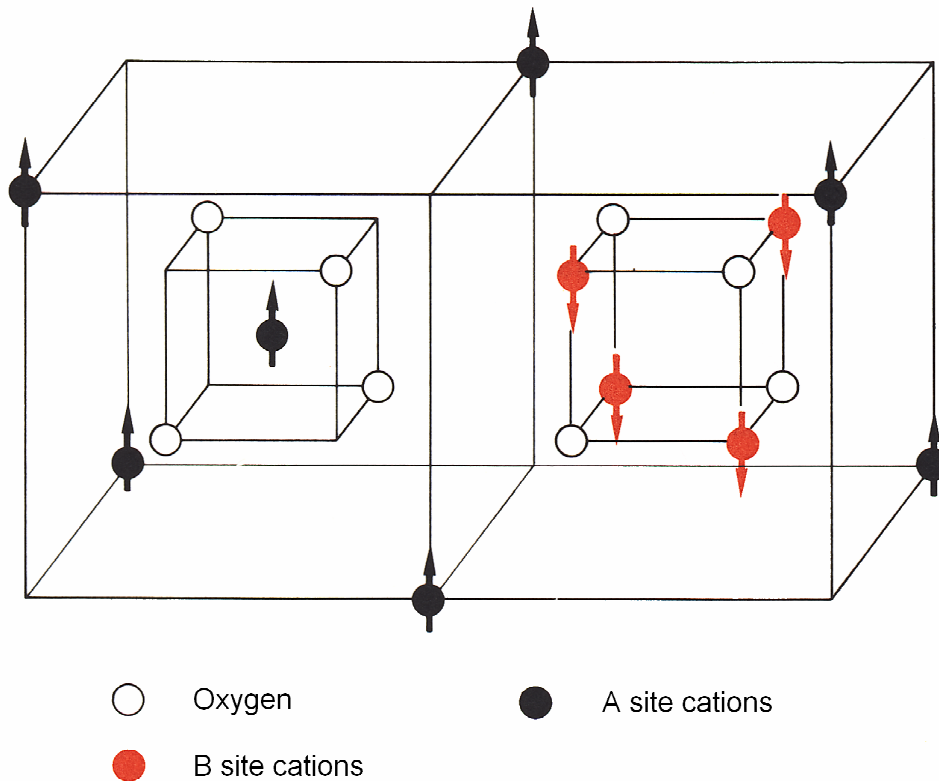


*Figure 5. Ferrimagnetic coupling of magnetic moments in a spinel. The orientation of the moments is parallel in each sublattice and antiparallel between the sublattices [43].*

Magnetite forms an inverse spinel in which  $\text{Fe}^{2+}$  ions occupy half the B sites, while the  $\text{Fe}^{3+}$  ions sit at the other half of the B sites and all the A sites [45]. With all the octahedral moments aligned in parallel fashion, due to superexchange interactions, and the tetrahedral moments pointing to the antiparallel direction, an approximation for the saturation magnetization of the formula unit can be given subtractively in multiples of the Bohr magneton:  $2(0.5 \cdot 5 + 0.5 \cdot 4) \mu_B - 5 \mu_B = 4 \mu_B$ . The factor 2 is explained by the existence of twice as many B sites as A sites in the crystal. The structure of maghemite is very similar and often represented by the formula  $\text{Fe}^{3+}_8 (\text{Fe}^{3+}_{13/3} \text{Fe}^{3+}_{2/3}) \text{O}_{32}$ . This means that only trivalent iron is present in the crystal lattice and that vacancy ordering occurs at the octahedral sites where statistically only

13 1/3 sites are occupied. The saturation magnetization per formula unit of maghemite amounts to  $2.5 \mu_B$ .

### Superparamagnetism

The formation of domains in ferro- and ferrimagnetic materials is driven by energetic considerations. Although the introduction of domain walls costs energy, the associated saving in magnetostatic energy renders it favorable. This equilibrium shifts when the sample dimensions are reduced, and below a critical diameter  $D_c$  the material consists of a single domain [46]. Inside particles of single-domain size, the magnetization is forced to lie along so-called easy axes due to magnetocrystalline and shape anisotropy reasons. In order to flip the magnetization between these preferred directions, an energy barrier  $\Delta E$  has to be overcome, which depends on the effective anisotropy constant  $K_{eff}$  and the particle volume  $V$ :

$$\Delta E = K_{eff} V . \quad (\text{Eq. 9})$$

For nanoscale objects, the energy barrier is small in comparison to the thermal energy  $k_B T$  and the magnetization can fluctuate easily. In case  $k_B T \gg K_{eff} V$ , the systems behave like paramagnets with giant non-interacting magnetic moments, hence the expression superparamagnetism [47]. The reversal time  $\tau$  of the magnetic moments is given by the Néel-Brown expression

$$\tau = \tau_0 \exp \left( \frac{K_{eff} V}{k_B T} \right) , \quad (\text{Eq. 10})$$

where  $\tau_0$  is typically  $10^{-9}$  s. If the reversal time is much longer than the observational time of a laboratory experiment, the magnetic moments of the system appear to be locked in a certain direction. This macroscopic blockade is maintained below the blocking temperature  $T_B$  which separates the blocked from the superparamagnetic state. Apart from its dependence on particle size, effective anisotropy constant and measuring time,  $T_B$  is also manipulated by the applied



field. The field lowers the energetic barrier for moment reversal, and thus the blocking temperature.

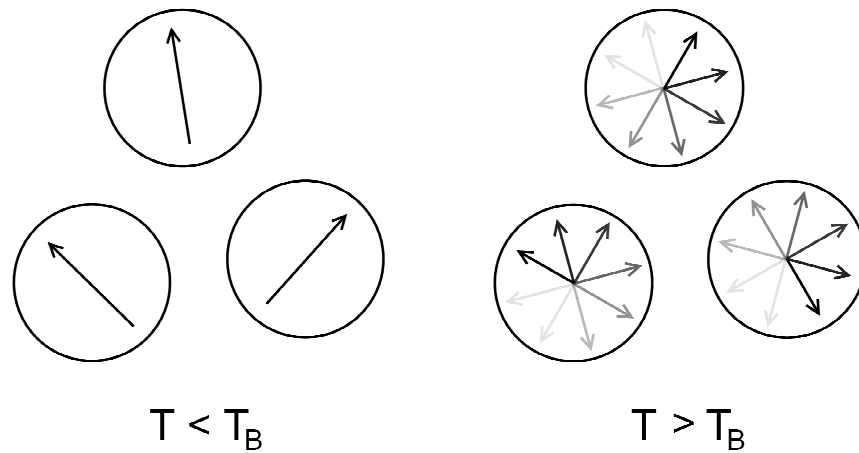


*Figure 6. Temperature influence on the magnetic behavior of superparamagnetic materials. Below the blocking temperature  $T_B$  (left), single-domain magnetic moments are blocked. Increase of temperature above  $T_B$  (right) leads to reversal of the magnetic moments at time scales shorter than the experimental time.*

Particles for biomedical applications are usually fabricated in such a way that their moments are available in the superparamagnetic state at room temperature. Then, the application of a field will align the strong magnetic moments and result in a designated effect. Moreover, the absence of any remanent magnetization upon removal of the field prevents the aggregation of the carriers, and turns them into perfectly switchable devices.

### **Magnetization measurements**

Experimental techniques for examining the magnetic properties of solids are numerous. Basically, these techniques differ with regard to their working principle and their sensitivity. Two devices most frequently used are the vibrating sample magnetometer (VSM) and the SQUID magnetometer. Both methods are based on the recording of an induction effect caused by the movement of a magnetic sample [48].

---

In a VSM, a sample vibrates sinusoidally up and down, and thereby induces an alternating current in a stationary pick-up coil. The induced signal is proportional to the magnetic moment of the sample and has the same frequency as the vibration pulse. Therefore, it can be easily filtered out by a lock-in amplifier fed with a vibration reference signal. SQUID (superconducting quantum interference device) magnetometry is one of the most sensitive techniques for the determination of magnetic dipoles. Initially, the alteration of the magnetic flux upon movement of a magnetic sample along the axis of a superconducting pick-up coil is registered. This flux information is then transferred via a coupling coil to the central component of the magnetometer, namely the SQUID sensor. The sensor completes the transformation of the flux signal into an electrical voltage. A dc-SQUID consists of a superconducting ring which is interrupted at two positions by Josephson junctions. When the intrinsic current in the respective halves of the ring is affected by a change in the magnetic flux, a voltage drop becomes detectable at the contacts. Magnetic fields as small as  $10^{-15}$  T can be measured with modern SQUID magnetometers [49].

The most direct information on the arrangement of magnetic moments inside a specimen can be achieved by neutron diffraction. The wavelength of neutrons is related to their velocity and can be tuned thermally to values similar to atomic spacings. Incident neutron beams are scattered on the one hand by atomic nuclei (nuclear scattering) and on the other hand by variations in the magnetic field (magnetic scattering). This is somewhat surprising, since neutrons do not interact with electron clouds due to their zero charge. In fact, the magnetic scattering is brought about by the coupling of atomic magnetic moments with those of neutrons. Various events can be revealed by the recorded diffraction patterns: the magnetization of a sample results in additional peaks, while a change in strength of magnetic order causes a change in amplitude. Moreover, neutron diffraction can be applied to determine the arrangement of magnetic moments in an ordered crystal [42]. Despite all these

---

possibilities, the acceptance of this method is rather cautious, due to the fact that neutron generation is very expensive.

### **PRINCIPLES IN MAGNETIC RESONANCE IMAGING (MRI)**

Atomic nuclei of non-zero spin configuration also carry magnetic moments. However, these moments are negligibly small in comparison to those of electrons. Sensitive techniques, such as magnetic resonance imaging (MRI), are able to detect such faint nuclear moments via excitation under resonance conditions. MRI represents a noninvasive imaging routine for the detailed visualization of body structures, and is particularly suitable for the high-contrast depiction of soft tissues. Selective focusing during the recording procedure enables the production of sectional images of the area of interest. The individual pictures are finally put together to yield three-dimensional models of the investigated zone. A further benefit is that MRI involves no ionizing radiation. The scientists and later Nobel Prize winners Paul C. Lauterbur and Sir Peter Mansfield extended the ideas of nuclear magnetic resonance for imaging purposes, and were leading in the development of MRI. The central role in clinical MRI is played by hydrogen nuclei which consist of a single proton and appear ubiquitously in the human body.

The rotation of protons around their own axis, better known as proton spin, creates a permanent magnetic moment parallel to the rotational axis of the spins. Upon application of a magnetic field  $B_0$ , the magnetic moments react with a precession motion around the field at a characteristic Larmor frequency  $\omega_0$  which is given by

$$\omega_0 = \gamma B_0 , \quad (\text{Eq. 11})$$

wherein  $\gamma$  is the gyromagnetic ratio. The subtle loss of energy during precession forces the moments to align gradually with the field, thereby creating a net longitudinal magnetization

$M_z$  along the axis of the external field. By the perpendicular input of an appropriate high frequency pulse under resonance conditions, that is at Larmor frequency, an entire  $90^\circ$  deflection of the magnetization vector to the xy plane takes place. The precession and spin motion of this transverse magnetization  $M_{XY}$  induces an oscillating current in the detector coil, which is amplified to give the MR signal.

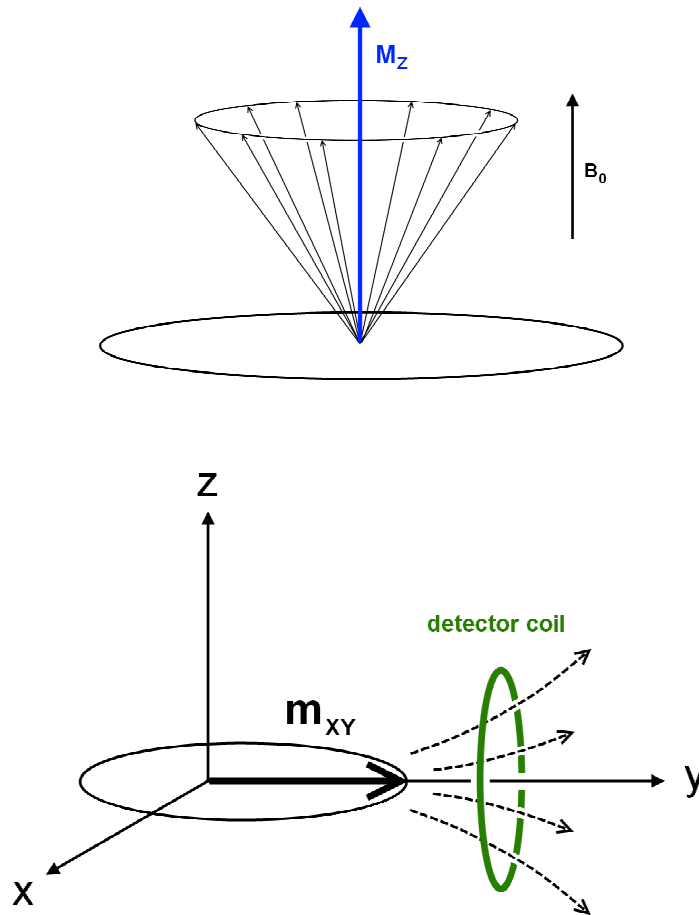


Figure 7. Precession movement of magnetic moments in an external field  $B_0$  results in a net longitudinal magnetization  $M_z$  (top). After application of a high frequency pulse, the magnetization vector flaps to the xy plain and induces a signal in the detector coil (bottom).

After removal of the high frequency pulse, the modulus of the transverse magnetization and thus the oscillation amplitude decrease with time, due to special relaxation mechanisms, and the resultant fading of the signal is known as free induction decay [50].

The processes leading to the decay of transverse magnetization are referred to as spin-lattice relaxation and spin-spin relaxation. Other denominations are  $T_1$  and  $T_2$  relaxation, respectively. Spin-lattice relaxation appears due to energy exchange between the spin system and the surrounding lattice. This causes a progressive realignment with the external field, and a recovery of the longitudinal magnetization  $M_Z$  in such a way that

$$M_Z = M_0(1 - e^{-t/T_1}) , \quad (\text{Eq. 12})$$

where  $M_0$  is the magnetization along the external field at equilibrium state and  $T_1$  is the so-called longitudinal relaxation time.

Simultaneously, spin-spin relaxation weakens the transverse magnetization by dephasing of the spins. The loss of phase coherence can be attributed primarily to the energy exchange among the spins, which is known as pure spin-spin interaction, but it can also be due to constant inhomogeneities in the external magnetic field. The time constant  $T_2$  for the pure spin-spin interaction is given by

$$M_{XY} = M_{XY'}(1 - e^{-t/T_2}) , \quad (\text{Eq. 13})$$

where  $M_{XY'}$  is the maximum magnetization in transverse direction. In case the contribution of field inhomogeneities cannot be eliminated, the time for the relaxation process is generally shortened and expressed as transverse relaxation time  $T_2^*$ .

As  $T_2$  relaxation is a much faster process than  $T_1$  relaxation, the observed signal loss after a single high frequency pulse is dominated by the transverse dephasing. However, when multiple excitations are performed during a measurement cycle, the weighting between these parameters can be shifted [50]. In this connection, the settings of both the repetition time  $T_R$  and the echo time  $T_E$  of a measurement sequence have a strong impact. The quantity  $T_R$  is defined as the time interval between two consecutive excitations of a section of interest. In order to attain a so-called  $T_1$  weighting, that is the assessment of contrast due to the different longitudinal relaxations of certain tissues, the repetition time should be kept rather small.

---

After a short  $T_R$ , the magnetization vectors  $M_Z$  of different tissues accessible for further excitations vary the most, and consequently, the highest possible contrast of signals is achieved.

The echo time  $T_E$  specifies the time range between excitation and registration of the MR signal. The later the registration happens, the more pronounced the differences in spin dephasing for the investigated tissues due to unequal  $T_2$  relaxation times. Therefore, the type of image acquisition with a combination of long repetition time and long echo time is called  $T_2$ -weighted. In contrast,  $T_1$  weighting is accomplished by small values of  $T_R$  and  $T_E$ . A typical set of scan parameters for a  $T_2$ -weighted sequence would contain a repetition time  $T_R$  between 3000 and 5000 ms and  $T_E$  in the range of 80 to 150 ms. [51]

The choice of the MRI sequence is sometimes crucial for the detection of malignant masses [52]. This is because the differences in absolute signal values are dependent on the respective sequence, but have to be maximal for the tissue areas examined, in order to allow for sufficient contrast and distinguishability.

Spin echo sequences are a method to eliminate the abovementioned magnetic field disturbances and their influence on the spin relaxation behavior, respectively. After standard excitation with a  $90^\circ$  pulse, the signal decays due to spin dephasing. A second  $180^\circ$  inversion pulse reverses the spins in the xy plane, whereupon they start to rephase again. Complete phase coherence is obtained after  $T_E$ , and the amplitude swelling of the echo signal is a measure for the pure spin-spin relaxation (*Figure 8*).

As already pointed out, the selection of the pulse sequence is a major factor affecting image contrast in MRI studies. The contrast is further determined by the individual physique of the patients, the technical specifications of the scanning device and the effect of MRI contrast agents.

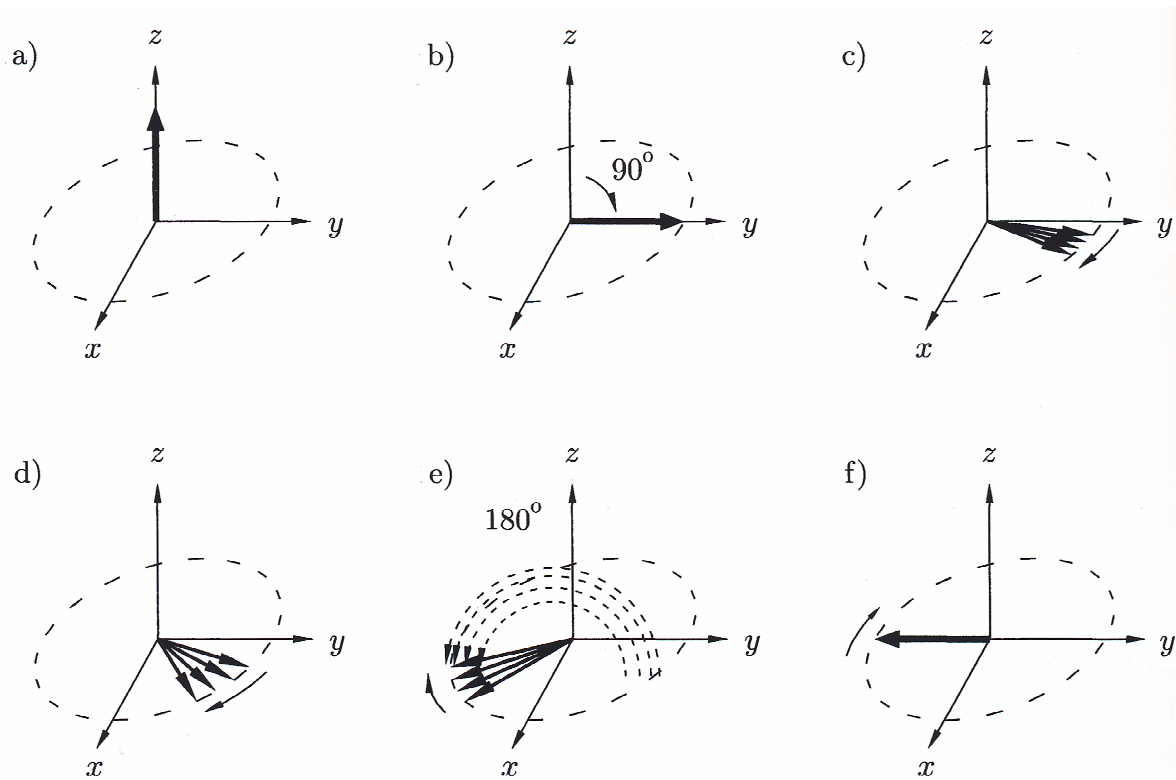
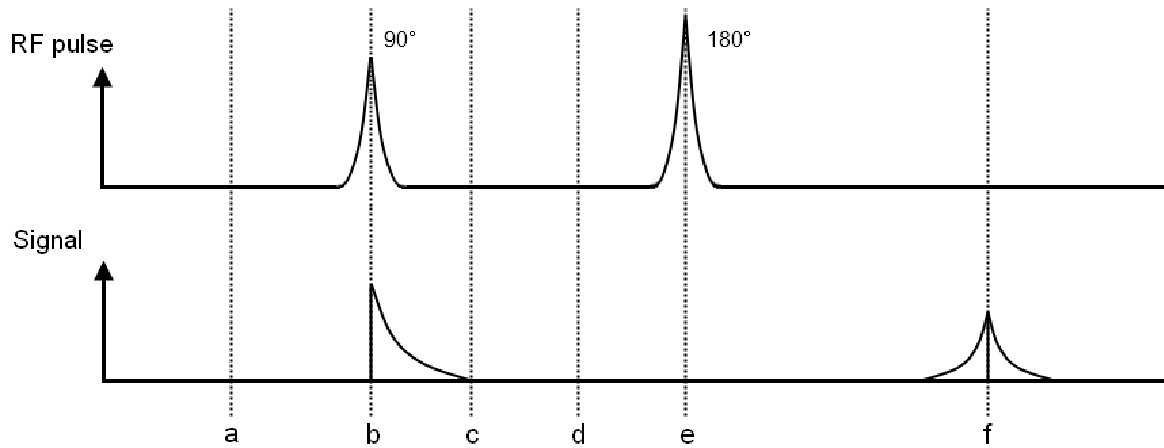


Figure 8. Timing of RF pulses and signal of detector coil during MRI spin echo sequence (upper chart). The spin echo effect (lower chart): (a) The equilibrium magnetization initially lies along the  $z$ -direction. (b) Magnetization precession in the  $xy$  plain after  $90^\circ$  pulse ( $t = 0$ ). (c)(d) Gradual spin dephasing because of field inhomogeneities. (e) Spin reversal and beginning rephasing after application of  $180^\circ$  pulse ( $t = \tau$ ). (f) Complete rephasing of spins at  $t = 2\tau$ - spin echo signal [42].

---

## MRI CONTRAST AGENTS

Contrast agents are a group of pharmaceuticals used to enhance the visibility of internal body structures, and to elaborate faint differences in the signal intensity of adjacent tissues. In general, the brightness (or darkness) of a tissue results additively from its proton density and its resonance behavior. While the first item is rather difficult to manipulate, the relaxation properties can be altered by means of most contrast enhancers. This is due to the generation of local magnetic fields which interact with the surrounding protons. For paramagnetic MRI contrast agents, the interaction is a combination of inner- and outersphere relaxation, whereas the latter mechanism dominates for superparamagnetic agents [6]. Outersphere relaxation is mediated by the movement of water protons in the vicinity of the generated magnetic field gradients, and has a strong effect on the transverse relaxation.

On this basis, MRI contrast agents are classified into positive and negative contrast enhancers. Paramagnetic agents mainly accelerate the longitudinal  $T_1$  relaxation and cause a hypersignal in the region of interest. Due to this brightening effect, they are called positive contrast agents. In contrast, superparamagnetic formulations induce rapid spin dephasing and thus massive shortening of the  $T_2$  relaxation time [53]. Tissues containing minimum levels of these agents appear darker in appropriate sequences. Therefore, such agents are also referred to as negative contrast agents.

Most positive contrast agents contain the paramagnetic gadolinium ion in chelated form. The attachment of strong chelators reduces the toxic potential of gadolinium, and permits the intravasal application of the complex solutions. The indications for gadolinium complexes range from whole-body imaging and angiography, to the detection of focal liver lesions. Several marketed products have been approved by the FDA, such as Omniscan® and Magnevist®.



Nanosuspensions of superparamagnetic iron oxide modifications have found application as negative contrast agents in the past decade (*Table 2*). The approved ferrofluids contain magnetite or maghemite nanoparticles of different dimensions, which are surrounded by macromolecular stabilizers. The surface coverage with these molecules prevents the particles from aggregation, and optionally enables the prolongation of blood residence time, due to the hindrance of plasma protein opsonization. Depending on their size, the coated nanoparticles tend to accumulate in different compartments of the body. While nanoparticles of very small dimensions (< 40 nm) concentrate in the lymph nodes after 24 hours, larger nanoparticles of around 100 nm are rapidly taken up by the reticuloendothelial system. As sufficient tissue enrichment is necessary for effective contrast enhancement, the indications follow from the respective pharmacokinetic distributions in the body.

Trade name	Manufacturer	Specifications	Indication	Dosage
Endorem®	Guerbet S.A.	Fe <sub>3</sub> O <sub>4</sub> / Dextran 11.2 mg [Fe] per mL	Liver lesions	15 µmol [Fe] per kg body weight
Lumirem®	Guerbet S.A.	Fe <sub>3</sub> O <sub>4</sub> / APTMS 0.18 mg [Fe] per mL	GI tract, bowel delineation	600 – 900 mL (oral) 300 – 600 mL (rectal)
Resovist®	Bayer Schering	Fe <sub>3</sub> O <sub>4</sub> / γ-Fe <sub>2</sub> O <sub>3</sub> / Carboxydextran 0.5 mmol [Fe] per mL	Liver lesions	0.45 – 0.7 mmol [Fe] (intravenous)

APTMS : [3-(2-Aminoethylamino)propyl]trimethoxysilane

*Table 2. Marketed contrast agents based on magnetic iron oxide nanoparticles.*

---

## MANUFACTURING TECHNIQUES

Several procedures for the fabrication of magnetic nanoparticles are available nowadays [5]. The selection of the appropriate synthesis route is a crucial step, due to the fact that it affects composition, shape and crystallinity of the products. Further features directing the decision are the eventual application, yield and particle uniformity. The most important methods for synthesizing nanoparticles of the iron oxide species  $\text{Fe}_3\text{O}_4$  and  $\gamma\text{-Fe}_2\text{O}_3$  are aqueous coprecipitation and thermal decomposition (*Table 3*).

Coprecipitation is a convenient way to synthesize magnetic iron oxides from aqueous iron salt solutions by the simple addition of a base. The dimensions and the size distribution of the nanoparticular products can be regulated by a series of settings, among these the iron(II)/iron(III) ratio, type of iron salts used, pH and temperature [47]. In case the reaction is carried out under inert atmosphere, crystalline magnetite is formed as a product. Due to its susceptibility to air oxidation, magnetite is either stored under appropriate conditions or deliberately oxidized to also magnetic  $\gamma\text{-Fe}_2\text{O}_3$ . Despite all scientific efforts, control of particle size remains the weak point of the coprecipitation method. Basic approaches for solving this problem contain the *in situ* stabilization of nanoparticles by polymers or carbohydrates during the precipitation process [54]. Uniform crystal growth can further be mediated by the use of special chelating agents [55]. A great advantage of the coprecipitation method with respect to biomedical applications is the complete lack of organic solvents. However, the prepared magnetic nanoparticles first have to be stabilized by protecting surfactant or polymer coatings, before they can be administered.

Monodisperse iron oxide nanoparticles with high size control can be synthesized by the thermal decomposition of organometallic precursors like iron pentacarbonyl  $\text{Fe}(\text{CO})_5$  or iron acetylacetonate  $\text{Fe}(\text{acac})_3$ . The reactions are carried out under the presence of surfactants in high-boiling organic solvents, and yield either pure metal or iron oxide nanoparticles,

---

depending on the valence of the precursor molecules. Initially formed metal nanoparticles can be easily converted to their oxides in a consecutive step. For example, Hyeon et al. prepared monodisperse  $\gamma$ -Fe<sub>2</sub>O<sub>3</sub> nanocrystals by thermal decomposition of Fe(CO)<sub>5</sub> in a mixture of octyl ether and oleic acid at 100 °C and subsequent oxidation of the intermediate by the addition of trimethylamine oxide [56]. In general, the dimensional and morphological properties of the nanoparticles are precisely tunable by controlling the reaction times and the temperature, as well as the concentrations and ratios of the employed reactants. In order to render the hydrophobic magnetic nanoparticles water-dispersible, polar molecules have to be introduced. This is managed, for example, by the exchange of surface ligands or the intercalation of amphiphilic molecules between stabilizer chains.

Droplets inside water-in-oil microemulsions can serve as nanoreactors for the formation of iron oxide nanoparticles. The dimensions of the surfactant-stabilized water droplets are determined by the ratio of surfactant to water [57]. Consequently, the size of the nanoparticles can be controlled to a high extent. A popular pattern occurring in many synthesis protocols comprises the isovolumetric mixing of two analog microemulsions, one containing an iron salt solution, the other containing an alkaline precipitation agent [58]. The hydrophobic nanoparticles are recovered by acetone and ethanol treatment, and are readily dispersible in organic solvents.

Besides the presented strategies, a multitude of methods are available for the fabrication of magnetic iron oxide nanoparticles, such as sol-gel reactions, hydrothermal synthesis and laser pyrolysis. Nevertheless, progress in this field is still ongoing. In microfluidic systems, reactants are compartmentalized in droplets and systemically fused by electrocoalescence. The generated nanoparticles exhibited very small sizes and narrow size distributions [59].

Synthetic method	Reaction temperature [°C]	Solvent	Shape control	Yield
coprecipitation	20 – 90	water	–	high / scalable
thermal decomposition	100 – 320	organic compound	++	high / scalable
microemulsion	20 – 50	organic compound	+	low
hydrothermal synthesis	220	water-ethanol	++	medium

*Table 3. Synthesis routes for the generation of magnetic (iron oxide) nanoparticles.*

---

**OBJECTIVE OF THE STUDY**

The general objective of the present work was the development of a novel ferrofluid of high versatility for biomedical applications. Here, the main focus was on the suitability of designed formulations to operate as effective contrast agents in MRI studies. Our goal was to optimize these formulations in terms of functionality, selectivity and biocompatibility in order to overcome limitations of currently marketed MRI contrast agents. The overall process involved the synthesis and stabilization of ferrofluidic nanosuspensions based on magnetic  $\gamma$ -Fe<sub>2</sub>O<sub>3</sub> as well as the evaluation of their compliance with the technological requirements necessary for an effective *in vivo* application.

**Chapter 1** provides background information on the status quo of magnetic nanoparticles in various biomedical disciplines. Furthermore, general aspects of particular relevance for the better understanding of the topic are addressed, among these basic principles of magnetochemistry and magnetic resonance imaging, with the aim of imparting more transparency to the reader.

In order to be qualified for biomedical applications, magnetic nanoparticles have to meet certain requirements. These include small size, monodispersity, high magnetization values, superparamagnetism and peculiar surface coating. The role of surfactant choice is not to be underestimated, since these agents provide stabilization, protection, functionalization and biocompatibility. Accordingly, it was our goal to generate nanoparticulate iron oxide formulations matching the specified features the best way possible. We assumed that appropriate selection and subsequent tuning of the synthesis route could maximize magnetic and relaxation properties of the nanocarriers. Furthermore, the implementation of a new class of surface stabilizers was supposed to confer combined compatibility and versatility to the magnetic carriers. In **Chapter 2**, respective experiments highlighting the influence of both synthesis procedure and stabilizer choice on the performance of magnetic nanoparticles are

---

described. Iron oxide nanoparticles were synthesized by an aqueous coprecipitation process, and thoroughly characterized with regard to their specifications. For the purpose of comparison, the magnetic cores were coated with either poly(ethylene imine), a standard polymer for the stabilization of iron oxide nanoparticles, or the grafted derivative poly(ethylene imine)-*g*-poly(ethylene glycol). It was hypothesized that the modification of nanoparticles with a surface stabilizer carrying PEG moieties would enhance the colloidal stability in protein-rich environments, and lead to a reduction in cytotoxicity. In addition, the relaxation parameters of the formulations were investigated in order to reveal the potential effectiveness in MRI contrast enhancement. As relaxation is a physical property brought about by the magnetic part of the compounds, we assumed it to be independent of the respective coating agent. Were the assumptions to be validated, the novel iron oxide formulation containing poly(ethylene imine)-*g*-poly(ethylene glycol) would possibly be able to compete with presently marketed MRI contrast agents.

The investigations described in **Chapter 3** move the focus to the cellular uptake of oppositely charged magnetic iron oxide nanoparticles. Based on the fact that the surface potentials of nanoparticulate systems severely affect their cell internalization rate and mechanism, we anticipated a major difference in accumulation behavior and possibly cell-internal distribution in comparative uptake studies. Moreover, we attempted to reveal implications of cellular localization for the relaxometric performance of magnetic nanoparticles. For that purpose, particle-loaded cells were subjected to different MRI sequences, in order to evaluate the contrast enhancement potential of the ferrofluids. The setups of the examined formulations differed in both the charge of the polymeric stabilizer and the applied synthesis route. Therefore, we assumed the cell uptake kinetics and rate to be a cooperative effect of several variables, but governed by surface charge. It was further hypothesized that accumulation of positively charged iron oxide nanoparticles would occur at a faster rate, and to a higher extent. In general, a pronounced uptake does not necessarily improve the signaling of a tissue in MRI

---

sequences, due to the detrimental effect of cell compartmentalization. However, we predicted this effect to be less pronounced for formulations with the potential for endosomal escape, such as the applied compounds of iron oxide and poly(ethylene imine). Such formulations were suggested to be highly valuable for applications such as stem cell tracking, which do require high cell loading levels with contrast agents and sufficient MRI signaling.

---

**REFERENCES**

- [1] Nagesha, D., Devalapally, H., Sridhar, S., Amiji, M., 2008. Multifunctional Magnetic Nanosystems for Tumor Imaging, Targeted Delivery and Thermal Medicine. In: Torchilin, V. (ed). *Multifunctional Pharmaceutical Nanocarriers*, New York: Springer, 381-408.
- [2] Peer, D., Karp, J.M., Hong, S., Farokhzad, O.C., Margalit, R., Langer, R., 2007. Nanocarriers as an emerging platform for cancer therapy. *Nat. Nanotechnol.* 2, 751-760.
- [3] Alexiou, C., Jurgons, R., Seliger, C., Iro, H., 2006. Medical applications of magnetic nanoparticles. *J. Nanosci. Nanotechnol.* 6, 2762-2768.
- [4] Mornet, S., Vasseur, S., Grasset, F., Veverka, P., Goglio, G., Demourgues, A., Portier, J., Pollert, E., Duguet, E., 2006. Magnetic nanoparticle design for medical applications. *Prog. Solid State Chem.* 34, 237-247.
- [5] Tartaj, P., Morales, M.d.P., Veintemillas-Verdaguer, S., Gonzalez-Carreno, T., Serna, C.J., 2003. The preparation of magnetic nanoparticles for applications in biomedicine. *J. Phys. D: Appl. Phys.* 36, R182-R197.
- [6] Laurent, S., Forge, D., Port, M., Roch, A., Robic, C., Vander Elst, L., Muller, R.N., 2008. Magnetic Iron Oxide Nanoparticles: Synthesis, Stabilization, Vectorization, Physicochemical Characterizations, and Biological Applications. *Chem. Rev.* 108, 2064-2110.



- 
- [7] Veiseh, O., Gunn, J.W., Zhang, M., Design and fabrication of magnetic nanoparticles for targeted drug delivery and imaging. *Adv. Drug Delivery Rev.* 62, 284-304.
- [8] Alexis, F., Pridgen, E., Molnar, L.K., Farokhzad, O.C., 2008. Factors Affecting the Clearance and Biodistribution of Polymeric Nanoparticles. *Mol. Pharmaceutics* 5, 505-515.
- [9] Duguet, E., Vasseur, S., Mornet, S., Devoisselle, J.-M., 2006. Magnetic nanoparticles and their applications in medicine. *Nanomedicine* 1, 157-168.
- [10] Wang, M., Thanou, M., Targeting nanoparticles to cancer. *Pharmacol. Res.* 62, 90-99.
- [11] Bae, Y.H., 2009. Drug targeting and tumor heterogeneity. *J. Controlled Release* 133, 2-3.
- [12] Godin, B., Serda, R.E., Sakamoto, J., Decuzzi, P., Ferrari, M., 2009. Nanoparticles for Cancer Detection and Therapy. In: Vogel, V. (ed). *Nanotechnology, Volume 5: Nanomedicine*, Weinheim: Wiley VCH, 51-88.
- [13] McCarthy, J.R., Kelly, K.A., Sun, E.Y., Weissleder, R., 2007. Targeted delivery of multifunctional magnetic nanoparticles. *Nanomedicine* 2, 153-167.
- [14] Weissleder, R., Kelly, K., Sun, E.Y., Shtatland, T., Josephson, L., 2005. Cell-specific targeting of nanoparticles by multivalent attachment of small molecules. *Nat. Biotechnol.* 23, 1418-1423.

- 
- [15] Gupta Ajay, K., Gupta, M., 2005. Synthesis and surface engineering of iron oxide nanoparticles for biomedical applications. *Biomaterials* 26, 3995-4021.
- [16] Natarajan, A., Gruettner, C., Ivkov, R., DeNardo, G.L., Mirick, G., Yuan, A., Foreman, A., DeNardo, S.J., 2008. NanoFerrite Particle Based Radioimmunonanoparticles: Binding Affinity and In Vivo Pharmacokinetics. *Bioconjugate Chem.* 19, 1211-1218.
- [17] Williams, R.O., Sinswat, P., 2008. Recent Advances in Nanoparticle-based Drug Delivery Technologies and Their Applications for Particulate Drug Delivery Systems. In: Ravi Kumar, M.N.V. (ed). *Handbook of Particulate Drug Delivery, Volume 1: Materials and Technologies*, Los Angeles: American Scientific Publishers.
- [18] Ritter, J.A., Ebner, A.D., Daniel, K.D., Stewart, K.L., 2004. Application of high gradient magnetic separation principles to magnetic drug targeting. *J. Magn. Magn. Mater.* 280, 184-201.
- [19] Fernandez-Pacheco, R., Valdivia, J.G., Ibarra, M.R., 2009. Magnetic nanoparticles for local drug delivery using magnetic implants. *Methods Mol. Biol.* 544, 559-569.
- [20] Dames, P., Gleich, B., Flemmer, A., Hajek, K., Seidl, N., Wiekhorst, F., Eberbeck, D., Bittmann, I., Bergemann, C., Weyh, T., Trahms, L., Rosenecker, J., Rudolph, C., 2007. Targeted delivery of magnetic aerosol droplets to the lung. *Nat. Nanotechnol.* 2, 495-499.

- 
- [21] Jordan, A., Wust, P., Faehling, H., John, W., Hinz, A., Felix, R., 2009. Inductive heating of ferrimagnetic particles and magnetic fluids: Physical evaluation of their potential for hyperthermia. *Int. J. Hyperthermia* 25, 499-511.
- [22] Jordan, A., Maier-Hauff, K., Wust, P., Rau, B., Johannsen, M., 2007. Thermotherapie mit magnetischen Nanopartikeln. *Onkologe* 13, 894-902.
- [23] Suto, M., Hirota, Y., Mamiya, H., Fujita, A., Kasuya, R., Tohji, K., Jeyadevan, B., 2009. Heat dissipation mechanism of magnetite nanoparticles in magnetic fluid hyperthermia. *J. Magn. Magn. Mater.* 321, 1493-1496.
- [24] Gonzales-Weimuller, M., Zeisberger, M., Krishnan, K.M., 2009. Size-dependant heating rates of iron oxide nanoparticles for magnetic fluid hyperthermia. *J. Magn. Magn. Mater.* 321, 1947-1950.
- [25] Sonvico, F., Mornet, S., Vasseur, S., Dubernet, C., Jaillard, D., Degrouard, J., Hoebeke, J., Duguet, E., Colombo, P., Couvreur, P., 2005. Folate-Conjugated Iron Oxide Nanoparticles for Solid Tumor Targeting as Potential Specific Magnetic Hyperthermia Mediators: Synthesis, Physicochemical Characterization, and in Vitro Experiments. *Bioconjugate Chem.* 16, 1181-1188.
- [26] Johannsen, M., Gneveckow, U., Thiesen, B., Taymoorian, K., Cho Chie, H., Waldofner, N., Scholz, R., Jordan, A., Loening Stefan, A., Wust, P., 2007. Thermotherapy of prostate cancer using magnetic nanoparticles: feasibility, imaging, and three-dimensional temperature distribution. *Eur Urol* 52, 1653-1661.

- 
- [27] Nanostart: MagForce receives EU approval for nano cancer therapy. Retrieved Oct 10, 2010. [http://www.nanostart.de/images/pdf/magforce\\_czerwensky\\_20100630.pdf](http://www.nanostart.de/images/pdf/magforce_czerwensky_20100630.pdf)
- [28] Thorek, D.L.J., Czupryna, J., Chen A.K., Tsourkas A., 2008. Molecular Imaging of Cancer with Superparamagnetic Iron-Oxide Nanoparticles. In: Hayat M.A. (ed), Cancer Imaging, Volume 2: Instrumentation and Applications, London: Elsevier Academic Press, 85-96.
- [29] Corot, C., Robert, P., Idee, J.-M., Port, M., 2006. Recent advances in iron oxide nanocrystal technology for medical imaging. *Adv. Drug Delivery Rev.* 58, 1471-1504.
- [30] Vogl Thomas, J., Schwarz, W., Blume, S., Pietsch, M., Shamsi, K., Franz, M., Lobeck, H., Balzer, T., del Tredici, K., Neuhaus, P., Felix, R., Hammerstingl Renate, M., 2003. Preoperative evaluation of malignant liver tumors: comparison of unenhanced and SPIO (Resovist)-enhanced MR imaging with biphasic CTAP and intraoperative US. *Eur Radiol* 13, 262-272.
- [31] Cai, W., Chen, X., 2007. Nanoplatforms for targeted molecular imaging in living subjects. *Small* 3, 1840-1854.
- [32] Fang, C., Zhang, M., Nanoparticle-based theragnostics: Integrating diagnostic and therapeutic potentials in nanomedicine. *J. Controlled Release* 146, 2-5.
- [33] Amsalem, Y., Mardor, Y., Feinberg, M.S., Landa, N., Miller, L., Daniels, D., Ocherashvilli, A., Holbova, R., Yosef, O., Barbash, I.M., Leor, J., 2007. Iron-Oxide

- 
- Labeling and Outcome of Transplanted Mesenchymal Stem Cells in the Infarcted Myocardium. *Circulation* 116, I38-I45.
- [34] Sun, C., Sze, R., Zhang, M., 2006. Folic acid-PEG conjugated superparamagnetic nanoparticles for targeted cellular uptake and detection by MRI. *J. Biomed. Mater. Res., Part A* 78A, 550-557.
- [35] Burtea, C., Laurent, S., Roch, A., Vander Elst, L., Muller, R.N., 2005. C-MALISA (cellular magnetic-linked immunosorbent assay), a new application of cellular ELISA for MRI. *J. Inorg. Biochem.* 99, 1135-1144.
- [36] Jin, A.Y., Tuor, U.I., Rushforth, D., Filfil, R., Kaur, J., Ni, F., Tomanek, B., Barber, P.A., 2009. Magnetic resonance molecular imaging of post-stroke neuroinflammation with a P-selectin targeted iron oxide nanoparticle. *Contrast Media Mol. Imaging* 4, 305-311.
- [37] Zhang, C., Jugold, M., Woenne, E.C., Lammers, T., Morgenstern, B., Mueller, M.M., Zentgraf, H., Bock, M., Eisenhut, M., Semmler, W., Kiessling, F., 2007. Specific Targeting of Tumor Angiogenesis by RGD-Conjugated Ultrasmall Superparamagnetic Iron Oxide Particles Using a Clinical 1.5-T Magnetic Resonance Scanner. *Cancer Res.* 67, 1555-1562.
- [38] Hadjipanayis, C.G., Machaidze, R., Kaluzova, M., Wang, L., Schuette, A.J., Chen, H., Wu, X., Mao, H., EGFRvIII Antibody-Conjugated Iron Oxide Nanoparticles for Magnetic Resonance Imaging-Guided Convection-Enhanced Delivery and Targeted Therapy of Glioblastoma. *Cancer Res.* 70, 6303-6312.

- 
- [39] Kinoshita, M., Yoshioka, Y., Okita, Y., Hashimoto, N., Yoshimine, T., MR molecular imaging of HER-2 in a murine tumor xenograft by SPIO labeling of anti-HER-2 affibody. *Contrast Media Mol. Imaging* 5, 18-22.
- [40] Zheng, J., Jaffray, D.A., Allen C., 2008. Nanosystems for Multimodality In vivo Imaging. In: Torchilin, V. (ed). *Multifunctional Pharmaceutical Nanocarriers*, New York: Springer, 409-430.
- [41] Bumb, A., Regino, C.A.S., Perkins, M.R., Bernardo, M., Ogawa, M., Fugger, L., Choyke, P.L., Dobson, P.J., Brechbiel, M.W., Preparation and characterization of a magnetic and optical dual-modality molecular probe. *Nanotechnology* 21, 175704/175701-175704/175709.
- [42] Blundell, S., 2001. *Magnetism in Condensed Matter*. New York: Oxford University Press.
- [43] Riedel, E., 1999. *Anorganische Chemie*, 4<sup>th</sup> edition. Berlin – New York: de Gruyter.
- [44] Tipler, P.A., 1994. *Physik*. Heidelberg: Spektrum.
- [45] Lee, S.-J., Lee, S., 2006. The spin structure of maghemite investigated by <sup>57</sup>Fe NMR. *New J. Phys.* 8, 98.
- [46] Wohlfarth, E.P., 1983. Magnetic properties of single domain ferromagnetic particles. *J. Magn. Magn. Mater.* 39, 39-44.

- 
- [47] Lu, A.H., Salabas, E.L., Schueth, F., 2007. Magnetic nanoparticles: synthesis, protection, functionalization, and application. *Angew. Chem., Int. Ed.* 46, 1222-1244.
- [48] Lueken, H., 1999. *Magnetochemie*. Stuttgart – Leipzig: B.G. Teubner.
- [49] Pannetier-Lecoeur, M. Superconducting-magneto-resistive sensor: Reaching the femtotesla at 77 K. Retrieved Oct 5, 2010.  
<http://tel.archives-ouvertes.fr/docs/00/45/34/10/PDF/HDR.pdf>
- [50] Weishaupt, D., Koechli, V.D., Marincek, B., 2009. *Wie funktioniert MRI?*, 6<sup>th</sup> edition. Heidelberg: Springer.
- [51] Ma, J., Jackson, E.F., Kumar, A.J., Ginsberg, L.E., 2009. Improving fat-suppressed T2-weighted imaging of the head and neck with 2 fast spin-echo dixon techniques: initial experiences. *AJNR Am J Neuroradiol* 30, 42-45.
- [52] Semelka, R.C., Bagley, A.S., Brown, E.D., Kroeker, M.A., 1994. Malignant lesions of the liver identified on T1- but not T2-weighted MR images at 1.5 T. *J Magn Reson Imaging* 4, 315-318.
- [53] Na, H.B., Song, I.C., Hyeon, T., 2009. Inorganic Nanoparticles for MRI Contrast Agents. *Adv. Mater.* 21, 2133-2148.
- [54] Horak, D., Babic, M., Jendelova, P., Herynek, V., Trchova, M., Pientka, Z., Pollert, E., Hajek, M., Sykova, E., 2007. D-Mannose-Modified Iron Oxide Nanoparticles for Stem Cell Labeling. *Bioconjugate Chem.* 18, 635-644.

- 
- [55] Iwasaki, T., Mizutani, N., Watano, S., Yanagida, T., Kawai, T., Size control of magnetite nanoparticles by organic solvent-free chemical coprecipitation at room temperature. *J. Exp. Nanosci.* 5, 251-262.
- [56] Hyeon, T., Lee, S.S., Park, J., Chung, Y., Na, H.B., 2001. Synthesis of Highly Crystalline and Monodisperse Maghemite Nanocrystallites without a Size-Selection Process. *J. Am. Chem. Soc.* 123, 12798-12801.
- [57] Paul, B.K., Moulik, S.P., 2001. Uses and applications of microemulsions. *Curr. Sci.* 80, 990-1001.
- [58] Chin, A.B., Yaacob, I.I., 2007. Synthesis and characterization of magnetic iron oxide nanoparticles via w/o microemulsion and Massart's procedure. *J. Mater. Process. Technol* 191, 235-237.
- [59] Frenz, L., El Harrak, A., Pauly, M., Begin-Colin, S., Griffiths, A.D., Baret, J.-C., 2008. Droplet-based microreactors for the synthesis of magnetic iron oxide nanoparticles. *Angew. Chem., Int. Ed.* 47, 6817-6820.



**Chapter 2      Novel magnetic iron oxide nanoparticles coated  
with poly(ethylene imine)-g-poly(ethylene glycol)  
for potential biomedical application:  
synthesis, stability, cytotoxicity and MR imaging**

---

---

**ABSTRACT**

Magnetic iron oxide nanoparticles have found application as contrast agents for magnetic resonance imaging (MRI) and as switchable drug delivery vehicles. Their stabilization as colloidal carriers remains a challenge. The potential of poly(ethylene imine)-*g*-poly(ethylene glycol) (PEGPEI) as stabilizer for iron oxide ( $\gamma$ -Fe<sub>2</sub>O<sub>3</sub>) nanoparticles was studied in comparison to branched poly(ethylene imine) (PEI). Carrier systems consisting of  $\gamma$ -Fe<sub>2</sub>O<sub>3</sub>-PEI and  $\gamma$ -Fe<sub>2</sub>O<sub>3</sub>-PEGPEI were prepared and characterized with regard to their physicochemical properties, including magnetic resonance relaxometry. Colloidal stability of the formulations was tested in several media, and cytotoxic effects in adenocarcinomic epithelial cells were investigated.

Synthesized  $\gamma$ -Fe<sub>2</sub>O<sub>3</sub> cores showed superparamagnetism and high degree of crystallinity. Diameters of polymer-coated nanoparticles  $\gamma$ -Fe<sub>2</sub>O<sub>3</sub>-PEI and  $\gamma$ -Fe<sub>2</sub>O<sub>3</sub>-PEGPEI were found to be  $38.7 \pm 1.0$  nm and  $40.4 \pm 1.6$  nm, respectively. No aggregation tendency was observable for  $\gamma$ -Fe<sub>2</sub>O<sub>3</sub>-PEGPEI over 12 hours, even in high ionic strength media. Furthermore, IC<sub>50</sub> values were significantly increased by more than 10-fold, when compared to  $\gamma$ -Fe<sub>2</sub>O<sub>3</sub>-PEI. Formulations exhibited  $r_2$  relaxivities of high numerical value, namely around  $160 \text{ mM}^{-1} \text{ s}^{-1}$ .

In summary, novel carrier systems composed of  $\gamma$ -Fe<sub>2</sub>O<sub>3</sub>-PEGPEI meet key quality requirements, rendering them promising for biomedical applications, e.g. as MRI contrast agents.

---

## INTRODUCTION

Magnetic iron oxide nanoparticles (IONP) have met with increasing interest due to potential biomedical applications, amongst others in drug delivery [1, 2], magnetic resonance imaging (MRI) [3, 4] and hyperthermia of tumors [5]. Recently, the design of such carrier systems has moved towards multifunctionality based on drug loaded IONP [6, 7] and more selectivity by the attachment of targeting ligands [8]. In all cases, biocompatibility of IONP regarding immunogenicity and colloidal stability is of concern.

In general, surface coatings are necessary which influence aggregation behavior, colloidal stability in blood, cytotoxicity, and furthermore play a significant role in pharmacokinetics and biodistribution in the body [9]. Stabilization strategies for magnetic iron oxide nanoparticles are mostly based on polymer coatings. Polymers investigated include crosslinked dextran, poly(lactic acid), poly(ethylene glycol), chitosan and polyvinyl alcohol [10]. Newer strategies concern amphiphilic polymers for phase transfer of IONP generated in organic solvents [11]. Also, cationic polymers such as poly(ethylene imine) (PEI) have been used to stabilize IONP by adsorptive coating on numerous occasions [12]. Such IONP have been investigated in the context of multifunctional carriers, allowing imaging and nucleic acid delivery [13, 14], but also for targeting and imaging purposes [15, 16].

Problems associated with PEI coated IONP are their lack of colloidal stability and cytotoxicity associated with the polymer. It has been demonstrated that such IONP tend to aggregate in certain cell culture media and in the presence of serum proteins [17]. A potential strategy to overcome these problems could be the modification of PEI backbone with poly(ethylene glycol) (PEG), as PEG provides copolymers with increased stability, increased circulatory lives and lower toxicity [18]. Only scant information is available on IONP stabilized by copolymers of PEG and PEI [19].

It was hypothesized that copolymers of the type poly(ethylene imine)-*g*-poly(ethylene glycol), PEGPEI could serve as coating agent for magnetic iron oxide nanoparticles, leading to enhanced colloidal stability and reduced cytotoxicity due to PEG shielding effects. To verify these assumptions,  $\gamma$ -Fe<sub>2</sub>O<sub>3</sub> nanoparticles were coated with PEGPEI, using a straightforward manufacturing technique. These IONP were compared with PEI coated nanoparticles to evaluate the effect of PEG shielding. IONP were characterized with respect to physicochemical properties and composition. Moreover, colloidal stability and aggregation behavior were investigated, as well as cytotoxicity and contrast enhancement in MRI experiments.

## **MATERIALS AND METHODS**

### **Materials**

Iron(II)chloride tetrahydrate and iron(III)chloride hexahydrate were purchased from Sigma Aldrich (Taufkirchen, Germany). Branched poly(ethylene imine) (PEI) with a molecular weight of 25,000 Da was a gift from BASF (Ludwigshafen, Germany). Block copolymers of the general composition PEI(25k)-*g*-PEG(20k)<sub>1</sub>, abbreviated as PEGPEI, were synthesized as previously described [20]. Synthesis procedures and dilution steps were carried out in ultra pure water (0.055  $\mu$ S/cm, USF Seral, Seradest BETA 25 and Serapur DELTA UV/UF) unless otherwise stated. All other chemicals were obtained from commercial sources, and used as received without further purification.

### **Preparation of $\gamma$ -Fe<sub>2</sub>O<sub>3</sub> nanoparticle cores**

Iron oxide nanoparticles were prepared by an aqueous coprecipitation route adapted from the Massart process [21]. Briefly, concentrated ammonia solution (25 %) was slowly added to a

---

0.13 M slightly acidic solution of iron(III) chloride hexahydrate and iron(II)chloride tetrahydrate (molar ratio 2:1) until formation of a dark black slurry occurred. After collection with a permanent magnet and triple washing with ultra pure water, particles were refluxed in a mixture of nitric acid and 0.34 M iron(III)nitrate nonahydrate at 90 °C for 30 minutes. The precipitate was collected by magnetic decantation and subsequently dispersed in water to yield a stable final suspension at pH 2.

Functionalized nanoparticles were generated by mixing the iron oxide suspensions with PEI or PEGPEI polymer solutions for 30 minutes at a defined mass ratio [Fe] to [PEI] of 1:2. Unbound polymer was removed by dialyzing the suspensions in multiple cycles against a 500-fold excess of ultra pure water, using Spectra/Por® membranes with MWCO 100,000 Da (Carl Roth, Karlsruhe, Germany).

### **Characterization of $\gamma$ -Fe<sub>2</sub>O<sub>3</sub> cores**

- **Transmission electron microscopy**

Size and morphology of  $\gamma$ -Fe<sub>2</sub>O<sub>3</sub> cores were investigated using transmission electron microscopy (TEM). Suspension droplets were placed onto carbon-coated copper grids S160-3 (Plano, Wetzlar, Germany) and allowed to air dry. After insertion into the microscope JEM-3010 (Jeol Germany, Eching, Germany), pictures were taken at an acceleration voltage of 300 kV. Core dimensions were calculated by averaging at least 200 particle diameters using ImageJ software.

- **X-ray diffraction**

X-ray diffraction (XRD) patterns of naked iron oxide cores were recorded on a Panalytical X'Pert Pro powder diffractometer (Almelo, Netherlands) to characterize the crystallite type and structure of the material. For that purpose, particle suspensions were lyophilized and

---

desiccated thoroughly before being screened with the goniometer at  $2\theta$  angles from  $20^\circ$  to  $80^\circ$  at a stepwidth of  $0.0131^\circ$ .

- **Magnetization measurements**

The dried samples were further investigated with regard to their expected superparamagnetic behavior. Small amounts of material were introduced into a Magnetic Property Measurement System MPMS® equipped with 5 T magnet (Quantum Design, San Diego, CA), using superconducting quantum interference device (SQUID) technology. Samples underwent a zero field-cooled field-cooled (zfc-fc) sweep from 5 to 350 K at a rate of 2 K/min and an external magnetic field strength of 50 and 500 Oe, respectively.

### **Characterization of polymer-coated nanoparticles**

- **Dynamic light scattering**

Hydrodynamic diameters of nanoparticles after polymer functionalization were assessed by dynamic light scattering (DLS) on a Zetasizer Nano ZS (Malvern Instruments, Herrenberg, Germany). Measurements were performed at  $25^\circ\text{C}$  after appropriate dilution of the respective samples with ultra pure water to avoid multiscattering events. DTS v. 5.10-software was used to calculate both particle mean diameters from intensity-weighted distributions (Z-Ave) and distribution widths displayed as the polydispersity index (PDI).

- **Thermal gravimetric analysis and FT-IR spectroscopy**

Investigations on the general and quantitative composition of polymer-coated iron oxide nanoparticles were carried out via thermal gravimetric analysis (TGA) and infrared spectroscopy (IR). In the course of the thermal analysis, lyophilized samples of iron oxide, pure PEI or PEGPEI and core-shell compounds thereof were tracked over a temperature range from  $25$  to  $900^\circ\text{C}$  at a scan rate of 20 K/min under nitrogen atmosphere using a PerkinElmer

---

TGA 7 assembly (Rodgau, Germany). Samples of similar type were also subjected to infrared wavenumber scans between 4000 and 400  $\text{cm}^{-1}$  on a Bruker FT-IR spectrometer with Alpha Platinum ATR sampling module (Bruker Optics, Ettlingen, Germany).

### **Colloidal stability**

The stability of the polymer-coated formulations was tested in a dual set of experiments. Firstly, change of particle diffusivity in different relevant media was examined over a time scale of 30 minutes. Here, 10  $\mu\text{L}$  of nanoparticle suspensions containing iron concentrations of 1  $\text{mg/mL}$  were diluted 40-fold with one of the following agents: ultra pure water, sodium chloride 0.9 % (w/v), fetal calf serum (FCS) of different concentrations or Dulbecco's Modified Eagle Medium (DMEM) high glucose supplemented with 10 % FCS and L-glutamine. Trends of diffusion coefficients over the half-hour period were read out by dynamic light scattering on a Zetasizer Nano ZS at 25  $^{\circ}\text{C}$  with settings analogous to the section stated above for size measurements.

Secondly, the same formulations were analyzed at 37  $^{\circ}\text{C}$  for alterations in turbidity at 630 nm over 12 hours with an Ultrospec 3000 spectrophotometer (Pharmacia Biotech, Vienna, Austria). Suspensions were mixed with the abovementioned solutions in a 1:40 ratio, and transmissions were recorded at given times. Samples were stored in a thermal block at 37  $^{\circ}\text{C}$  throughout the whole experiment, and redispersed prior to each measurement by vortexing.

### **Cell culture and trypan blue exclusion assay**

Human lung adenocarcinoma cell line A549 was maintained in DMEM high glucose containing 10 % FCS and L-glutamine without the addition of antibiotics in a humidified atmosphere at 37  $^{\circ}\text{C}$  and 8.5 %  $\text{CO}_2$ . For the experiment, cells were seeded onto 24-well plates at a density of 60,000 per well. After awaiting adherent growth, culture medium was exchanged with DMEM supplemented with 5 % FCS, in order to avoid interference with the

---

assay reagents. Immediately thereafter, the wells were incubated with increasing [Fe] concentrations of either iron oxide-PEI or iron oxide-PEGPEI for a period of 24 hours. For the purpose of comparison, treatment with pure PEI was performed, due to its well-known cytotoxic properties. Unmanipulated wells served as a control. After 24 hours, cells were washed twice with PBS to remove aggregated material, and 20  $\mu$ L of 0.4 % trypan blue were added by pipet. Three minutes after addition of the dye, magnified pictures of the respective wells were taken on a camera-equipped microscope. The percentage of cell viability was determined by inspecting at least 200 cells for lack or presence of intracellular blue color, as dead cells soak up the dye due to loss of membrane integrity.

### **MR relaxometry**

Magnetic resonance imaging studies were carried out on a 7 T Bruker ClinScan 70/30 USR (Bruker BioSpin, Rheinstetten, Germany). Concentration series of polymer-functionalized iron oxide nanoparticles were placed into microcentrifuge cups to avoid artifacts from surrounding air. For measurements of transverse  $T_2$  relaxation times, spin-echo multicontrast sequences were run at  $T_R$  values of 2000 ms, varying spin echo times  $T_E$  (10-150 ms with an increment of 10 ms), field of view 65x75 mm, matrix 112x128 and slice thickness 0.6 mm. Data quantification was achieved by evaluating DICOM images.  $T_2$  maps were generated from the overlay of successive spin-echo images, using a nonlinear monoexponential fitting of the signal intensity ( $SI$ ) decay curve:  $SI(t) = S_0 \exp(-t/T_2)$ , where  $S_0$  is the signal magnitude at equilibrium and  $t$  the particular echo time. Relaxation times  $T_2$  and their reciprocal values, relaxation rates  $R_2 (=1/T_2)$  could therefore be derived by analyzing regions of interest (ROI) within the created maps.

Additionally, effective transverse relaxation times ( $T_2^*$ ) were calculated from  $T_2^*$ -weighted images taken with the following settings: gradient-echo multicontrast with  $T_R$  350 ms, multiple spin echo times  $T_E$  (2-5 ms), field of view 58x78 mm, matrix 96x128, slice thickness



---

0.5 mm.  $T_2^*$  values were obtained correspondingly by plotting the MRI signal intensities of the acquired maps versus echo times  $T_E$ .

### **Statistical analysis**

Measurements were carried out in triplicate and data are presented as mean  $\pm$  S.D. unless otherwise noted. For statistical testing, one-way ANOVA in conjunction with Bonferroni's post- $t$  test analysis were performed. Probability values of  $p < 0.05$  were considered significant.

## **RESULTS AND DISCUSSION**

### **Particle synthesis**

Iron oxide nanoparticles prepared by the aqueous precipitation route suggested are generally of the maghemite ( $\gamma\text{-Fe}_2\text{O}_3$ ) type, after mild oxidation of the intermediate modification magnetite ( $\text{Fe}_3\text{O}_4$ ). Initial stabilization was conferred to the naked  $\gamma\text{-Fe}_2\text{O}_3$  nanoparticles by electrostatic repulsion following peptization in acidic environment. Ammonia solution was added dropwise to the reaction mixture to induce a short burst of nucleation and controlled growth of IONP. Both parameters have been described to be essential for size uniformity, according to the LaMer diagram [22]. Other factors determining particle size, such as type, molarity and ratio of iron salts, were kept constant throughout the whole manufacturing process. Mixing of iron oxide suspensions with polymer solutions yielded the formulations of interest,  $\gamma\text{-Fe}_2\text{O}_3\text{-PEI}$  and  $\gamma\text{-Fe}_2\text{O}_3\text{-PEGPEI}$ . The simplicity and lack of organic solvents generally render this coating procedure favorable for biological applications.

## Physicochemical characterization

- **Size and morphology of  $\gamma$ -Fe<sub>2</sub>O<sub>3</sub> cores**

The maghemite cores depicted on TEM pictures (*Figure 1*) were found to be irregularly shaped with an average diameter of  $10.8 \pm 3.0$  nm, and arranged in clusters, because of their magnetic nature. Size values were obtained by averaging 200 core diameters, representing a number-weighted distribution pattern. Dynamic light scattering experiments showed considerably larger diameters, due to the inclusion of regions of agglomeration and the analysis in intensity-weighted mode (data not shown). Transmission electron micrographs revealed uniformly arranged planes inside the  $\gamma$ -Fe<sub>2</sub>O<sub>3</sub> crystallite at very high magnifications. Relatively wide size distribution and poor control of the shape of IONP are drawbacks generally observed with the aqueous coprecipitation route [23]. Distribution width, however, is still in an acceptable range and the avoidance of organic solvents turns out to be beneficial for biomedical use. The high resolution images suggest an inverse spinel structure of the maghemite crystal lattice.

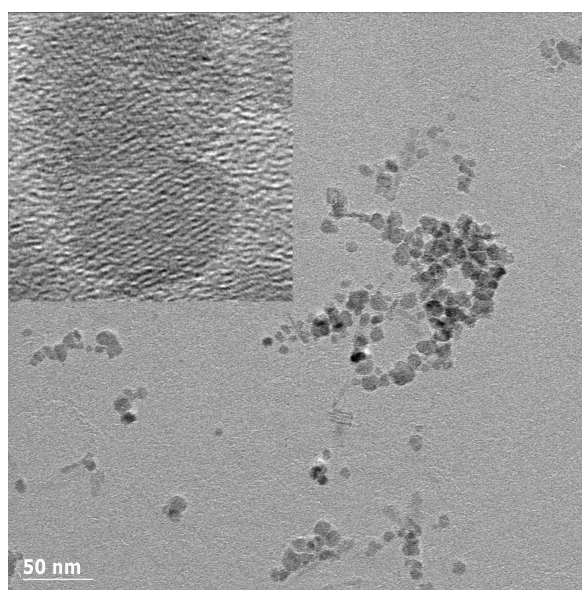


*Figure 1. Transmission electron micrographs on morphology of synthesized  $\gamma$ -Fe<sub>2</sub>O<sub>3</sub> cores and crystallite structure at higher magnification (inset).*

- **Crystal modification of synthesized iron oxide**

Evidence of identity and crystal structure were further verified by X-ray diffraction patterns. Intensity signals appeared at defined scattering angles  $2\theta$  with the most prominent ones at  $30.6^\circ$ ,  $35.9^\circ$ ,  $43.3^\circ$ ,  $57.4^\circ$  and  $63.2^\circ$  (Figure 2). The Bragg peaks could be assigned to specific diffraction planes inside the maghemite lattice: (2 2 0), (3 1 1), (4 0 0), (5 1 1) and (4 4 0). The assembly of the diffraction peaks is indicative of a cubic inverse spinel structure and conforms to maghemite/magnetite reference spectra due to the relative positions of signals [24].

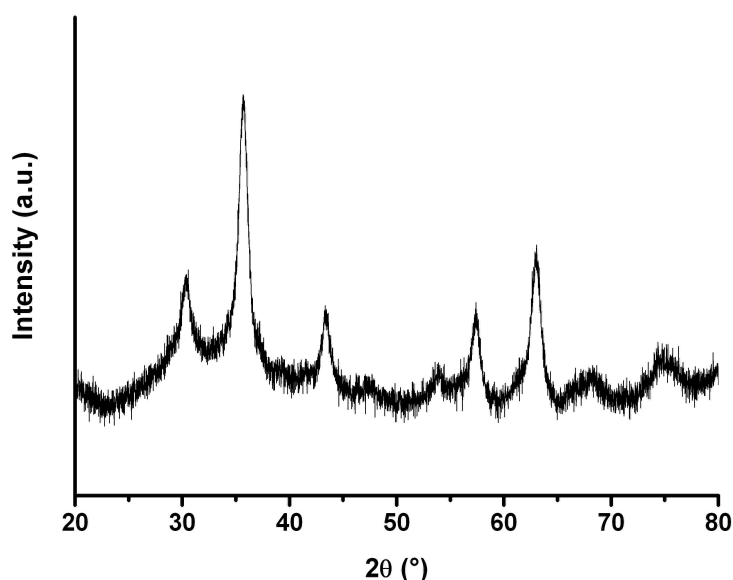


Figure 2. XRD pattern of prepared iron oxide ( $\gamma\text{-Fe}_2\text{O}_3$ ) nanoparticles, indicative of inverse spinel structure. Signals are assignable to diffraction planes (2 2 0), (3 1 1), (4 0 0), (5 1 1) and (4 4 0) at  $30.6^\circ$ ,  $35.9^\circ$ ,  $43.3^\circ$ ,  $57.4^\circ$  and  $63.2^\circ$ , respectively.

In general, appearance of signals is regulated by the incident X-ray wavelength ( $K_{\alpha 1}$ : 1.5406 nm,  $K_{\alpha 2}$ : 1.5444 nm). Distinguishability between the modifications  $\gamma\text{-Fe}_2\text{O}_3$  and  $\text{Fe}_3\text{O}_4$  is not possible due to the crystallographically isomorphous structures of both materials. Broadening of the peaks is caused by crystallite size and, to a lesser extent, lattice strain [25]. Crystallite

diameters were accessible by application of the Scherrer equation, which considers size contributions to peak broadening [26]. The formula is given by

$$B = \frac{K \lambda}{L \cos \theta}$$

where  $B$  is the half-value width of respective Bragg peaks,  $\lambda$  the applied X-ray wavelength,  $L$  the diameter,  $\theta$  the Bragg angle and  $K$  the shape-dependent Scherrer constant (set to 0.9). The calculated mean diameters of  $10.3 \pm 1.2$  nm supported findings from transmission electron microscopy. The slight discrepancies between both methods can be explained by the existence of thin amorphous layers on the surface of the iron oxide nanoparticles, and the already mentioned lattice strain.

- **Superparamagnetism**

Temperature-dependent magnetization measurements for naked iron oxide nanoparticles indicated the presence of a blocking temperature  $T_B$  of 75 K, visible in the zero field-cooled section, at an external field strength of 50 Oe (*Figure 3*). Also, the rather broad distribution around the  $T_B$  maximum was clearly noticeable. Moreover, the blocking temperature shifted to lower values at 500 Oe and vanished completely at higher magnetic field strengths (data not shown). The appearance of  $T_B$  is an indicator for the superparamagnetic behavior of the types of iron oxide prepared. Nanoscale magnetic particles possess a so-called blocking temperature as thermal limit that divides blocked and superparamagnetic state [27]. Above this value, thermal energy exceeds anisotropy energy and leads to randomization of magnetic moments much faster than the experimental time scales. As seen here, the thermal energy input upon heating of the samples disturbs the systems, initially leading to unblocking and alignment of magnetic moments with the external magnetic field. Thereafter, iron oxide nanoparticles drift into the superparamagnetic state characterized by randomization of magnetic vectors and decrease of magnetization. It can thus be concluded that the IONP are

combining strong magnetic moments and paramagnetic behavior (superparamagnetism), which is of great importance for biomedical applications.

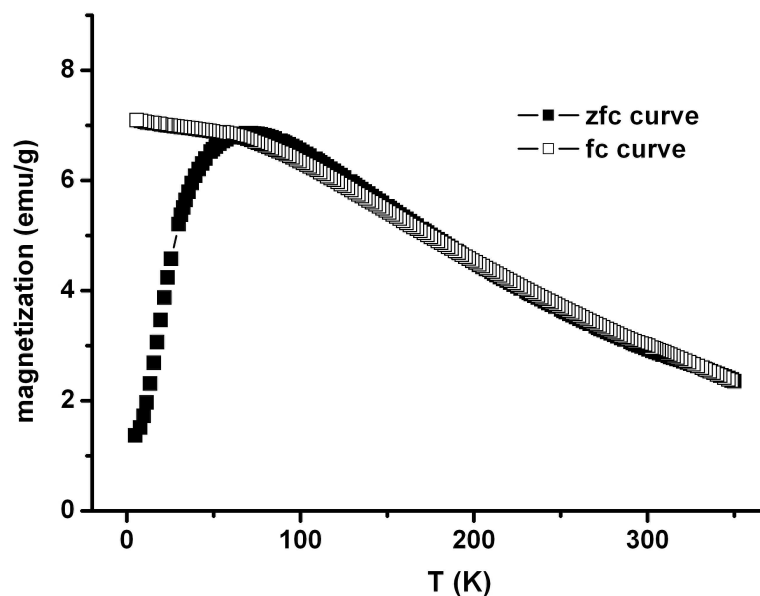


Figure 3. Temperature-dependent magnetization of  $\gamma\text{-Fe}_2\text{O}_3$  nanoparticles, as obtained from zero field-cooled – field-cooled (zfc-fc) sweep at an external field strength of 50 Oe. Superparamagnetic limit is given by the maximum of the zfc curve, namely the blocking temperature  $T_B$ .

- **Hydrodynamic diameters of polymer-coated nanoparticles**

All further physicochemical investigations were performed on the coated nanoparticle formulations after adsorptive layering with polymers. Particle sizes, as measured by dynamic light scattering, were found to be  $38.7 \pm 1.0$  nm ( $\gamma\text{-Fe}_2\text{O}_3\text{-PEI}$ ) and  $40.4 \pm 1.6$  nm ( $\gamma\text{-Fe}_2\text{O}_3\text{-PEGPEI}$ ), suggesting an increase in radii of 13-15 nm under the assumption that single iron oxide cores were layered with the respective polymers (Table 1). Polymer layer thickness is thus similar for both formulations, despite PEGPEI displaying almost double molecular

weight. The polydispersity indices (PDI) representing the widths of the fitted Gaussian distributions amounted to  $0.212 \pm 0.013$  and  $0.186 \pm 0.018$ , respectively.

	size (nm)	$r_2$ ( $\text{mM}^{-1} \text{s}^{-1}$ )	$r_2^*$ ( $\text{mM}^{-1} \text{s}^{-1}$ )
$\gamma\text{-Fe}_2\text{O}_3$	$10.8 \pm 3.0$ *		
$\gamma\text{-Fe}_2\text{O}_3\text{-PEI}$	$38.7 \pm 1.0$ **	163.2	249.1
$\gamma\text{-Fe}_2\text{O}_3\text{-PEGPEI}$	$40.4 \pm 1.6$ **	155.7	231.7

\* as measured by TEM

\*\* as measured by DLS (n = 3)

*Table 1. Physicochemical parameters of magnetic iron oxide nanoparticles.*

As a result, these IONP had particle sizes smaller than those of the commercially available product Resovist® (60 nm) and may be designated as ultrasmall superparamagnetic iron oxide nanoparticles (USPIO). It has been shown earlier that poly(ethylene imine) can attach to very different surfaces within a broad pH range [28]. We assume that the binding mechanism of PEI onto maghemite is a combination of hydrogen bonding and dipolar interactions. The slight difference in polymer layer thickness referred to, suggests in our opinion the orientation of PEG molecules along the nanoparticle surface, thereby forming a protective shield in aqueous environment. Besides that, we observed an auto-regulation of the pH values after mixing iron oxide and polymer suspensions to numbers of 7.5 to 7.7, presumably evoked by the buffering capacity of the branched poly(ethylene imine) and its derivative PEGPEI. This enables an euhydric application of the formulation without further manipulations. So, despite its simplicity, this synthesis strategy permits the fabrication of small nanoparticulate carriers with relatively narrow size distributions at neutral pH. However, the colloidal stability of these adsorptive compounds remains to be addressed.

- **Composition of polymer-coated nanoparticles**

In additional experiments, the relative composition of the hybrid particles, consisting of an inorganic iron oxide core and an organic polymer shell, was assessed by thermal analysis and IR spectrometry. Thermograms revealed a degradation onset for pure PEI at 370 °C and a biphasic degradation process for PEGPEI. The curves for the hybrid nanoparticles showed analogous patterns and remainder of the inorganic iron oxide cores at high temperatures (*Figures 4a and b*). Due to apparent minimum water residues in the samples, an absolute quantification of polymer contribution to the overall particle mass was difficult, but estimated to be 55 % in the case of PEI and 65 % for PEGPEI. The degradation temperature values obtained were in good accordance with results from earlier studies [29]. Furthermore, it became obvious that almost all polymer applied during the layering process of maghemite nanoparticles is bound to the surface (maximum mass fraction PEI 59 % and PEGPEI 72 %). Only a small percentage got washed out during dialysis purification of the batches.

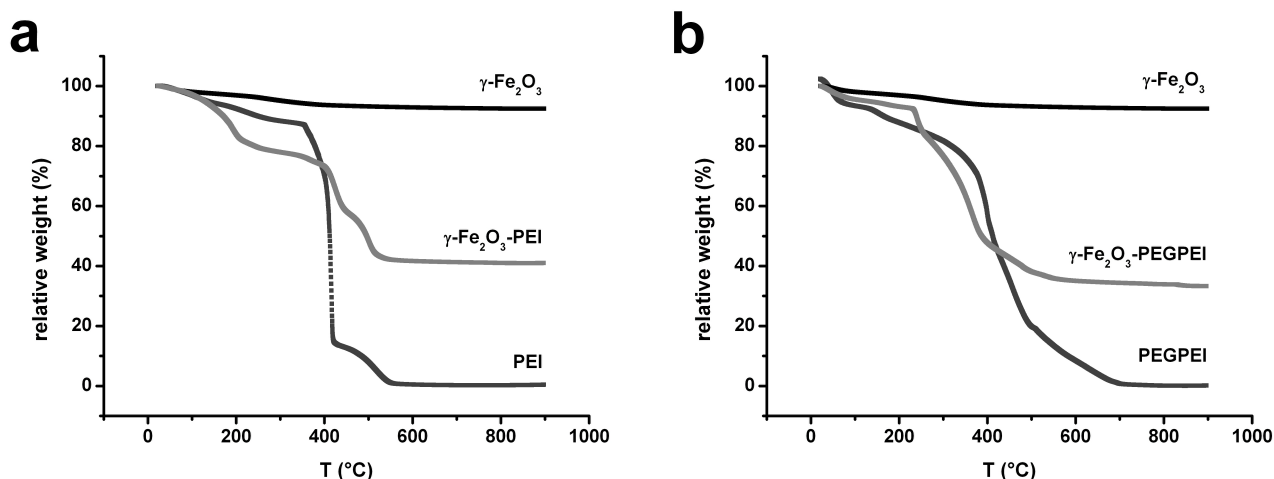


*Figure 4. Relative weight loss of hybrid nanoparticle systems (a)  $\gamma\text{-Fe}_2\text{O}_3$ -PEI and (b)  $\gamma\text{-Fe}_2\text{O}_3$ -PEGPEI upon heating to 900 °C (TGA). Respective curves for naked  $\gamma\text{-Fe}_2\text{O}_3$  cores and pure polymers were taken for comparison reasons.*

Further evidence for the qualitative assembly of the hybrid nanoparticles was gained by infrared spectra, for clarity only data for the  $\gamma$ -Fe<sub>2</sub>O<sub>3</sub>-PEI type are shown. Vibration signals originating from the Fe-O bond were found at wavenumbers of 630, 585 and 440 cm<sup>-1</sup> and coexisted for both pure maghemite and  $\gamma$ -Fe<sub>2</sub>O<sub>3</sub>-PEI nanoparticles (*Figure 5*).

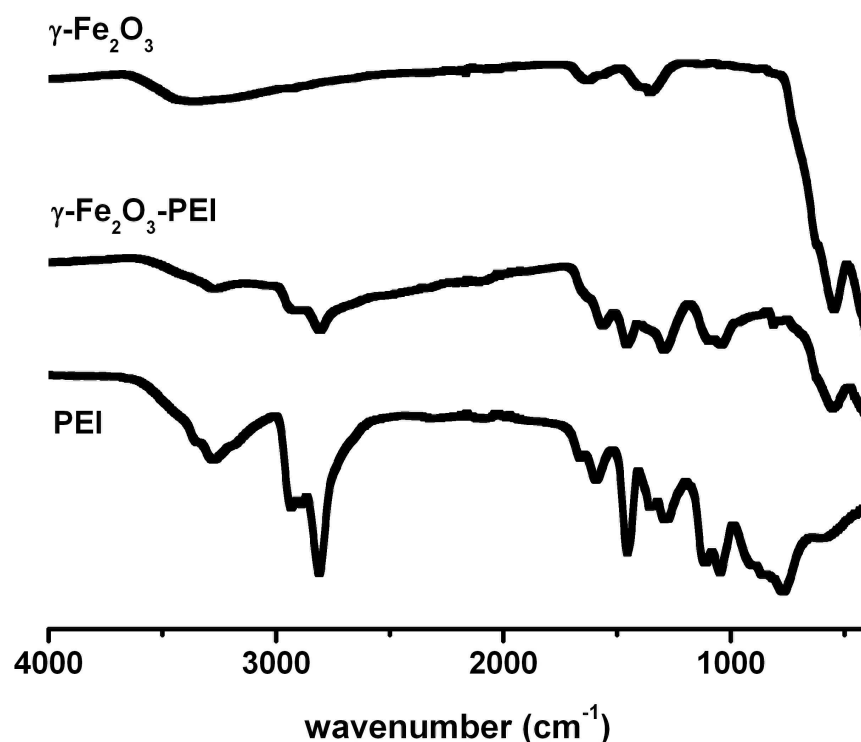


*Figure 5. Infrared wavenumber scans for lyophilized  $\gamma$ -Fe<sub>2</sub>O<sub>3</sub>-PEI and its singular components. Spectra were arranged on top of each other for clarity.*

Moreover, characteristic bands for poly(ethylene imine), such as the N-H stretch at 3500-3300 cm<sup>-1</sup>, were recorded and coincided with those of hybrid particles. Others reported that finite-size effects in nanoparticulate maghemite cause splitting of the Fe-O  $\nu_1$  band to values above 570 cm<sup>-1</sup> and shifting of the  $\nu_2$  band (375 cm<sup>-1</sup>) to higher wavenumbers [30].



---

### Colloidal stability in different media

Diffusion coefficients of formulations  $\gamma$ -Fe<sub>2</sub>O<sub>3</sub>-PEI and  $\gamma$ -Fe<sub>2</sub>O<sub>3</sub>-PEGPEI in various media, as calculated from the DLS auto-correlation function, were recorded to identify alterations in overall particle size. The changes were most pronounced for  $\gamma$ -Fe<sub>2</sub>O<sub>3</sub>-PEI in supplemented cell medium DMEM with a 65 % decrease of diffusion coefficients after 30 minutes, while dispersion of both formulations in saline or fetal calf serum left the particle diffusivity rather unchanged, with a minor exception for very high protein levels in FCS 90 % (*Figures 6a and b*). Turbidity measurements over 12 h generally confirmed these findings, as the decay of transmission indicating aggregation of nanoparticles was found to be most distinct for  $\gamma$ -Fe<sub>2</sub>O<sub>3</sub>-PEI in DMEM 10 % FCS (*Figures 6c and d*), also macroscopically observable by a complete loss of transparency.

The results suggest that adsorption of serum components did not induce detrimental effects on stability of polymer-coated iron oxide nanoparticle systems, as seen by the constancy of relative diffusion coefficients. However, absolute sizes after protein adsorption were found to be slightly enhanced for the  $\gamma$ -Fe<sub>2</sub>O<sub>3</sub>-PEI type, hinting at facilitated and increased attachment of the protein fraction. When additionally introduced into a high ionic strength environment like DMEM, these carriers begin to precipitate massively, presumably due to shrinkage of the electrical double layers and loss of repulsive shielding between the particles. The improved performance of  $\gamma$ -Fe<sub>2</sub>O<sub>3</sub>-PEGPEI (in DMEM 10 % FCS) is assumed to be caused by an effective reduction in absolute protein adsorption levels, thus retaining individuality of the nanoparticles, and may be attributed in large part to the presence of surface PEG moieties. PEG coatings have been shown to prevent protein fouling and to provide steric hindrance suppressing aggregation [31]. As cell medium DMEM 10 % FCS has a similar ionic composition to simulated body fluid and equals human blood serum assembly, results are promising for a possible *in vivo* application of PEGPEI-modified nanoparticles. On the one hand, these particles can evade rapid sequestration in MPS organs due to their small size and

stability [32], on the other hand iron oxide pegylation offers possibly the beneficial effect of reduced protein opsonization *in vivo*. Through the synergistic combination of these mechanisms, the blood circulation half-lives of the carriers are supposed to be greatly enhanced, and hence the access to deeper compartments is facilitated [33].

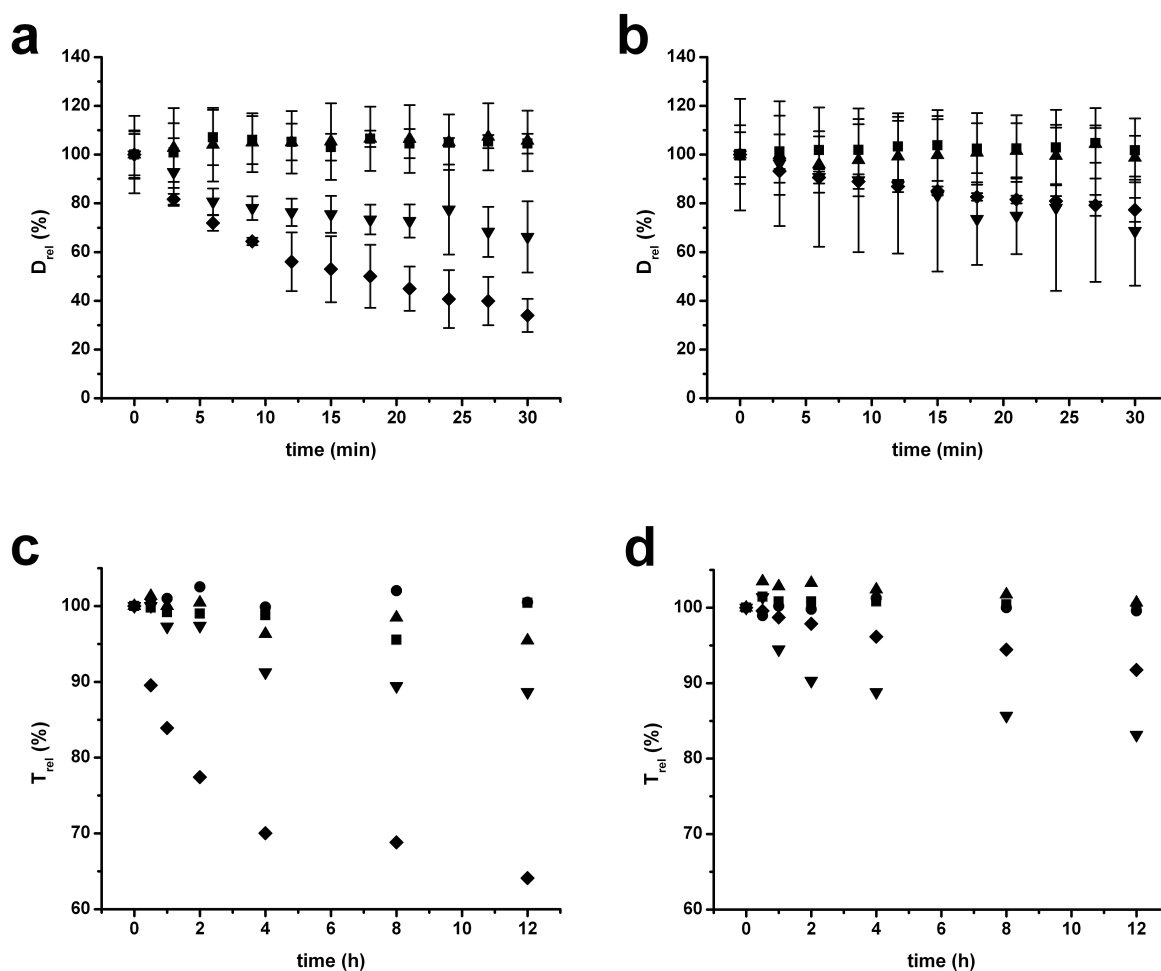


Figure 6. Colloidal stability of nanoparticle formulations in NaCl 0.9 % (■), FCS 10 % (▲), FCS 90 % (▼) and DMEM supplemented with 10 % FCS (◆), as measured by changes of relative diffusion coefficients  $D_{rel}$  and relative transmissions  $T_{rel}$  over time. Initial values were set to 100 %. Course of  $D_{rel}$  was monitored for (a)  $\gamma\text{-Fe}_2\text{O}_3\text{-PEI}$  and (b)  $\gamma\text{-Fe}_2\text{O}_3\text{-PEGPEI}$  nanoparticles ( $n = 3$ ) in the different media. Graphs (c) and (d) show transmission data at 630 nm for  $\gamma\text{-Fe}_2\text{O}_3\text{-PEI}$  and  $\gamma\text{-Fe}_2\text{O}_3\text{-PEGPEI}$ , respectively.

### Cytotoxicity assessment

A549 cell viability profiles after incubation with nanoparticulate [Fe] amounts of 0.1-100  $\mu\text{g/mL}$  were sigmoidally fitted and yielded  $\text{IC}_{50}$  values of 6.8 and 160  $\mu\text{g/mL}$  [Fe] for  $\gamma\text{-Fe}_2\text{O}_3\text{-PEI}$  and  $\gamma\text{-Fe}_2\text{O}_3\text{-PEGPEI}$ , respectively (data not shown). Due to the fact that cytotoxicity of hybrid iron oxide nanoparticles in the applied concentration range is caused to a major extent by their polymeric coatings [34], incubation concentrations were recalculated and standardized to polymer molarities of either PEI or PEGPEI, and viability curves were replotted for comparison purposes (Figure 7). For example, the incubation amount of 10  $\mu\text{g/mL}$  [Fe] equals 14.3  $\mu\text{g/mL}$  of  $\gamma\text{-Fe}_2\text{O}_3$  and, given the findings from TGA analysis, where hybrid  $\gamma\text{-Fe}_2\text{O}_3\text{-PEI}$  nanoparticles were found to contain 60 % of polymer, subsequently 21.5  $\mu\text{g/mL}$  or 0.86  $\mu\text{M}$  of PEI. Thereafter, it could be seen clearly that poly(ethylene imine) layered on iron oxide particles exhibited cytotoxicity comparable to free PEI polymer, while PEGPEI created these effects only when applied at an almost 20-fold amount.

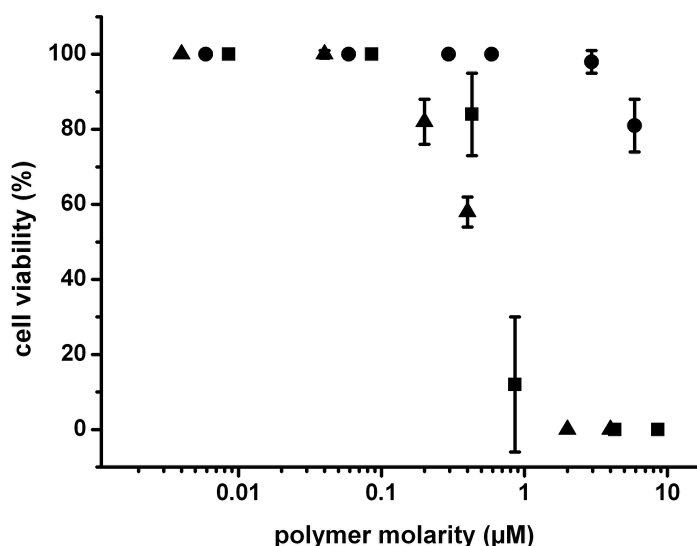


Figure 7. A549 cell viability, as observed by trypan blue exclusion assay after incubation with dilutions of PEI 25k ( $\blacktriangle$ ),  $\gamma\text{-Fe}_2\text{O}_3\text{-PEI}$  ( $\blacksquare$ ) and  $\gamma\text{-Fe}_2\text{O}_3\text{-PEGPEI}$  ( $\bullet$ ). Values are plotted against polymer fractions of each formulation.  $\text{IC}_{50}$  numbers were accessible by sigmoidal fitting of the curves.

Despite the implemented approximation, the informative value of the chosen display is in our opinion higher than for standard depictions plotting viability versus iron concentration. The highly destructive nature of poly(ethylene imine) originates from its strong cationic character, which is responsible for inducing defects into lipid bilayers [35]. Shielding of cytotoxicity has been reported to be brought about by covalent attachment of poly(ethylene glycol) to harmful polymers like PEI. However, the massive reduction in cytotoxicity seen here outcores findings for PEI(25k)-g-PEG(20k)<sub>1</sub> polyplexes, where decrease in cell-detrimental effects upon pegylation was not that pronounced [36]. Also, modification of PEI 25 kDa was shown to reduce cytotoxic and oxidative stress most effectively at high degrees of PEGylation and low PEG chain lengths [37]. We explain the different behavior by the fact that PEG moieties on the surface of iron oxide nanoparticles are mainly directed towards the surrounding medium, thereby efficiently contributing to the shielding of these systems, whereas polyplexes hide large parts thereof on the inside. Fetal calf serum concentration was reduced to 5 % prior to incubation experiments in order to minimize masking effects by proteins [38].

### **Potential of IONP as MRI contrast agent**

Relaxivities  $r_2$  and  $r_2^*$  were accessible by measuring relaxation times for concentration series of the formulations  $\gamma\text{-Fe}_2\text{O}_3\text{-PEI}$  and  $\gamma\text{-Fe}_2\text{O}_3\text{-PEGPEI}$  via the general equation

$$1 / T_2^{(*)} = 1 / T_{init.} + r_2^{(*)} C$$

where  $T_{init.}$  represents the initial relaxation time, and  $T_2$  or  $T_2^*$  are the relaxation times determined for [Fe] concentrations  $C$ . Experimental values for  $r_2$  at a magnetic field strength of 7 T ran up to 163.2 and 155.7  $\text{mM}^{-1} \text{s}^{-1}$  for  $\gamma\text{-Fe}_2\text{O}_3\text{-PEI}$  and  $\gamma\text{-Fe}_2\text{O}_3\text{-PEGPEI}$ , respectively (*Table 1*). Gradient-echo  $T_2^*$  images of linearly arranged concentration series of  $\gamma\text{-Fe}_2\text{O}_3\text{-PEI}$  suspensions revealed loss of signal decay with decreasing iron concentrations, visible by transient brightening of the respective microcentrifuge tubes (*Figure 8*). This phenomenon is

caused by the significant enhancement of transverse proton relaxation in the vicinity of areas containing magnetic iron oxide, thus leading to quick fading of MR signals.

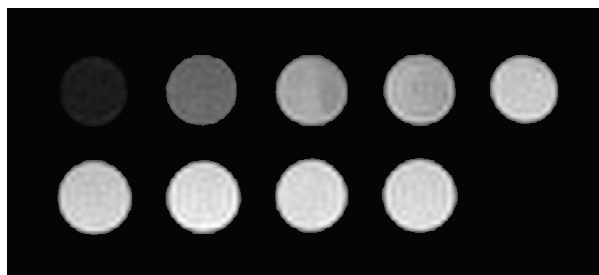


*Figure 8.  $T_2^*$ -weighted image of  $\gamma\text{-Fe}_2\text{O}_3\text{-PEI}$  nanoparticle suspensions with  $[\text{Fe}]$  concentrations of 100, 50, 30, 20, 10, 5, 2, 1 and 0.1  $\mu\text{g/mL}$  (top left to bottom right).*

As the coating thickness negatively affects the performance of magnetic nanoparticles, the slightly higher  $r_2$  and  $r_2^*$  values for  $\gamma\text{-Fe}_2\text{O}_3\text{-PEI}$  particles can be attributed to their lower polymer fraction. However, the calculated  $r_2$  relaxivities are a measure for the efficiency of contrast agents and were found to be superior to most marketed products [39]. Taken together, the results prove the possibility of applying the formulations as MR contrast agents, e.g. for cell tracking, where accelerated uptake behavior mediated by positive surface charges would increase the degree of cellular labeling.

## CONCLUSIONS

An interesting alternative to current polymer candidates for coating of iron oxide nanoparticles was suggested to be poly(ethylene imine)-*g*-poly(ethylene glycol) (PEGPEI), representing in our opinion an advancement of pure poly(ethylene imine) in terms of colloidal stability and cytotoxicity, due to introduced PEG shielding moieties. We generated a novel magnetic carrier system based on the assembly of PEGPEI and iron oxide nanoparticles,

---

which meets the premium requirements for biomedical applications, amongst these small size, narrow size distribution and superparamagnetism. Despite the simplicity of the synthesis procedure,  $\gamma$ -Fe<sub>2</sub>O<sub>3</sub>-PEGPEI particle systems displayed good colloidal stability over long-term range when suspended in critical cell media. Moreover, particle-associated toxicity was significantly reduced in contrast to correspondents  $\gamma$ -Fe<sub>2</sub>O<sub>3</sub>-PEI due to introduction of hydrophilic PEG groups to the polymer backbone. Relaxometric data underlined the general ability to enhance contrast in magnetic resonance imaging. The findings confirm the stated assumptions of increased stability and reduced cytotoxicity after nanoparticle coating with PEGPEI. Given these results, iron oxide-PEGPEI nanoparticles possess great potential for biomedical applications. Especially the use of these carriers for cell tracking purposes is envisioned, where sufficient intracellular accumulation and concurrent absence of toxicity are needed. These effects are supposed to be balanced well for  $\gamma$ -Fe<sub>2</sub>O<sub>3</sub>-PEGPEI, but need to be investigated in further studies.

#### **ACKNOWLEDGEMENTS**

The authors thank Maximilian Voelker from the Department of Diagnostic Radiology, Marburg, Germany for assistance with MR measurements and Eva Mohr for support in cell culture questions.

---

**REFERENCES**

- [1] Cengelli, F., Grzyb, J.A., Montoro, A., Hofmann, H., Hanessian, S., Juillerat-Jeanneret, L., 2009. Surface-Functionalized Ultrasmall Superparamagnetic Nanoparticles as Magnetic Delivery Vectors for Camptothecin. *ChemMedChem* 4, 988-997.
- [2] Chen, B., Lai, B., Cheng, J., Xia, G., Gao, F., Xu, W., Ding, J., Gao, C., Sun, X., Xu, C., Chen, W., Chen, N., Liu, L., Li, X., Wang, X., 2009. Daunorubicin-loaded magnetic nanoparticles of Fe<sub>3</sub>O<sub>4</sub> overcome multidrug resistance and induce apoptosis of K562-n/VCR cells in vivo. *Int. J. Nanomed.* 4, 201-208.
- [3] Howes, P., Green, M., Bowers, A., Parker, D., Varma, G., Kallumadil, M., Hughes, M., Warley, A., Brain, A., Botnar, R., 2010. Magnetic Conjugated Polymer Nanoparticles as Bimodal Imaging Agents. *J. Am. Chem. Soc.* 132, 9833-9842.
- [4] Li Calzi, S., Kent, D.L., Chang, K.-H., Padgett, K.R., Afzal, A., Chandra, S.B., Caballero, S., English, D., Garlington, W., Hiscott, P.S., Sheridan, C.M., Grant, M.B., Forder, J.R., 2009. Labeling of stem cells with monocrystalline iron oxide for tracking and localization by magnetic resonance imaging. *Microvasc. Res.* 78, 132-139.
- [5] Balivada, S., Rachakatla, R.S., Wang, H., Samarakoon, T.N., Dani, R.K., Pyle, M., Kroh, F.O., Walker, B., Leaym, X., Koper, O.B., Tamura, M., Chikan, V., Bossmann, S.H., Troyer, D.L., 2010. A/C magnetic hyperthermia of melanoma mediated by iron(0)/iron oxide core/shell magnetic nanoparticles: a mouse study. *BMC Cancer* 10, 119-127.

- 
- [6] Maeng, J.H., Lee, D.-H., Jung, K.H., Bae, Y.-H., Park, I.-S., Jeong, S., Jeon, Y.-S., Shim, C.-K., Kim, W., Kim, J., Lee, J., Lee, Y.-M., Kim, J.-H., Kim, W.-H., Hong, S.-S., 2010. Multifunctional doxorubicin loaded superparamagnetic iron oxide nanoparticles for chemotherapy and magnetic resonance imaging in liver cancer. *Biomaterials* 31, 4995-5006.
- [7] Santra, S., Kaittanis, C., Grimm, J., Perez, J.M., 2009. Drug/Dye-Loaded, Multifunctional Iron Oxide Nanoparticles for Combined Targeted Cancer Therapy and Dual Optical/Magnetic Resonance Imaging. *Small* 5, 1862-1868.
- [8] Lee, C.-M., Jeong, H.-J., Cheong, S.-J., Kim, E.-M., Kim, D.W., Lim, S.T., Sohn, M.-H., 2010. Prostate Cancer-Targeted Imaging Using Magnetofluorescent Polymeric Nanoparticles Functionalized with Bombesin. *Pharm. Res.* 27, 712-721.
- [9] Gupta, A.K., Gupta, M., 2005. Synthesis and surface engineering of iron oxide nanoparticles for biomedical applications. *Biomaterials* 26, 3995-4021.
- [10] Laurent, S., Forge, D., Port, M., Roch, A., Robic, C., Vander Elst, L., Muller Robert, N., 2008. Magnetic iron oxide nanoparticles: synthesis, stabilization, vectorization, physicochemical characterizations, and biological applications. *Chem Rev* 108, 2064-2110.
- [11] Kim, M., Jung, J., Lee, J., Na, K., Park, S., Hyun, J., 2010. Amphiphilic comblike polymers enhance the colloidal stability of Fe<sub>3</sub>O<sub>4</sub> nanoparticles. *Colloids Surf., B* 76, 236-240.



- 
- [12] Thuenemann, A.F., Schuett, D., Kaufner, L., Pison, U., Moehwald, H., 2006. Maghemite Nanoparticles Protectively Coated with Poly(ethylene imine) and Poly(ethylene oxide)-block-poly(glutamic acid). *Langmuir* 22, 2351-2357.
- [13] Huth, S., Lausier, J., Gersting Soeren, W., Rudolph, C., Plank, C., Welsch, U., Rosenecker, J., 2004. Insights into the mechanism of magnetofection using PEI-based magnetofectins for gene transfer. *J Gene Med* 6, 923-936.
- [14] Arsianti, M., Lim, M., Marquis, C.P., Amal, R., 2010. Assembly of Polyethylenimine Based Magnetic Iron Oxide Vectors: Insights into Gene Delivery. *Langmuir* 26, 7314-7326.
- [15] Chertok, B., David, A.E., Yang, V.C., 2010. Polyethyleneimine-modified iron oxide nanoparticles for brain tumor drug delivery using magnetic targeting and intra-carotid administration. *Biomaterials* 31, 6317-6324.
- [16] Masotti, A., Pitta, A., Ortaggi, G., Corti, M., Innocenti, C., Lascialfari, A., Marinone, M., Marzola, P., Daducci, A., Sbarbati, A., Micotti, E., Orsini, F., Poletti, G., Sangregorio, C., 2009. Synthesis and characterization of polyethylenimine-based iron oxide composites as novel contrast agents for MRI. *Magn. Reson. Mater. Phys., Biol. Med.* 22, 77-87.
- [17] Petri-Fink, A., Steitz, B., Finka, A., Salaklang, J., Hofmann, H., 2008. Effect of cell media on polymer coated superparamagnetic iron oxide nanoparticles (SPIONs): Colloidal stability, cytotoxicity, and cellular uptake studies. *Eur. J. Pharm. Biopharm.* 68, 129-137.

- 
- [18] Jain, A., Jain, S.K., 2008. PEGylation: an approach fro drug delivery. A review. *Crit. Rev. Ther. Drug Carrier Syst.* 25, 403-447.
- [19] Zhou, J.H., Huang, L., Wang, W.W., Pang, J., Zou, Y., Shuai, X.T., Gao, X., 2009. Prostate cancer targeted MRI nanoprobe based on superparamagnetic iron oxide and copolymer of poly(ethylene glycol) and polyethyleneimin. *Chin. Sci. Bull.* 54, 3137-3146.
- [20] Kissel, T., Petersen, H., Fischer, D., Kunath, K., von Harpe, A., 1999. Cationic Block Copolymers. WO/2001/005875.
- [21] Bee, A., Massart, R., Neveu, S., 1995. Synthesis of very fine maghemite particles. *J. Magn. Mater.* 149, 6-9.
- [22] Beattle, J.K., 1989. Monodisperse colloids of transition metal and lanthanide compounds. *Pure Appl. Chem.* 61, 937-941.
- [23] Yu, W.W., Falkner, J.C., Yavuz, C.T., Colvin, V.L., 2004. Synthesis of monodisperse iron oxide nanocrystals by thermal decomposition of iron carboxylate salts. *Chem. Commun. (Cambridge, U. K.)*, 2306-2307.
- [24] Si, S., Kotal, A., Mandal, T.K., Giri, S., Nakamura, H., Kohara, T., 2004. Size-Controlled Synthesis of Magnetite Nanoparticles in the Presence of Polyelectrolytes. *Chem. Mater.* 16, 3489-3496.

- 
- [25] Zhang, H., Gilbert, B., Huang, F., Banfield, J.F., 2003. Water-driven structure transformation in nanoparticles at room temperature. *Nature (London, U. K.)* 424, 1025-1029.
- [26] Patterson, A.L., 1939. The Scherrer formula for x-ray particle-size determination. *Phys. Rev.* 56, 978-982.
- [27] Lu, A.H., Salabas, E.L., Schueth, F., 2007. Magnetic nanoparticles: synthesis, protection, functionalization, and application. *Angew. Chem., Int. Ed.* 46, 1222-1244.
- [28] Schneider, M., Brinkmann, M., Moehwald, H., 2003. Adsorption of Polyethylenimine on Graphite: An Atomic Force Microscopy Study. *Macromolecules* 36, 9510-9518.
- [29] Petersen, H., Fechner, P.M., Fischer, D., Kissel, T., 2002. Synthesis, Characterization, and Biocompatibility of Polyethylenimine-graft-poly(ethylene glycol) Block Copolymers. *Macromolecules* 35, 6867-6874.
- [30] Yamaura, M., Camilo, R.L., Sampaio, L.C., Macedo, M.A., Nakamura, M., Toma, H.E., 2004. Preparation and characterization of (3-aminopropyl)triethoxysilane-coated magnetite nanoparticles. *J. Magn. Magn. Mater.* 279, 210-217.
- [31] Fang, C., Bhattarai, N., Sun, C., Zhang, M., 2009. Functionalized nanoparticles with long-term stability in biological media. *Small* 5, 1637-1641.
- [32] Owens, D.E., Peppas, N.A., 2006. Opsonization, biodistribution, and pharmacokinetics of polymeric nanoparticles. *Int. J. Pharm.* 307, 93-102.

- 
- [33] Corot, C., Robert, P., Idee, J.-M., Port, M., 2006. Recent advances in iron oxide nanocrystal technology for medical imaging. *Adv. Drug Delivery Rev.* 58, 1471-1504.
- [34] Hussain, S.M., Hess, K.L., Gearhart, J.M., Geiss, K.T., Schlager, J.J., 2005. In vitro toxicity of nanoparticles in BRL 3A rat liver cells. *Toxicol. in Vitro* 19, 975-983.
- [35] Leroueil, P.R., Berry, S.A., Duthie, K., Han, G., Rotello, V.M., McNerny, D.Q., Baker, J.R., Jr., Orr, B.G., Banaszak Holl, M.M., 2008. Wide varieties of cationic nanoparticles induce defects in supported lipid bilayers. *Nano Lett.* 8, 420-424.
- [36] Petersen, H., Fechner, P.M., Martin, A.L., Kunath, K., Stolnik, S., Roberts, C.J., Fischer, D., Davies, M.C., Kissel, T., 2002. Polyethylenimine-graft-Poly(ethylene glycol) Copolymers: Influence of Copolymer Block Structure on DNA Complexation and Biological Activities as Gene Delivery System. *Bioconjugate Chem.* 13, 845-854.
- [37] Beyerle, A., Merkel, O., Stoeger, T., Kissel, T., 2010. PEGylation affects cytotoxicity and cell-compatibility of poly(ethylene imine) for lung application: Structure-function relationships. *Toxicol. Appl. Pharmacol.* 242, 146-154.
- [38] Schulze, C., Kroll, A., Lehr, C.-M., Schaefer, U.F., Becker, K., Schnekenburger, J., Isfort, C.S., Landsiedel, R., Wohlleben, W., 2008. Not ready to use - overcoming pitfalls when dispersing nanoparticles in physiological media. *Nanotoxicology* 2, 51-61.

- 
- [39] Casula, M.F., Floris, P., Innocenti, C., Lascialfari, A., Marinone, M., Corti, M., Sperling, R.A., Parak, W.J., Sangregorio, C., 2010. Magnetic Resonance Imaging Contrast Agents Based on Iron Oxide Superparamagnetic Ferrofluids. *Chem. Mater.* 22, 1739-1748.

**Chapter 3      Cell uptake behavior of oppositely charged  
magnetic iron oxide nanoparticles – implications  
for subsequent cellular MR imaging**

---

---

**ABSTRACT**

Sufficient accumulation of magnetic iron oxide nanoparticles inside certain tissues is beneficial for cellular magnetic resonance (MR) imaging. In our opinion, the extent of cell internalization *in vitro* can be controlled by several measures, including modulation of size, surface charge and colloidal stability.

To investigate this, two series of maghemite ( $\gamma\text{-Fe}_2\text{O}_3$ ) nanoparticles modified with polymers of opposite charge, in detail poly(ethylene imine) (PEI) and a polymaleic anhydride derivative (PMA), were synthesized and thoroughly characterized with respect to size, zeta potential, colloidal stability and magnetic properties. Furthermore, the uptake rate of both formulations into A549 carcinoma cells after fluorescent labeling of the carriers, as well as the resulting alteration in MR relaxation times were evaluated. Intracellular iron levels after 24 hour incubation with  $\gamma\text{-Fe}_2\text{O}_3$ -PEI particles were found to be almost 10-fold higher than those of their negatively charged counterparts. In addition, effective signal darkening in  $T_2$ -weighted sequences was only achieved upon cellular incorporation of sufficient iron molarities, as it was seen for the  $\gamma\text{-Fe}_2\text{O}_3$ -PEI type.

These findings underscore the cooperative effect of surface charge and colloidal stability on uptake, and highlight  $\gamma\text{-Fe}_2\text{O}_3$ -PEI suspensions as potential agents for cell tracking purposes, where extensive iron internalization and contrast enhancement are of top priority.

**INTRODUCTION**

Magnetic iron oxide nanoparticles have moved into the focus of researchers due to their broad application range in biomedical disciplines, including drug delivery [1, 2], MR imaging [3, 4] and hyperthermia [5]. In recent years, much effort has been put into the development of iron

---

oxide-based tracking agents allowing the non-invasive detection of specific cell types. Most investigations in this segment concern the surveillance of stem cell movement after insertion into the human body [6]. Further studies have shown the possibility of localizing transplanted graft tissues and their potential rejection in immunocompetent models, respectively, after iron oxide loading [7]. Limitations to these concepts can arise, for example, from insufficient cellular accumulation of magnetic carriers, leading to deficient usage as image probes [8]. Combined with the fact that MR signal enhancement, caused by conventional iron oxide nanoparticles, is still unsatisfactory compared to that obtained with other imaging modalities such as PET [9], the necessity for either high particle loadings or more efficient assemblies becomes obvious [10]. Several factors influence the cellular uptake of nanoscale objects, amongst these size, surface properties, cell type and endocytotic pathways [11]. Labeling characteristics of superparamagnetic iron oxide nanoparticles of different size have been reported to be superior for larger diameters [12]. Moreover, surface functionalization with charged moieties is known to affect the cellular uptake of polymeric nanoparticles [13], and these findings have also been transferred to inorganic colloidal carriers [14]. In general, cationic magnetic nanoparticles were found to possess excellent properties for tracking applications, as they enter cells with higher effectiveness [15]. This has been proven for a variety of iron oxide formulations coated with polyelectrolytes of positive surface charge, such as poly(L-lysine) or dendritic guanidines [16]. However, thorough comparative analyses between oppositely charged magnetic nanoparticles are still missing. In order to accentuate the exclusive impact of surface charge on cellular accumulation of nanocarriers, in our opinion size effects have to be disabled by keeping particle dimensions constant. Apart from the overall uptake rate of nanoparticulate objects, their respective pathway of internalization is manipulated by surface charge [17]. This is of crucial importance, as compartmentalization of iron oxide carriers, evoked by several internalization mechanisms, has been reported to negatively affect the eventual relaxivity behavior in MR imaging [18]. Therefore, the



---

manipulation of non-phagocytic entering of nanocarriers into cells, which occurs mainly by adsorptive or receptor-mediated endocytosis and macropinocytosis [19], represents an interesting target. A parameter which is mostly excluded from *in vitro* internalization studies is agglomeration, although it contributes significantly to particle sedimentation, and subsequently to increased interaction with cell layers [20].

On the basis of this knowledge, we hypothesized that the cellular uptake rate of polymer-coated magnetic nanoparticles can be favorably enhanced *in vitro*, by using cationic species with reduced colloidal stability. Resultant from that, total iron loading levels are supposed to increase, thereby facilitating the detection by MR imaging. To support our assumptions, we developed two size-equivalent formulations of iron oxide modified with oppositely charged polymers by different synthesis routes, and studied their internalization kinetics and the localization inside carcinoma cells. In addition, the thus produced cells were fixed in tissue-imitating agarose phantoms, and subjected to specific magnetic resonance measurement sequences.

## **MATERIALS AND METHODS**

### **Chemicals**

Iron(II)chloride tetrahydrate and iron(III)chloride hexahydrate were purchased from Sigma Aldrich (Taufkirchen, Germany). Branched poly(ethylene imine) (PEI) with a molecular weight of 25,000 Da was a gift from BASF (Ludwigshafen, Germany). Fluorescein isothiocyanate (FITC) and Dy636 were from Sigma Aldrich (Taufkirchen, Germany) and Dyomics (Jena, Germany), respectively. All chemicals were obtained from commercial sources, and used as received without further purification.

---

**Synthesis  $\gamma$ -Fe<sub>2</sub>O<sub>3</sub>-PEI / particle system I**

Iron oxide nanoparticles of the maghemite type were prepared via aqueous coprecipitation, according to the Massart protocol [21]. Briefly, ammonia solution (2.6 mL, 25 % w/v) was added to a slightly acidic solution of iron(III) chloride hexahydrate and iron(II)chloride tetrahydrate (100 mL, 0.13 M, molar ratio 2:1) under constant stirring, until persistence of a black slurry. Nanoparticles were collected by a permanent magnet and washed thrice with ultra pure water, then refluxed in a mixture of nitric acid (2 N HNO<sub>3</sub>) and iron(III)nitrate nonahydrate (0.34 M) at 90 °C for 30 minutes. The precipitate was gathered by magnetic decantation, and subsequently dispersed in water to yield a stable maghemite suspension. Following that, dispersions were reacted with poly(ethylene imine) (PEI) solution at a defined mass ratio of [Fe] to [PEI] of 1:2 under vigorous shaking for 30 minutes. Unbound polymer was removed by extensive dialysis across Spectra/Por® membranes with MWCO 100,000 Da (Carl Roth, Karlsruhe, Germany).

**Synthesis  $\gamma$ -Fe<sub>2</sub>O<sub>3</sub>-PMA / particle system II**

Nanocrystals of the  $\gamma$ -Fe<sub>2</sub>O<sub>3</sub> type were prepared according to the method described by Hyeon and coworkers [22]. Briefly, 10 mL of octyl ether and 1.28 g of oleic acid were mixed and degassed in a 50 mL flask at 60 °C for 20 minutes. Then, 0.29 mL of Fe(CO)<sub>5</sub> were added at 100 °C and the solution was heated up slowly to refluxing temperature (~ 300 °C) for 1 h. The solution was cooled down to room temperature, and 0.34 g of (CH<sub>3</sub>)<sub>3</sub>NO were added. The mixture was heated up and maintained at 130 °C for 2 h, then refluxed at 300 °C for another 2 h. After stopping the reaction, particles were precipitated by addition of anhydrous toluene and methanol, followed by alternating washing steps with toluene and methanol, and final redispersion of particles in toluene (hydrophobic nanoparticles).

Amphiphilic poly(maleic anhydride) derivative (PMA) was synthesized and used for the transfer of hydrophobic nanoparticles to aqueous solution, according to a previously

---

published protocol [23]. Briefly, 500  $\mu\text{L}$  of amphiphilic polymer solution (0.5 M) were mixed with 2 mL of hydrophobic nanoparticles (0.48  $\mu\text{M}$ ). After mixing, the solvent was slowly evaporated under reduced pressure, until the sample was completely dried. The remaining solid film was redissolved in SBB (sodium borate, 50 mM, pH 12) under vigorous stirring to yield clear nanosuspensions of  $\gamma\text{-Fe}_2\text{O}_3\text{-PMA}$  particles.

### **Physicochemical characterization**

Size and morphology of the synthesized iron oxide cores were investigated on a JEM-3010 transmission electron microscope (Jeol Germany, Echting, Germany) at an acceleration voltage of 300 kV. Maghemite suspension droplets were placed onto carbon-coated copper grids S160-3 (Plano, Wetzlar, Germany) and allowed to dry. Core dimensions were calculated by averaging at least 200 diameters registered by ImageJ software.

Hydrodynamic diameters and zeta potentials of nanoparticles after polymer functionalization were assessed by dynamic light scattering (DLS) and laser Doppler anemometry (LDA), using a Zetasizer Nano ZS (Malvern Instruments, Herrenberg, Germany). DLS measurements were performed at 25 °C after appropriate dilution of the respective samples with ultra pure water, to avoid multiscattering events. As to LDA analysis, samples were dispersed in sodium chloride (10 mM) in order to maintain a constant ionic strength.

For magnetization studies, small amounts of lyophilized material (~ 1.5 mg) were placed into a Magnetic Property Measurement System MPMS® equipped with 5 T magnet (Quantum Design, San Diego, CA) using superconducting quantum interference device (SQUID) technology. Magnetization values of the samples were surveyed during a field-dependent sweep from  $-55,000$  to  $55,000$  Oe at room temperature.

---

### **Iron quantification**

ICP-OES (inductively coupled plasma - optical emission spectroscopy) technology was applied for [Fe] quantification. After lysis of iron oxide nanoparticle systems with nitric acid (65 % w/v), absorbance of samples was measured at three different wavelengths (238.2 nm, 239.6 nm, 259.9 nm) on an Optima 2000 DV (PerkinElmer, Rodgau, Germany). Amounts of iron were calculated by standardization to internal standard yttrium(III)chloride.

### **Labeling of particle systems**

For fluorescent tagging of particle system I, green dye FITC was conjugated to PEI as previously described [24]. The labeled polymer was attached to naked maghemite nanoparticles analogous to the synthesis protocol, thereby yielding  $\gamma$ -Fe<sub>2</sub>O<sub>3</sub>-PEI-FITC carriers.

Particle system II was tagged with red marker Dy636 in a two-step process. First, 1 mg of amine-containing dye was dissolved in 0.4 mL of methanol and reacted with 0.5 mL of PMA solution in CHCl<sub>3</sub>. The solvent mixture was exchanged to anhydrous chloroform, and the final polymer concentration was set to 10 mM. Then, 2.5 mL of Dy636 modified amphiphilic polymer were mixed with 2 mL of hydrophobic  $\gamma$ -Fe<sub>2</sub>O<sub>3</sub> nanoparticles (0.48  $\mu$ M). The mixture was treated analogously to abovementioned unlabeled particles to yield stable  $\gamma$ -Fe<sub>2</sub>O<sub>3</sub>-PMA-Dy636 nanosuspensions.

### **Cell culture and uptake studies**

Human lung adenocarcinoma cell line A549 was maintained in DMEM high glucose containing 10 % FCS and L-glutamine without the addition of antibiotics in a humidified atmosphere at 37 °C and 8.5 % CO<sub>2</sub>.

For experiments on uptake kinetics, cells were seeded onto 24-well plates at a density of 60,000 per well. After awaiting adherent growth, culture medium was exchanged with

DMEM supplemented with 5 % FCS, in order to avoid interference with the assay reagents. Immediately after this, the wells were incubated with either particle system I or particle system II at fixed iron concentrations ( $1 \mu\text{g mL}^{-1}$ ). For the purpose of comparison, blank cells and wells treated with unlabeled particle species were included. Following definite incubation times (5 min, 15 min, 30 min, 60 min, 2 h, 4 h, 8 h, 24 h), cells were washed twice with PBS, trypsinized and fixed in a 1:1 mixture of FACSFlow<sup>TM</sup> and paraformaldehyde (4 % w/v). Cell dispersions prepared in this way were analyzed with respect to their fluorescent intensity via flow cytometry (FACS), using a FACSCanto II (BD Biosciences, San Jose, CA). Signals from a total of 10,000 cells were recorded on channels 488 nm and 630 nm, respectively.

### **Agarose phantom relaxometry**

A549 cells were plated at a density of 100,000 per well, and incubated with iron oxide suspensions of different types ( $\gamma\text{-Fe}_2\text{O}_3\text{-PEI}$  and  $\gamma\text{-Fe}_2\text{O}_3\text{-PMA}$ ) and concentrations (1, 10, 30 and  $50 \mu\text{g mL}^{-1}$ ) for 24 hours. After PBS washing and trypsinization, cell numbers were counted by means of a Neubauer chamber. Quantification of cell-internalized iron was realized by ICP-OES after cell lysis in concentrated nitric acid ( $600 \mu\text{L}$ ) for 4 hours. Phantoms for MR relaxometry were produced by dispersing  $10^5$  doped A549 cells in agarose (1 % w/v). Magnetic resonance (MR) imaging studies concerning the  $T_2$  and  $T_2^*$  relaxation times of the respective phantoms were carried out on a 7 T Bruker ClinScan 70/30 USR (Bruker BioSpin, Rheinstetten, Germany). For measurements of transverse  $T_2$  relaxation times, spin-echo multicontrast sequences were run at  $T_R$  values of 2000 ms, varying spin echo times  $T_E$  (10-120 ms with an increment of 10 ms), field of view  $75 \times 75$  mm, matrix  $128 \times 128$  and slice thickness 0.6 mm. Data quantification was achieved by evaluating the such created DICOM images. Relaxation times  $T_2$  could be derived by analyzing regions of interest (ROI) within  $T_2$  maps generated by the overlay of successive spin-echo images, using a monoexponential fitting of the signal intensity ( $SI$ ) decay curve:  $SI(t) = S_0 \exp(-t/T_2)$ , where

$S_0$  is the signal magnitude at equilibrium and  $t$  the particular echo time. Effective transverse relaxation times ( $T_2^*$ ) were calculated from  $T_2^*$ -weighted images taken with the following settings: gradient-echo multicontrast with  $T_R$  350 ms, multiple spin echo times  $T_E$  (3-32 ms), field of view 89x89 mm, matrix 128x128, slice thickness 0.5 mm.  $T_2^*$  values were obtained correspondingly by fitting the MRI signal intensities of the acquired maps versus echo times  $T_E$ .

## RESULTS

The different synthesis strategies for formation of  $\gamma\text{-Fe}_2\text{O}_3$  nanoparticles clearly had an impact on the resulting morphology (*Figure 1*). While inorganic cores generated by aqueous coprecipitation (particle system I) were found to be irregularly shaped, those coming from thermal decomposition of organometallic precursor molecules were of perfect spherical shape (particle system II).

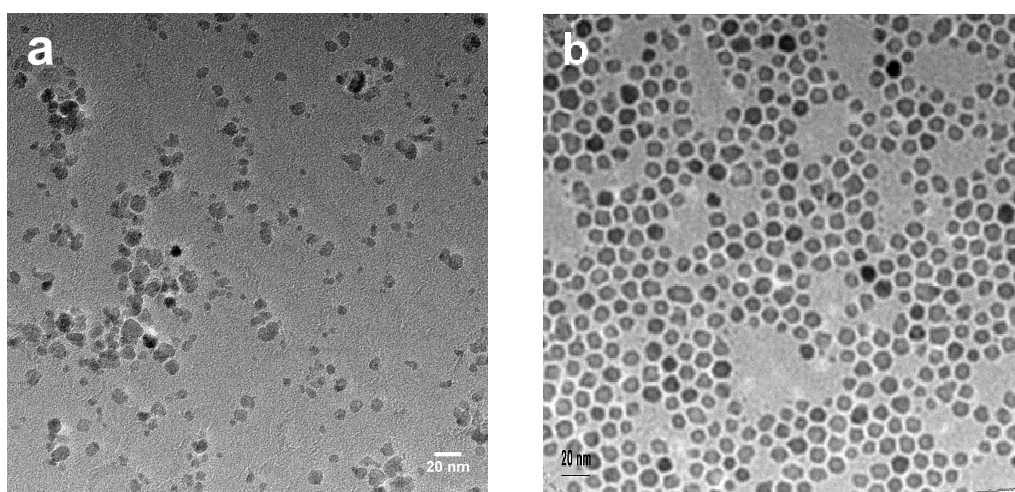


*Figure 1. Transmission electron micrographs depicting the morphology of  $\gamma\text{Fe}_2\text{O}_3$  nanoparticles after synthesis by (a) aqueous precipitation route and (b) thermal decomposition of organometallic precursors.*

Analysis of Feret diameters on TEM micrographs further revealed mean diameters of  $10.4 \pm 2.4$  nm and  $10.8 \pm 0.12$  nm for the two setups, respectively. Adsorptive attachment of poly(ethylene imine) completed particle system I ( $\gamma$ -Fe<sub>2</sub>O<sub>3</sub>-PEI), whereas intercalation of polymer strands between surfactant alkyl chains formed the final step in producing particle system II ( $\gamma$ -Fe<sub>2</sub>O<sub>3</sub>-PMA). Hydrodynamic diameters for the two polymer-modified formulations, as measured by dynamic light scattering, amounted to  $38.8 \pm 0.3$  nm and  $37.4 \pm 0.8$  nm. Both types of nanoparticle suspensions exhibited unimodal size distributions and zeta potentials of comparable absolute value, in numbers  $16.8 \pm 1.1$  mV for  $\gamma$ -Fe<sub>2</sub>O<sub>3</sub>-PEI and  $-18.7 \pm 0.6$  mV for  $\gamma$ -Fe<sub>2</sub>O<sub>3</sub>-PMA (Table 1).

	hydrodynamic diameter [nm]	polydispersity index	zeta potential [mV]	saturation magnetization [emu g <sup>-1</sup> ]
$\gamma$ -Fe <sub>2</sub> O <sub>3</sub> -PEI	$38.8 \pm 0.3$	$0.144 \pm 0.019$	$16.8 \pm 1.1$	23.7
$\gamma$ -Fe <sub>2</sub> O <sub>3</sub> -PMA	$37.4 \pm 0.8$	$0.321 \pm 0.025$	$-18.7 \pm 0.6$	16.4

Table 1. Physicochemical parameters of magnetic iron oxide nanoparticles.

The impact of preparation technology on magnetic features of the samples was investigated by monitoring field-dependent magnetization data on a SQUID system (Figure 2). All recorded curves showed lack of remanence and typical sigmoidal characteristics. Saturation magnetizations, i.e. the states of maximum alignment of magnetic spins at strong external fields, were derived by tangential fitting of the curve maxima. Numerical values decreased from 54.6 to 23.7 emu g<sup>-1</sup> for particle system I after actual coating with poly(ethylene imine).

For counterparts  $\gamma\text{-Fe}_2\text{O}_3\text{-PMA}$ , values were reduced from  $27.7 \text{ emu g}^{-1}$  for hydrophobic  $\gamma\text{-Fe}_2\text{O}_3$  after organic synthesis (data not shown) to  $16.4 \text{ emu g}^{-1}$ .

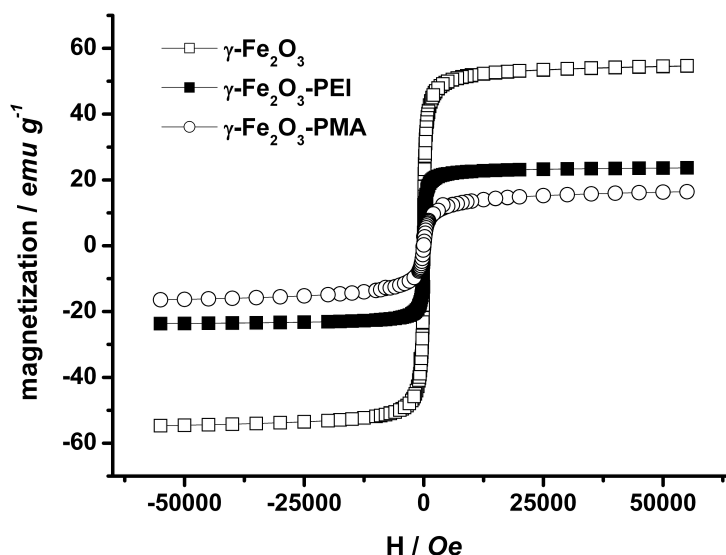


Figure 2. Field-dependent magnetization curves of bare ( $\gamma\text{Fe}_2\text{O}_3$  from aqueous synthesis) and polymer-coated ( $\gamma\text{Fe}_2\text{O}_3\text{-PEI}$  and  $\gamma\text{Fe}_2\text{O}_3\text{-PMA}$ ) iron oxide nanoparticles at 298 K.

When incubating A549 cells with fluorophore-bearing particle systems I and II, different qualitative uptake patterns were observed for the two species. Positively charged  $\gamma\text{-Fe}_2\text{O}_3\text{-PEI-FITC}$  nanoparticles were internalized in a steady manner over the examined period of 24 hours, with the predominant uptake taking place within the first two hours after incubation (Figures 3a and b). Single-peaked mean fluorescence intensity signals indicated, that there were no cell population subsets with lower degrees of particle incorporation. In contrast to that, negatively charged particles  $\gamma\text{-Fe}_2\text{O}_3\text{-PMA-Dy636}$  were seen to accumulate in cells only to a small extent within two hours. The major fraction of these carriers was incorporated between time points 4 and 24 hours, mostly after 8 hours. Interestingly,  $\gamma\text{-Fe}_2\text{O}_3\text{-PMA-Dy636}$  were incorporated faster by the cells in the presence of  $\gamma\text{-Fe}_2\text{O}_3\text{-PEI-FITC}$ .



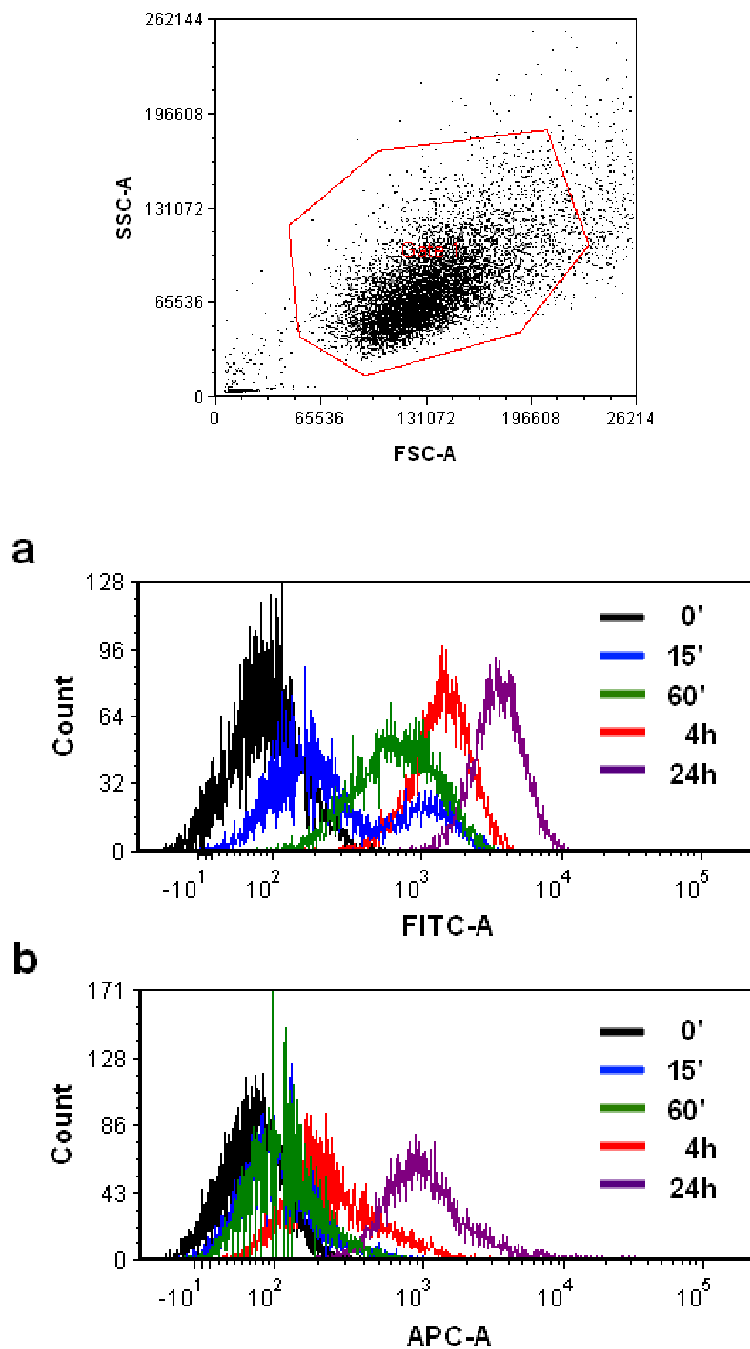
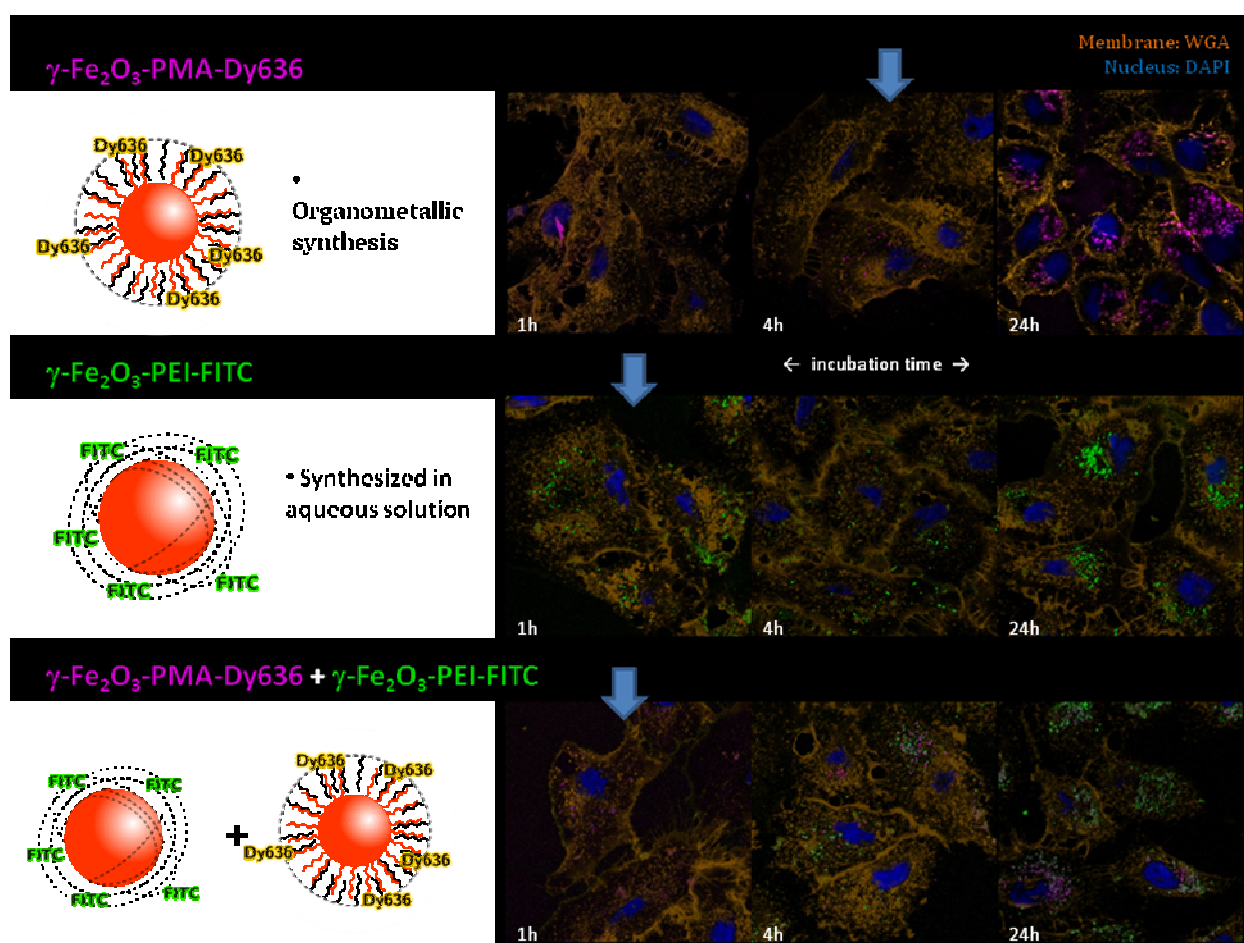


Figure 3. Cellular uptake kinetics of nanoparticle formulations  $\gamma\text{Fe}_2\text{O}_3\text{-PEI-FITC}$  (a) and  $\gamma\text{Fe}_2\text{O}_3\text{-PMA-Dy636}$  (b). Cells were incubated with distinct amounts of the respective particle systems ( $1\ \mu\text{g}$  [Fe]) for time periods of 15 min, 60 min, 4 h and 24 h. Fluorescence intensities were recorded by means of flow cytometry for a total of 10,000 events on channels FITC (excitation 488 nm) and APC-A (630 nm). (Dot plot used for cell gating is shown on the upper chart.)

Intensity signals were measured via confocal laser scanning microscopy (*Figure 4*) and FACS, but as measurements were performed on different FACS channels and labeling efficiencies of the two particle systems were not homogenous, absolute comparability between  $\gamma\text{-Fe}_2\text{O}_3\text{-PEI-FITC}$  and  $\gamma\text{-Fe}_2\text{O}_3\text{-PMA-Dy636}$  was not given before quantification of cell iron via ICP-OES, following analogous incubation regimes.



*Figure 4. Investigations on cellular uptake kinetics of nanoparticle formulations  $\gamma\text{Fe}_2\text{O}_3\text{-PMA-Dy636}$  (top),  $\gamma\text{Fe}_2\text{O}_3\text{-PEI-FITC}$  (middle), and a co-incubation mixture of both (bottom) by means of laser scanning confocal imaging. A549 cells were incubated with the corresponding nanoparticles, and the cell membranes as well as the nucleus were stained with wheat germ agglutinin – alexa 594 or DAPI, respectively.*

When cells were exposed to particle system I at an initial dose of one microgram [Fe], about 12 % of this amount were found to be internalized after 24 hours. Consistent with the findings from flow cytometry, the uptake of this species increased constantly over time. Unlike that, particle system II invaded A549 cells to a significantly lower extent of 1.5 %. Data points after 15 and 60 minutes were indistinguishable from background, and the most pronounced rise in intracellular iron mass appeared after four hours. Nevertheless, the results from ICP-OES correlated well with MFI values from flow cytometry, as indicated by the calculated coefficients of determination for each of the formulations ( $R^2 = 0.993$  and  $R^2 = 0.990$  for  $\gamma\text{-Fe}_2\text{O}_3\text{-PEI-FITC}$  and  $\gamma\text{-Fe}_2\text{O}_3\text{-PMA-Dy636}$ , respectively) (Figure 5).

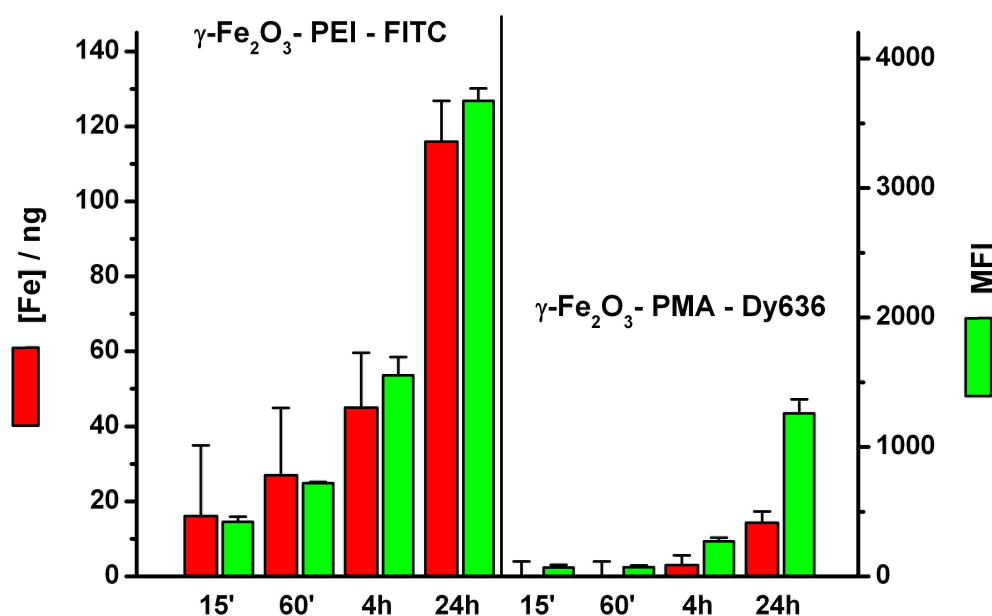


Figure 5. Quantification of absolute intracellular iron contents after 24 h incubation of A549 cells with formulations  $\gamma\text{-Fe}_2\text{O}_3\text{-PEI-FITC}$  and  $\gamma\text{-Fe}_2\text{O}_3\text{-PMA-Dy636}$  (red bars). Correlation of these data with mean fluorescence intensity values gained after identical cell treatment (green bars) were performed for comparison of methods ICP-OES and flow cytometry.

Relaxation parameters of manufactured agarose phantoms containing doped cells were dependent on the effective amounts of iron per cell. As expected, A549 incubation with high iron molarities caused non-proportional enhancement of intracellular accumulation. For particle system I, maximum incubation with a total of 50  $\mu\text{g}$  [Fe], for instance, led to intracellular iron levels of 6.9 pg per cell, and subsequent relaxation rates  $R_2^*$  of 23.0  $\text{s}^{-1}$ . An identical application scheme of particle system II resulted in values of 1.4 pg per cell and 8.2  $\text{s}^{-1}$ .

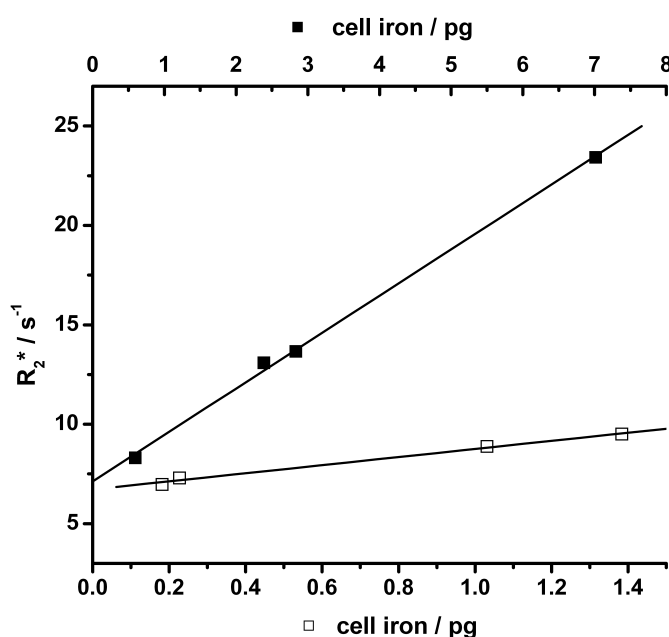


Figure 6. Relaxation rates  $R_2^*$  of agarose phantoms containing  $10^5$  cells doped with maghemite nanoparticles. Data points represent intracellular iron levels after incubation with increasing amounts of  $\gamma\text{Fe}_2\text{O}_3\text{-PEI}$  (■) and  $\gamma\text{Fe}_2\text{O}_3\text{-PMA}$  (□), respectively (1, 10, 30 and 50  $\mu\text{g}$  [Fe]).

Despite the discrepancy in absolute  $R_2^*$  numbers, the efficiency of both iron oxide nanoparticle setups in reducing transverse relaxation times, often denoted as relaxivity  $r_2^*$ , turned out to be equivalent, as derived from comparison of the slopes of the best-fit lines (Figure 6).

---

## DISCUSSION

In order to study the role of surface chemistry in modulation of cellular uptake and relaxometric performance, maghemite nanoparticles prepared from alternative synthesis routes were modified with positively charged poly(ethylene imine) and negatively charged PMA, respectively. Much effort had to be put into the establishment of manufacturing protocols for the two different carrier systems, due to the fact that equal dimensions of the fabricated iron oxide cores and the entire polymer-coated nanoparticles were required for comparison purposes. We created particle systems of opposite surface potential with the above specifications, namely  $\gamma\text{-Fe}_2\text{O}_3\text{-PEI}$  and  $\gamma\text{-Fe}_2\text{O}_3\text{-PMA}$ . The discrimination between both particle setups, apart from the measured zeta potentials, was possible by investigating the regularity in morphology of precipitated maghemite crystals. Relatively wide size distribution and non-controllable shape of particles are the two main drawback criteria suffered from the aqueous coprecipitation route [25]. However, keeping in mind the scope of biomedical application, these slightly negative features are compensated by the easy handling and the absence of organic solvents. Additionally, synthesis strategy seems to affect magnetic properties of the fabricated iron oxide nanoparticles. It is well-known that magnetization of inorganic colloids is determined primarily by their crystal diameter. As maghemite core dimensions were found to be almost identical, we assume that crystallinity represents the essential parameter for variation in overall saturation magnetizations ( $M_{sat}$ ) of the two particle systems. Another explanation for the differing  $M_{sat}$  values might be the existence of a magnetically dead layer on the maghemite surface, which does not contribute to the collective magnetic moment of  $\gamma\text{-Fe}_2\text{O}_3$  nanoparticles. The general reduction in magnetization, with respect to bulk maghemite [26], can be attributed to several mechanisms, such as spin canting or spin-glass-like behavior of the surface spins, both of them being effects which become more and more important with decreasing particle size. Polymer shielding of the naked iron

---

oxide cores induced further lowering of gram-standardized saturation magnetizations, which appears logical as the organic material does not add to the magnetic properties of the respective particle systems. Moreover, organic ligands used to stabilize magnetic nanoparticles lead to quenching of surface magnetic moments [27]. Displayed sigmoidal curves are indicative of superparamagnetism of both  $\gamma$ -Fe<sub>2</sub>O<sub>3</sub>-PEI and  $\gamma$ -Fe<sub>2</sub>O<sub>3</sub>-PMA. This feature is not only beneficial due to the availability of giant magnetic moments, but also due to the reduction in agglomeration tendency, which is attributable to complete paramagnet-like loss of magnetization at zero external field.

Several models have been stated for the internalization of differently charged iron oxide nanoparticles [28]. However, no efforts have been made so far to directly compare particle systems of equal dimensions and opposite charge with respect to their cellular uptake rate. Consequently, our approach consisted in eliminating size as a key factor for nanoparticle uptake by keeping the diameters of the two formulations constant. We hypothesized that, under these circumstances, the invasion into cells was only dependent on the surface potential and the colloidal stability of incubated carriers. The steady, but nonlinear uptake pattern of positively charged  $\gamma$ -Fe<sub>2</sub>O<sub>3</sub>-PEI carriers suggests the involvement of a saturable, receptor-mediated mechanism of cell intrusion. Other internalization routes proposed for magnetic iron oxide nanoparticles are macropinocytosis and adsorptive endocytosis [29]. The low extent of uptake for  $\gamma$ -Fe<sub>2</sub>O<sub>3</sub>-PMA particles after 24 hours was most striking. Electrostatic interactions with the negatively charged cell membrane certainly favor fast attachment and subsequent ingestion of cationic species  $\gamma$ -Fe<sub>2</sub>O<sub>3</sub>-PEI, but can hardly explain the extreme discrepancies observed. Thus, our opinion is that colloidal stability of the respective nanoparticle systems plays a cooperative role not to be underestimated in uptake kinetics. In the course of the experiments, primary agglomerates dispersed in the supernatant tend to sediment more rapidly onto the ground cell layer, according to Stokes' Law. The aggregation tendency, as indicated by findings from gel electrophoresis measurements, is significantly increased for positively

---

charged  $\gamma\text{-Fe}_2\text{O}_3\text{-PEI}$  particles. Consequently, the particle-cell contact area is largely enhanced, leading to higher total internalization rates. Although the phenomenon of colloidal instability drastically limits the application of such carrier systems, their rapid enrichment in certain tissues *in vitro* outbalances this drawback. Sufficient and fast loading of certain cell types is, for example, desired for tracking purposes via magnetic resonance imaging [30]. The reason for this is the concentration-dependent enhancement of transverse proton relaxation in the vicinity of areas containing magnetic iron oxide, thus leading to quick fading of MR signals and gain of contrast in  $T_2$ -weighted images [31]. Based on that knowledge, particle system  $\gamma\text{-Fe}_2\text{O}_3\text{-PEI}$  should perform superior to its anionic counterpart, when being used for cell tracking tasks. In order to corroborate that hypothesis, agarose phantoms containing iron-labeled cancer cells were subjected to MR measurement sequences. Phantom matrices act as versatile human tissue equivalents, as alteration of their basic composition allows for the imitation of specific intracorporal regions, and appendant relaxation properties [32]. Most effective signal darkening in  $T_2$ -weighted maps, denoted as high absolute relaxation rate values  $R_2^*$ , was observed for cell dispersions carrying large amounts of  $\gamma\text{-Fe}_2\text{O}_3\text{-PEI}$ . However, the effects were not as pronounced as for freely dispersed nanoparticles. We explain this behavior by the intracellular confinement of magnetic iron oxide carriers, which has a strong impact on the detected proton relaxation times [33]. Coming back to the magnetization properties of the tested formulations, we predicted higher molar relaxivities for the system  $\gamma\text{-Fe}_2\text{O}_3\text{-PEI}$ , due to enhanced magnetic interactions with surrounding proton spins. Surprisingly, the efficiencies of both tested formulations were found to be in the same range. The relativization of this parameter is, in our opinion, a consequence of the clustering of particles brought about by both colloidal instability and organelle compartmentalization. Altogether, the results point out that magnetic iron oxide nanoparticles of the  $\gamma\text{-Fe}_2\text{O}_3\text{-PEI}$  type are promising for cell labeling and subsequent tracking purposes.

---

## CONCLUSIONS

We successfully synthesized iron oxide nanoparticle systems of opposite charge, and evaluated them with respect to physicochemical properties, cell uptake patterns and relaxometric performance. Surface modification of the generated carriers was found to be the key factor governing the internalization into cells. Positively charged  $\gamma$ -Fe<sub>2</sub>O<sub>3</sub>-PEI particles accumulated rather rapidly, due to a synergistic dual mechanism of attractive forces to the cell membrane on the one hand, and deficient colloidal stability on the other hand. Although slight agglomeration tendency of nano-sized particles restricts their applicability *in vivo*, this problem is of minor importance for *in vitro* purposes. Cells incubated with  $\gamma$ -Fe<sub>2</sub>O<sub>3</sub>-PEI compounds revealed high numeric iron loadings, and subsequently effective signal darkening in MR sequences. These findings suggest  $\gamma$ -Fe<sub>2</sub>O<sub>3</sub>-PEI suspensions as promising agents for cell tracking purposes, where extensive iron uptake and contrast enhancement are premium requirements.

## ACKNOWLEDGEMENTS

The authors wish to thank Eva Mohr, Department of Pharmaceutics and Biopharmacy, Marburg, Germany for assistance in the cell culture lab and Clemens Pietzonka for helpful discussions concerning magnetic phenomena.



---

**REFERENCES**

- [1] Tartaj, P., Morales, M.P., Veintemillas-Verdaguer, S., Gonzalez-Carreno, T., Serna, C.J., 2003. The preparation of magnetic nanoparticles for applications in biomedicine. *J. Phys. D: Appl. Phys.* 36, R182-R197.
  
- [2] Tran, N., Pareta, R., Taylor, E., Webster, T.J., Iron oxide nanoparticles: novel drug delivery materials for treating bone diseases. *Adv. Mater. Res. (Zuerich, Switz.)* 89-91, 411-418.
  
- [3] Bulte, J.W.M., Kraitchman, D.L., 2004. Iron oxide MR contrast agents for molecular and cellular imaging. *NMR Biomed.* 17, 484-499.
  
- [4] Jin, A.Y., Tuor, U.I., Rushforth, D., Filfil, R., Kaur, J., Ni, F., Tomanek, B., Barber, P.A., 2009. Magnetic resonance molecular imaging of post-stroke neuroinflammation with a P-selectin targeted iron oxide nanoparticle. *Contrast Media Mol. Imaging* 4, 305-311.
  
- [5] Thiesen, B., Jordan, A., 2008. Clinical applications of magnetic nanoparticles for hyperthermia. *Int. J. Hyperthermia* 24, 467-474.
  
- [6] Bulte J.W.M., 2009. In vivo MRI cell tracking: clinical studies. *AJR Am J Roentgenol* 193, 314-325.

- 
- [7] Winter, E.M., Hogers, B., van der Graaf, L.M., Gittenberger-de Groot, A.C., Poelmann, R.E., van der Weerd, L., Cell tracking using iron oxide fails to distinguish dead from living transplanted cells in the infarcted heart. *Magn. Reson. Med.* 63, 817-821.
- [8] Huang, H.-C., Chang, P.-Y., Chang, K., Chen, C.-Y., Lin, C.-W., Chen, J.-H., Mou, C.-Y., Chang, Z.-F., Chang, F.-H., 2009. Formulation of novel lipid-coated magnetic nanoparticles as the probe for in vivo imaging. *J. Biomed. Sci. (London, U. K.)* 16:86.
- [9] Lee, J.-H., Huh, Y.-M., Jun, Y.-w., Seo, J.-w., Jang, J.-t., Song, H.-T., Kim, S., Cho, E.-J., Yoon, H.-G., Suh, J.-S., Cheon, J., 2007. Artificially engineered magnetic nanoparticles for ultra-sensitive molecular imaging. *Nat Med* 13, 95-99.
- [10] Lu, C.-W., Hung, Y., Hsiao, J.-K., Yao, M., Chung, T.-H., Lin, Y.-S., Wu, S.-H., Hsu, S.-C., Liu, H.-M., Mou, C.-Y., Yang, C.-S., Huang, D.-M., Chen, Y.-C., 2007. Bifunctional Magnetic Silica Nanoparticles for Highly Efficient Human Stem Cell Labeling. *Nano Lett.* 7, 149-154.
- [11] Mailander, V., Landfester, K., 2009. Interaction of nanoparticles with cells. *Biomacromolecules* 10, 2379-2400.
- [12] Sun, R., Dittrich, J., Le-Huu, M., Mueller Margareta, M., Bedke, J., Kartenbeck, J., Lehmann Wolf, D., Krueger, R., Bock, M., Huss, R., Seliger, C., Grone, H.-J., Misselwitz, B., Semmler, W., Kiessling, F., 2005. Physical and biological characterization of superparamagnetic iron oxide- and ultrasmall superparamagnetic iron oxide-labeled cells: a comparison. *Invest Radiol* 40, 504-513.

- 
- [13] Chung, Y.-I., Kim, J.C., Kim, Y.H., Tae, G., Lee, S.-Y., Kim, K., Kwon, I.C., The effect of surface functionalization of PLGA nanoparticles by heparin- or chitosan-conjugated Pluronic on tumor targeting. *J. Controlled Release* 143, 374-382.
- [14] Ge, Y., Zhang, Y., Xia, J., Ma, M., He, S., Nie, F., Gu, N., 2009. Effect of surface charge and agglomerate degree of magnetic iron oxide nanoparticles on KB cellular uptake in vitro. *Colloids Surf., B* 73, 294-301.
- [15] Villanueva, A., Canete, M., Roca, A.G., Calero, M., Veintemillas-Verdaguer, S., Serna, C.J., Morales, M.d.P., Miranda, R., 2009. The influence of surface functionalization on the enhanced internalization of magnetic nanoparticles in cancer cells. *Nanotechnology* 20, 115103/115101-115103/115109.
- [16] Martin, A.L., Bernas, L.M., Rutt, B.K., Foster, P.J., Gillies, E.R., 2008. Enhanced Cell Uptake of Superparamagnetic Iron Oxide Nanoparticles Functionalized with Dendritic Guanidines. *Bioconjugate Chem.* 19, 2375-2384.
- [17] Harush-Frenkel, O., Rozentur, E., Benita, S., Altschuler, Y., 2008. Surface Charge of Nanoparticles Determines Their Endocytic and Transcytotic Pathway in Polarized MDCK Cells. *Biomacromolecules* 9, 435-443.
- [18] Billotey, C., Wilhelm, C., Devaud, M., Bacri, J.C., Bittoun, J., Gazeau, F., 2003. Cell internalization of anionic maghemite nanoparticles: quantitative effect on magnetic resonance imaging. *Magn. Reson. Med.* 49, 646-654.

- 
- [19] Hillaireau, H., Couvreur, P., 2009. Nanocarriers' entry into the cell: Relevance to drug delivery. *Cell. Mol. Life Sci.* 66, 2873-2896.
- [20] Limbach, L.K., Li, Y., Grass, R.N., Brunner, T.J., Hintermann, M.A., Muller, M., Gunther, D., Stark, W.J., 2005. Oxide Nanoparticle Uptake in Human Lung Fibroblasts: Effects of Particle Size, Agglomeration, and Diffusion at Low Concentrations. *Environ. Sci. Technol.* 39, 9370-9376.
- [21] Bee, A., Massart, R., Neveu, S., 1995. Synthesis of very fine maghemite particles. *J. Magn. Magn. Mater.* 149, 6-9.
- [22] Hyeon, T., Lee, S.S., Park, J., Chung, Y., Na, H.B., 2001. Synthesis of Highly Crystalline and Monodisperse Maghemite Nanocrystallites without a Size-Selection Process. *J. Am. Chem. Soc.* 123, 12798-12801.
- [23] Chang, W.H.-S., Lin, C.-A.J., Li, J.K.-J., Oheim, M., Yakovlev, A., Feltz, A., Luccardini, C., Fernandez-Arguelles, M.T., Sperling, R.A., Parak, W.J., 2009. Amphiphilic polymer, method for forming the same and application thereof. (Chung Yuan Christian University, Taiwan). Application: US2009036625 (A1), 12 pp.
- [24] Gautam, A., Densmore, C.L., Golunski, E., Xu, B., Waldrep, J.C., 2001. Transgene expression in mouse airway epithelium by aerosol gene therapy with PEI-DNA complexes. *Mol. Ther.* 3, 551-556.

- 
- [25] Lu, A.-H., Salabas, E.L., Schuth, F., 2007. Magnetic nanoparticles: synthesis, protection, functionalization, and application. *Angew Chem Int Ed Engl* 46, 1222-1244.
- [26] Fiorani, D., Testa, A.M., Lucari, F., D'Orazio, F., Romero, H., 2002. Magnetic properties of maghemite nanoparticle systems: surface anisotropy and interparticle interaction effects. *Physica B (Amsterdam, Neth.)* 320, 122-126.
- [27] Paulus, P.M., Bonnemann, H., Van der Kraan, A.M., Luis, F., Sinzig, J., De Jongh, L.J., 1999. Magnetic properties of nano-sized transition metal colloids: the influence of noble metal coating. *Eur. Phys. J. D* 9, 501-504.
- [28] He, C., Hu, Y., Yin, L., Tang, C., Yin, C., Effects of particle size and surface charge on cellular uptake and biodistribution of polymeric nanoparticles. *Biomaterials* 31, 3657-3666.
- [29] Moore, A., Weissleder, R., Bogdanov, A., Jr., 1997. Uptake of dextran-coated monocrystalline iron oxides in tumor cells and macrophages. *J Magn Reson Imaging* 7, 1140-1145.
- [30] Himmelreich, U., Dresselaers, T., 2009. Cell labeling and tracking for experimental models using Magnetic Resonance Imaging. *Methods (Amsterdam, Neth.)* 48, 112-124.

- 
- [31] Laurent, S., Boutry, S., Mahieu, I., Vander Elst, L., Muller, R.N., 2009. Iron oxide based MR contrast agents: from chemistry to cell labeling. *Curr. Med. Chem.* 16, 4712-4727.
- [32] Park, S.M., Nyenhuis, J.A., Smith, C.D., Lim, E.J., Foster, K.S., Baker, K.B., Hrdlicka, G., Rezai, A.R., Ruggieri, P., Sharan, A., Shellock, F.G., Stypulkowski, P.H., Tkach, J., 2003. Gelled versus nongelled phantom material for measurement of MRI-induced temperature increases with bioimplants. *IEEE Trans. Magn.* 39, 3367-3371.
- [33] Tanimoto, A., Oshio, K., Suematsu, M., Pouliquen, D., Stark, D.D., 2001. Relaxation effects of clustered particles. *J Magn Reson Imaging* 14, 72-77.

**Chapter 4      Summary and Outlook**



---

**SUMMARY**

This thesis presents the development of novel formulations on the basis of magnetic iron oxide nanoparticles. Optimization of the synthesis route resulted in the development of particles meeting general requirements for eventual applications. Furthermore, the selection of appropriate stabilizing agents imparted the nanoparticles with beneficial features, making an *in vivo* application possible. In doing so, the formulations seem to be especially promising for the application as contrast agents in magnetic resonance imaging.

**Chapter 1** gives a brief insight into current research in the field of magnetic nanoparticles. While the originally promoted idea of dragging nanoparticles to the site of action by a massive external field is becoming less important, the use of magnetic carriers as single and multifunctional imaging agents is gaining in importance.

**Chapter 2** describes the synthesis of magnetic iron oxide nanoparticles with optimal properties for MRI contrast enhancement and the comparative assessment of polymeric macromolecules as stabilizers for such nanoparticles. It was revealed that particles covered by poly(ethylene imine)-*g*-poly(ethylene glycol) performed better than their poly(ethylene imine) counterparts, in terms of stability and cytotoxicity. The systems containing the former polymer showed pronounced colloidal stability even in protein-rich cell media. In addition, cytotoxicity was reduced by more than an order of magnitude. In this respect, the assumptions made in the run-up to the studies have found confirmation. Indeed, the introduction of hydrophilic poly(ethylene glycol) moieties to the polymer backbone positively manipulated the above properties. In addition, the physicochemical properties of the generated iron oxide nanoparticles were found to be excellent, despite the simplicity of the synthesis procedure. The iron oxide cores displayed high crystallinity, high saturation magnetization and superparamagnetic features. The polymer-coated nanoparticles were narrowly distributed around an average diameter of 40 nm and showed relaxation parameters comparable to



---

presently marketed products. Given these results, the established magnetic ferrofluids appear to be interesting for an intracorporal application as an MRI contrast agent.

The assumption that the configuration of magnetic nanoparticles affects cell uptake (mechanisms) and localization, and subsequently cellular MRI signaling, provided a basis for further studies. **Chapter 3** includes the evaluation of oppositely charged iron oxide nanoparticle systems with regard to physicochemical properties, cell interaction and cell-constrained relaxometry. The findings of this section confirm that surface potential is the key factor controlling cell internalization of magnetic iron oxide nanoparticles. Particles with a positive zeta potential were taken up to an almost tenfold extent after 24 hours, and with faster kinetics than the negatively charged counterparts. Basically, these results confirm the preliminary assumptions that electrostatic attractive forces between the cell membrane and the nanoparticles favor an enhanced internalization of positive carriers. However, the clear discrepancy in overall uptake led to the conclusion that synergistic effects, such as colloidal stability, also influence the rate of particle accumulation in cells. Both systems were found to be compartmentalized in endosomes after their uptake into cells by a correspondent endocytotic pathway. This cellular confinement caused the relaxation parameters to change in comparison to freely dispersed nanosuspensions, in such a way that the signal contrast in  $T_2$ -weighted MRI sequences degraded. Nevertheless, phantoms of cells incubated with positively charged nanoparticles still revealed effective signal darkening in these MRI sequences. The results suggest the suspensions examined as promising agents for cell tracking purposes, as here high iron uptake in combination with pronounced relaxivity is required.

---

## OUTLOOK

The development of a novel ferrofluid based on iron oxide and poly(ethylene imine)-*g*-poly(ethylene glycol) has been successfully accomplished. Moreover, the general potential of this formulation for biomedical applications has been demonstrated. The platform created facilitates the continuation of research in various directions. Among the many possibilities available, formulation testing *in vivo* seems to be the most reasonable option. In this context, biodistribution patterns after intravenous administration could be recorded, in order to identify accumulation in tissues other than the liver. However, in case the magnetic nanoparticles are rapidly transported in large part to the liver, they can still be tested for the detection of focal lesions. Most MRI contrast agents marketed are indicated for this kind of disorder, due to their missing tissue selectivity. Nevertheless, the future goal must be to achieve sufficient degrees of tumor selectivity. One approach, which has been discussed for several years, is the attachment of small molecules or other targeting moieties to the formulated nanoparticles. For the abovementioned particles, such a functionalization would be relatively easy, as the linker molecule in the form of poly(ethylene glycol) is intrinsically present. Depending on the selection of the targeting moiety, artificial tumors implanted into the flanks of mice could accumulate sufficient amounts of nanoparticles, and thus be imaged in a high-contrast manner. Concerning cell tracking purposes, it would be interesting to determine the maximum loading levels of different cell types with the ferrofluidic nanoparticles. Here, an upper limit is naturally set by cytotoxic side effects.

Besides the application in the domain of magnetic resonance imaging, ferrofluids can also be used for hyperthermia treatments. After loading cells with magnetic nanoparticles, it might be possible to selectively destroy the cells by an RF pulse.

---

## ZUSAMMENFASSUNG

In der vorliegenden Arbeit wird die erfolgreiche Entwicklung neuer Formulierungen auf der Basis magnetischer Eisenoxidnanopartikel vorgestellt. Durch Optimierung der Syntheseroute gelang es, Partikel zu entwickeln, die die generellen Anforderungen für eine anschließende Anwendung erfüllen. Die hergestellten Nanopartikel konnten zudem durch die Auswahl geeigneter Stabilisatoren derart ausgestattet werden, dass eine Applikation *in vivo* möglich ist. Dabei scheinen die Formulierungen besonders aussichtsreich für die Verwendung als Kontrastmittel im Bereich der Magnetresonanztomographie (MRT) zu sein.

**Kapitel 1** gibt einen kurzen Einblick in den derzeitigen Stand der Forschung auf dem Gebiet magnetischer Nanopartikel. Während die ursprünglich propagierte Idee, magnetische Nanopartikel durch starke Magnetfelder an einen Wirkort zu bringen, immer mehr an Bedeutung verliert, steigt ihr Stellenwert als uni- oder multifunktionales Kontrastmittel für die MRT stetig.

**Kapitel 2** beschreibt die Synthese magnetischer Eisenoxidnanopartikel mit optimalen Eigenschaften für die Kontrastgebung sowie die vergleichende Bewertung verschiedener polymerer Makromoleküle zur Stabilisierung dieser Partikel. Es konnte gezeigt werden, dass die Umhüllung der Kerne mit Polyethylenimin-*g*-Polyethylenglykol (im Gegensatz zu Polyethylenimin) zu Partikeln führte, die bessere Eigenschaften hinsichtlich Stabilität und Zytotoxizität aufwiesen. Dabei zeigten Systeme mit erstgenanntem Polymer sogar in proteinreichen Zellmedien ausgeprägte kolloidale Stabilität. Außerdem konnte für dieses System eine Verminderung der Zytotoxizität um mehr als den Faktor zehn festgestellt werden. Insofern wurden die Annahmen aus dem Vorfeld der Studie bestätigt. Die Anbringung von Polyethylenglykol-Resten ans Polymerrückgrat führte in der Tat zur Veränderung der genannten Eigenschaften – Stabilität und Zytotoxizität – in die vorausgesagte Richtung. Des Weiteren ergab sich, dass die physikochemischen Eigenschaften der Eisenoxidnanopartikel

---

trotz der Einfachheit der Synthesemethode herausragend waren: die Eisenoxidkerne zeigten hohe Kristallinität, hohe Sättigungsmagnetisierung und superparamagnetisches Verhalten. Die polymerbeschichteten Nanopartikel waren eng verteilt um einen mittleren Durchmesser von 40 nm und verfügten über Relaxationsparameter, die vergleichbar zu denen derzeit auf dem Markt verwendeter Produkte sind. In Anbetracht der Ergebnisse erscheinen die hergestellten ferrofluidischen Nanosuspensionen interessant für eine intrakorporale Anwendung als Kontrastmittel für die MRT.

In **Kapitel 3** werden entgegengesetzt geladene Nanopartikelsysteme im Hinblick auf ihre physikochemischen Eigenschaften, Zellaufnahme und Relaxometrie untersucht. Die Ergebnisse dieses Abschnitts bestätigen, dass die Oberflächenladung magnetischer Eisenoxidnanopartikel entscheidenden Einfluss auf deren Zellinternalisierung hat. Die Aufnahme nach 24 Stunden lag für Partikel mit positivem Zetapotential fast zehnmal so hoch wie für negative Partikel und erfolgte zudem mit schnellerer Kinetik. Grundsätzlich bestätigen die Ergebnisse unsere Annahme der schnelleren Aufnahme positiver Trägersysteme aufgrund der elektrostatischen Anziehung durch die Zellmembran. Der deutliche Unterschied in den absoluten Aufnahmeraten der beiden Systeme ließ allerdings vermuten, dass weitere synergistische Effekte, wie zum Beispiel die Kolloidstabilität, zur Zellinternalisierung beitragen. Beide untersuchten Systeme waren nach ihrer Aufnahme in zellulären Endosomen lokalisiert. Der Einschluss in endosomalen Kompartimenten führte zu einer Änderung der Relaxationseigenschaften im Gegensatz zu frei vorliegenden Nanosuspensionen. Zudem schwächte sich der Signalkontrast in  $T_2$ -gewichteten MRT-Sequenzen ab. Nichtsdestotrotz bewirkten Zellphantome nach Inkubation mit positiv geladenen Nanopartikeln ausgeprägten Kontrast in diesen Sequenzen. Die Ergebnisse deuten an, dass die untersuchten positiv geladenen Nanosuspensionen geeignete Kontrastmittel auf dem Gebiet der Zellverfolgung darstellen können, da dort umfassende Aufnahme und ausgeprägte Relaxivität gefordert sind.

---

**AUSBLICK**

Die Herstellung eines neuartigen Ferrofluids auf Basis von Eisenoxid und Polyethylenimin-g-Polyethylenglykol wurde erfolgreich durchgeführt, und sein generelles Potential für biomedizinische Anwendungen aufgezeigt. Die geschaffene Plattform ermöglicht eine Fortsetzung der Studien in verschiedene Richtungen. Unter den vielen Optionen stellt die *in vivo* Testung der Formulierung die sinnvollste Möglichkeit dar. In diesem Zusammenhang könnte die Bioverteilung nach intravenöser Applikation untersucht werden, um die Akkumulation in anderen Geweben als der Leber zu beleuchten. Im Fall, dass der Großteil der magnetischen Nanopartikel doch in der Leber angesammelt wird, kann eine Anwendung für die Detektion fokaler Läsionen in Betracht gezogen werden. Die meisten vermarkteten MRT-Kontrastmittel sind aufgrund ihrer fehlenden Selektivität für diese Indikation zugelassen. Das Ziel für die Zukunft muss es sein, ein ausreichendes Maß an Tumorselektivität zu erreichen. Eine seit Jahren diskutierte Methode ist das Anbringen kleiner Moleküle (small molecules) und anderer zielgerichteter Reste an Nanopartikel. Für die genannten Partikel wäre eine derartige Funktionalisierung relativ leicht, da die intrinsisch vorhandenen PEG-Moleküle als Linker verwendet werden können. Je nach Wahl der Funktionalität würden sich künstliche subkutane Tumoren in ihrer Aufnahmefähigkeit für unterschiedlich modifizierte Systeme unterscheiden und müssten folglich differenziert abbildbar sein. Bezüglich der Zellverfolgung wäre es interessant, den maximalen Beladungsgrad verschiedener Zelltypen mit ferrofluidischen Nanopartikeln zu ermitteln. Hierbei ist eine natürliche Grenze durch die zytotoxischen Nebenwirkungen gegeben.

Neben der Anwendung auf dem Gebiet der MRT können Ferrofluide auch für die Hyperthermiebehandlung eingesetzt werden. Nachdem Zellen mit magnetischen Nanopartikeln dotiert werden, wäre eine selektive Zerstörung dieser Zellen durch Radiofrequenzimpulse möglich.

## Appendices

---

---

**ABBREVIATIONS**

ANOVA	Analysis of Variance
CT	Computed tomography
DLS	Dynamic light scattering
DMEM	Dulbecco's modified eagle medium
EGFR	Epidermal growth factor receptor
EPR	Enhanced permeation and retention
FCS	Fetal calf serum
FDA	Food and drug administration
IC <sub>50</sub>	Inhibitory concentration 50 percent
ICP-OES	Inductively coupled plasma optical emission spectrometry
IONP	Iron oxide nanoparticles
IR	Infrared spectroscopy
LDA	Laser Doppler anemometry
MFI	Mean fluorescence intensity
MNP	Magnetic nanoparticles
MPS	Mononuclear phagocytic system
MR	Magnetic resonance
MRI	Magnetic resonance imaging
MWCO	Molecular weight cut-off
PBP	P-Selectin binding peptide
PBS	Phosphate buffered saline
PDI	Polydispersity index
PEG	Poly(ethylene glycol) / Poly(ethylene oxide)
PEI	Poly(ethylene imine)

---

PET	Positron emission tomography
PMA	Poly(maleic anhydride)
RF	Radiofrequency
ROI	Region of Interest
SAR	Specific absorption rate
SPECT	Single photon emission computed tomography
SPION	Superparamagnetic iron oxide nanoparticles
SQUID	Superconducting quantum interference device
TEM	Transmission electron microscopy
TGA	Thermal gravimetric analysis
USPIO	Ultrasmall superparamagnetic iron oxide
VSM	Vibrating sample magnetometer
XRD	X-ray diffraction



---

**LIST OF PUBLICATIONS****Research Articles**

C. Schweiger, C. Pietzonka, J. Heverhagen, T. Kissel

Novel magnetic iron oxide nanoparticles coated with poly(ethylene imine)-g-poly(ethylene glycol) for potential biomedical application: synthesis, stability, cytotoxicity and MR imaging.

Accepted in *International Journal of Pharmaceutics*, Dec 2010

**Conference Proceedings**

C. Schweiger, T. Kissel

Pulmonary application of nanoparticulate iron oxide formulations for MRI screening (Poster).

Materialwissenschaftlicher Tag, Gießen, Germany, Jul 2009

C. Schweiger, P. Rivera Gil, W. Parak, T. Kissel

MRI contrast enhancement potential of different superparamagnetic iron oxide nanoparticle (SPION) formulations (Poster).

European Symposium on Controlled Drug Delivery, Egmond aan Zee, Netherlands, Apr 2010

---

**CURRICULUM VITAE****Persönliche Daten**

Name	Christoph Gerhard Schweiger
Geburtsdatum	27. Juni 1979
Geburtsort	Schwabmünchen
Familienstand	ledig
Adresse	Fuggerstraße 1 86836 Klosterlechfeld

**Ausbildung**

09 / 1989 – 06 / 1998	Leonhard-Wagner-Gymnasium Schwabmünchen Zeugnis der Allgemeinen Hochschulreife
08 / 1998 – 09 / 1999	Zivildienst, Städtisches Krankenhaus Schwabmünchen
10 / 1999 – 09 / 2000	Studium der Elektro- und Informationstechnik, Technische Universität München
10 / 2000 – 06 / 2006	Studium der Pharmazie, Ludwig-Maximilians-Universität München
08 / 2006	Approbation als Apotheker
01 / 2007 – 12 / 2010	Wissenschaftlicher Mitarbeiter, Institut für Pharmazeutische Technologie und Biopharmazie, Philipps-Universität Marburg Anfertigung der vorliegenden Dissertation

**Berufspraxis**

05 / 2005 – 10 / 2005	Pharmazeutisches Praktikum Sani-Plus Apotheke München
11 / 2005 – 04 / 2006	Pharmazeutisches Praktikum Drug Delivery Systems Development Sanofi-Aventis Frankfurt

